Appel

PHOTOPRODUCTION OF CHARMED BARYONS

by

Mark C. Gibney

B.A., University of California, San Diego, 1980

A thesis submitted to the

Faculty of the Graduate School of the

University of Colorado in partial fulfillment

of the requirements for the degree of

Doctor of Philosophy

Department of Physics

1989

This thesis for the Doctor of Philosophy degree by

Mark Gibney

has been approved for the

Department of Physics

by

Uriel Nauenberg

Uriel Nauenberg

John Cumalat

John Cumalat

Date APRIL 25, 1989

Gibney, Mark C., (Ph.D., Physics)

Photoproduction of Charmed Baryons

Thesis directed by Professor Uriel Nauenberg

Measurements of the branching fractions of the four Λ_c^+ decay modes, $\Lambda^0\pi^+$, $\Lambda^0\pi^+\pi^+\pi^-$, $p\overline{K^0}$, and $p\overline{K^0}\pi^+\pi^-$ relative to the $\Lambda_c^+ \rightarrow pK^-\pi^+$ decay mode are presented. The experiment was performed at the Tagged Photon Spectrometer in the Proton East area of the Fermi National Accelerator Laboratory. The Tagged Photon Detector is a two magnet spectrometer with large angular acceptance, good mass resolution, and good particle identification. The particle identification is achieved using Cerenkov counters, muon detectors, and electromagnetic and hadronic calorimeters. Particle tracking and vertex detection are accomplished by using a system of drift chambers in conjunction with a set of high resolution silicon microstrip detectors. The construction, maintenance, and calibration of the Cerenkov counters was the main responsibility of the Colorado group.

The relative branching fractions for the four decay modes are determined to be;

$$\frac{B(\Lambda\pi)}{B(pK\pi)} = 0.17 \pm 0.08 \pm 0.05$$

$$\frac{B(\Lambda\pi\pi\pi)}{B(pK\pi)} = 0.82 \pm 0.29 \pm 0.27$$

$$\frac{B(p\overline{K^0})}{B(pK\pi)} = 0.55 \pm 0.17 \pm 0.14$$

$$\frac{B(p\overline{K^0}\pi\pi)}{B(pK\pi)} < 1.7@90\%CL.$$

These measurements are compared with existing theoretical results for the two-body decays ($\Lambda\pi$, $p\overline{K^0}$). Quark model and SU(4) calculations of these branching fractions agree with our measurements while a similiar calculation using the Bag Model disagrees. The results of this experiment provide the needed corroboration for branching fraction measurements made in e^+e^- collider experiments.

To Rhonda

For Her Love and Patience

ACKNOWLEDGMENTS

I begin by thanking the E691 collaboration:

University of Colorado, Boulder;

L. Cremaldi, J. Elliot, U. Nauenberg

University of California, Santa Barbara;

A. Bean, J. Duboscq, P. Karchin, S. McHugh, R. Morrison,

G. Punkar, J. Raab, M. Witherell

Carleton University;

P. Estabrooks, J. Pinfold, J. Sidhu

Centro Brasileiro de Pesquisas Fisicas;

J. Anjos, A. Santoro, M. Souza

Fermilab;

J. Appel, L. Chen, P. Mantsch, T. Nash, M. Purohit, K. Sliwa,

M. Sokoloff, W. Spalding, M. Streetman

National Research Council of Canada;

M. Losty

Universidade de São Paulo;

C. Escobar

University of Toronto;

S. Bracker, G. Hartner, B. Kumar, G. Luste, J. Martin,

S. Menary, P. Ong, G. Stairs, A. Stundžia

The dedication of these people was the first strength of the experiment.

The leadership provided during the run by Penny Estabrooks, Jeff Spalding, Steve Bracker, and Rolly Morrison was indispensible, inspiring, and unforgettable. The leadership provided by Mike Witherell during the data analysis was a lesson in leadership.

I personally thank my advisor, Uriel Nauenberg, for his patience, his guidance, his physics insight, and his patience. His encouragement throughout, and especially during the last few months, was not only appreciated but necessary.

I personally thank Lucien Cremaldi for his encouragement, his physics insight, and for reading this thesis (twice). The care and industry with which he worked was an example to me.

I thank Jim Elliot for helping me progress from a naive to a real understanding of how an experiment is done.

I thank Mike Sokoloff, Milind Purohit, Kris Sliwa, Ravi Kumar, and Alice Bean for many insightful conversations on many topics (including physics).

I thank my coworkers (Scott, Johannes, Tom, CW, Steve, Rich, Ray, Wes, Tim, Tosa, Greg, Harry, and Janice) for their support.

And I thank the Brazilians for their friendliness and kindness (which seemed to rub off).

Finally, I would like to thank those for whom thanks is not enough.

I thank my mother for her love and support.

I thank Rhonda, to whom this thesis is dedicated, for her love, her patience, and her encouragement.

And I thank my Lord, Jesus Christ, who has demonstrated through me that the hopeless have hope. Indeed, 'I can do everything through him who gives me strength'.

This work was supported by the U. S. Department of Energy.

CONTENTS

TABLES

FIGURES

Figure

CHAPTER 1

INTRODUCTION

High Energy Physics is the study of the very small. The smaller the object we wish to 'see', the smaller the wavelength (λ_γ) with which we need to illuminate the object. In particular, photons used to probe these objects must have high energies, since the photon wavelength is inversely proportional to its energy. At present energies, $\lambda_\gamma \sim 10^{-2}$ fermi, which is the domain of quarks and leptons.

1.1 The Fundamental Interactions

Quarks were introduced by Gell-Mann[1] in the mid-sixties as a mneumonic device to account for the many 'elementary' particles which had been discovered during the decades before. The experimentalists had turned up hundreds of these particles, each uniquely specified by its mass, decay rate, spin, etc. The quark model succeeded in explaining the abundance of these states as well as a good many of their characteristics, suggesting that the particles observed in nature were actually *composite* particles. In Gell-Mann's model, the experimentally observed particles were considered to be bound states composed of combinations of three elementary particles of spin 1/2; the up, down, and strange quarks. All physically observed states could be classified in this scheme as either a quark-antiquark combination ($q\overline{q}$: meson) or a three quark combination (qqq and $\overline{qqq}$: baryon and anti-baryon). The quark structure of the proton (uud) was directly confirmed a few years later in lepton-proton interaction experiments.[2] Table 1.1.1 shows that char-

Table 1.1.1 Characteristics of the Quarks and Leptons

Quark	Spin	Baryon Number	Lepton Number	Charge
d(down)	1/2	1/3	0	-1/3 e
u(up)	1/2	1/3	0	+2/3 e
s(strange)	1/2	1/3	0	-1/3 e
c(charm)	1/2	1/3	0	+2/3 e
b(bottom)	1/2	1/3	0	-1/3 e
t(top)*	1/2	1/3	0	+2/3 e

* the top quark is not established experimentally as yet

Lepton	Spin	Baryon Number	Lepton Number	Charge
ν_e	1/2	0	1	0 e
e(electron)	1/2	0	1	-1 e
ν_μ	1/2	0	1	0 e
μ(muon)	1/2	0	1	-1 e
ν_τ	1/2	0	1	0 e
τ(tau)	1/2	0	1	-1 e

acteristics of the quarks (deduced from the observed composite particles) as well as the characteristics of the leptons.

The existence of the Δ^{++} baryon, a symmetric state of three up quarks (uuu), indicated that the theory, as proposed, was incomplete. Three fermions cannot exist together in a symmetric state since they would then violate Pauli's exclusion principle. To solve this problem, a new quantum number called color was proposed.[3] This new degree of freedom could assume the three eigenvalues, red (r), green (g), and blue (b); however, only 'colorless' combinations of these eigenvalues could be used to represent physical states since the color quantum number is not observed in nature. The color wavefunction for the Δ^{++} is thus totally anti-symmetric, with the form;

$$\Psi_{\Delta^{++}} \propto (rgb - rbg + brg - grb + gbr - bgr) \tag{1.1.1}$$

where combinations of three unique colors are *defined* to be colorless. The inclusion of the color quantum number in the quark model, thus, satisfied the fermi statistics of the Δ^{++} state. The color wavefunction of the mesons likewise took the form;

$$\Psi_{meson} \propto (r\bar{r} + b\bar{b} + g\bar{g}) \tag{1.1.2}$$

to complete this picture.

Experimental support for color was provided when the rate;

$$R = \frac{\sigma(e^+e^- \rightarrow hadrons)}{\sigma(e^+e^- \rightarrow \mu\mu)} \sim 2 \tag{1.1.3}$$

was measured for center of mass energies below the charm threshold.[2] Without the color hypothesis, this rate would be three times smaller or $\sim 2/3$.

given $\sigma \propto (\text{charge})^2$, and the charge of the quarks (i.e. $R = ((2/3)^2 + (1/3)^2 + (1/3)^2)/1^2 = 2/3$ without color). Color took its rightful place in the full theory when it was recognized as the charge of the strong force.[4]

With this quark theory, all 'ordinary' mesons and baryons (those composed of u, d, and s quarks) could be accounted for. The charm quark was introduced into this scheme *prior* to the discovery of any charmed particles to account for the conspicuous absence of particle decays with $s \rightarrow d$ quark transitions. In the 3 quark (uds) model, decays of this type are expected to have significant branching fractions.[5] They are, however, strongly suppressed, as evidenced by the ratio;[2]

$$\frac{\tau(K_L^0 \rightarrow \mu\mu)}{\tau(K_L^0 \rightarrow all)} = (9.1 \pm 1.9) \times 10^{-9} \qquad (1.1.4)$$

where $K_L^0 \rightarrow \mu\mu$ can be considered as an $s \rightarrow d\mu\mu$ decay. Thus, the strangeness changing neutral current of the three quark model ($\propto \bar{d}\gamma^\alpha(1 - \gamma_5)s + \bar{s}\gamma^\alpha(1 - \gamma_5)d$ to first order) must be suppressed somehow. Glashow, Ilioupous, and Miani[6] demonstrated that the addition of the charm quark to the quark model forced the cancellation of the first order term of this current (and suppressed it to second order). The inclusion of this new quark thus led to a revised theory which conformed to the experimental facts much more closely.

If we include the leptons and the top* and bottom quarks in our set of elementary particles, we have the following set of particles;

⋆ Although the t=top quark hasn't been seen directly, the prevalence of b→ c transitions over b→s transitions[2] provides some evidence for its existence since the GIM mechanism with which the flavor changing neutral currents (b → s) are suppressed required that the quarks have a doublet structure.

$$\begin{pmatrix} u \\ d' \end{pmatrix} \begin{pmatrix} c \\ s' \end{pmatrix} \begin{pmatrix} t \\ b' \end{pmatrix}$$

$$\begin{pmatrix} \nu_e \\ e \end{pmatrix} \begin{pmatrix} \nu_\mu \\ \mu \end{pmatrix} \begin{pmatrix} \nu_\tau \\ \tau \end{pmatrix}. \qquad (1.1.5)$$

The doublet structure given these particles implies that flavor changing neutral transitions are suppressed,[7] as was first demonstrated by Glashow, Iliopoulos, and Miani.

The d′, s′, b′ introduced above are given by the expression;

$$\begin{pmatrix} d' \\ s' \\ b' \end{pmatrix} . = \bigvee \times \begin{pmatrix} d \\ s \\ b \end{pmatrix} \qquad (1.1.6)$$

where V is the Kobayashi-Maskawa matrix,[2] which relates the experimentally derived weak eigenstates (s′) to their strong counterparts (s). The fact that $s \neq s'$ implies that the weak decay products of the charm particle may not contain a strange quark. Expressed quantitatively, $c \rightarrow s' = s \times \cos\theta_c + d \times \sin\theta_c$ with $\theta_c = 13°$, and thus 5% ($\sim \tan^2\theta_c$) of the time the charm decay products will contain a down instead of a strange quark. In this estimate, we've used the simpler model of Cabbibo which excludes the top and bottom quarks. The Kobayashi-Maskawa model includes this third 'generation' of particles as a generalization of the Cabbibo model.

The interactions between these particles are categorized as electroweak, strong, and gravitational and are characterized by the strength of the interaction and its effective range. To begin with, the gravitational force is negligible for the small quark and lepton masses, even for these small distances. The remaining two forces are described using *gauge* theories;

theories that remain invariant under some specific local gauge transformation. Quantum electrodynamics (QED), of which the electro-weak theory is an extension, is the simplest example of a gauge theory and is invariant with respect to local changes in the phase of the QED wavefunctions. To illustrate the importance of this simple phase invariance, one can show that the classical electromagnetic field is a direct consequence of the local phase invariance of Schröedinger's equation.[7] In the realm of high energy physics, the electro-weak model provides the (very successful) description of the combined weak and electromagnetic forces, and quantum chromodynamics describes the strong force. These two gauge theories together are referred to as the Standard Model.

The bosons which mediate these interactions are, respectively, the photon (electromagnetic force), the W^+, the W^-, and the Z° (weak force) of the electro-weak theory, and the 8 gluons which mediate the strong force. The character of each of these forces can be related to the character of the boson that mediates it. The photon is massless and thus the electromagnetic force has 'infinite' range; its influence is felt directly over the classical distance scale. The slow decay rate and small effective range which experimentally separates the weak force from the other forces, is related to the large ($\sim$ $100\mathrm{GeV}/c^2$) masses of the $W^{+,-}(M_W)$, and the Z° (M_Z) bosons. The weak coupling is a full four orders of magnitude smaller than the electromagnetic coupling ($\alpha_W \sim \frac{\alpha_{EM}}{(M_W^2/M_P^2)}$). Finally the experimentally supported concepts of asymptotic freedom and quark confinement,[8] behaviour unique to the strong force, are related to the fact that the gluons interact with each other.

The character of the strong force makes charm physics particularly intriguing. Asymptotic freedom (quark confinement) implies that the effect

of the strong force decreases (increases) with decreasing (increasing) distance and thus perturbation theory applies most reliably to bound states of small size, << 1 fermi. The large charm quark mass naturally leads to smaller bound states[9] to which one might hope to apply perturbation theory with some confidence.

1.2 Predictions for Charmed Baryon Decays

The Λ_c^+ is the lowest mass charm baryon, with predicted quantum numbers $I(J)^P = 0(1/2)^+$ and quark content (cud). As it has the lowest mass of all the charmed baryons, it must decay weakly since flavor changing decays are weak. The simplest form for the three decay topologies available to this particle are the two W-emission diagrams shown in figure 1.2.1A (spectator decay) and 1.2.1C and the W-exchange diagram shown in figure 1.2.1B (the sea quarks have been omitted).

In the spectator decay shown in figure 1.2.1A, the charm quark emits a W^+ which converts to a $u\bar{d}$ quark pair ($= \pi^+$). The up and down quarks from the Λ_c^+ are spectators to the decay in the sense that they take no part in the weak interaction. The decay mechanism utilized by the diagram in figure 1.2.1C is also W-emission, as in the spectator decay. The final states generated with this diagram can be quite different than those attained through the simple spectator decay, however. Finally, W-exchange is shown in figure 1.2.1B. In this process, the charm and down quarks in the Λ_c^+ exchange a W^+, and a $q\bar{q}$ pair (at least one) is pulled from the sea. The specific two body decay modes available to each of these diagrams are discussed elsewhere.[10]

The theoretical discussion of these decays is slim and limited to the two body decays. All of the predictions are based on the charm flavor changing effective Hamiltonian, $\mathcal{H}_{cc}$, in the short distance approximation;[11,12]

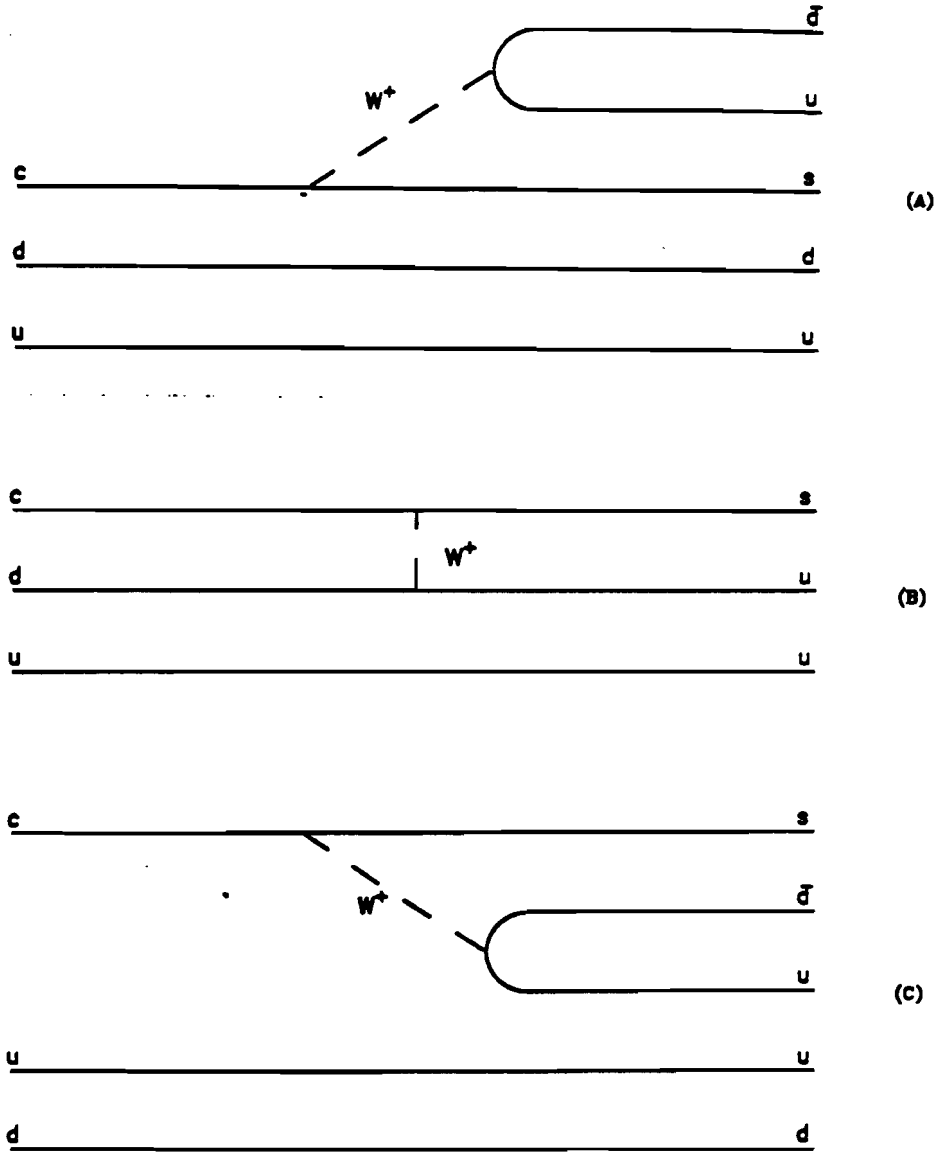

FIGURE 1.2.1. Decay Diagrams of the Λ_c^+ Baryon. (A) Spectator Decay. (B) W-Exchange Decay. (C) W-Emission.

$$\mathcal{H}_{cc} = \frac{G_F cos^2\theta_c}{\sqrt{2}}[f_- O^- + f_+ O^+] \tag{1.2.1}$$

with:

$$O^-_+ = \frac{1}{2} \times [(\overline{s}\gamma^\mu(1 - i\gamma_5)c)(\overline{u}\gamma^\mu(1 - i\gamma_5)d)^-_+$$

$$(\overline{s}\gamma^\mu(1 - i\gamma_5)d)(\overline{u}\gamma^\mu(1 - i\gamma_5)c)]. \tag{1.2.2}$$

Only the Cabbibo favored term is kept in this approximation. The f_+, f_- coefficients measure the hard gluon contributions to equation 1.2.1, where $f_+ = f_- = 1$ if strong interactions are ignored. Typically, $f_- = 1.96$ and $f_+ = .64$.[13]

Korner, Kramer, and Willrodt[11] have used the above effective Hamiltonian (equation 1.2.2) to make predictions of the two body decays of the Λ_c^+. In the first method used, they exploit the flavor symmetry of the O^-_+ operators (eqn. 1.2.3) of the effective Hamiltonian to obtain a large set of 'sum rules' relating $\Delta C = \Delta S = 1$ decays to established $\Delta C = 0$ decays. Estimates were then obtained for the decay rates of the $\Delta C = 1$ decays using the known behaviour of the non-charm decays. Clearly, the large symmetry breaking mass differences between the charmed and ordinary baryons limits the accuracy of this technique. They then use quark model wavefunctions (described elsewhere)[14] to calculate these decay rates. In this calculation, the quark wavefunctions are inserted into a decay amplitude similiar to that obtained using current algebra plus soft pion techniques.

The derivation of the amplitude using current algebra is described in the work of Ebert and Kallies.[13] In their paper, they derive the two body decay rates using this amplitude in conjunction with the MIT Heavy Bag Model wavefunctions. Finally, Hussain and Scadron,[15] using symmetry considerations along with extablished theoretical predictions for non-charm baryon decays, are able to derive the same rates, again with this current algebra derived decay amplitude. Further discussion of these models and their predictions will be left to chapter 8.

1.3 Charm Production and Detection

1.3.1 Production

Photon gluon fusion (PGF: figure 1.3.1) is assumed to be the primary mechanism of charm production in our experiment (e.g. we chose PGF as the charm production mechanism in our Monte Carlo).[16] This mechanism was chosen because it agreed well with the available experimental data. In photon-gluon fusion, the photon converts to a $c\bar{c}$ pair by fusing with a gluon from the target nucleus. Color is conserved by the emission of soft gluons (not shown).

It is interesting to compare the fraction of charm produced in these photon interactions with that expected in e^+e^- and hadron interactions. The charm fraction for these three production mechanisms is given roughly as $40\%_{ee}$: $1\%_{\gamma}$: $.1\%_{had}$.[17] In e^+e^- charm production, the virtual photon couples directly to the charge giving the production rate stated above (40% $= \frac{q_c^2}{\sum_{i=quark} q_i^2}$). The real photon again couples to the charm quark charge in charm photoproduction but the overall charm production rate is reduced to

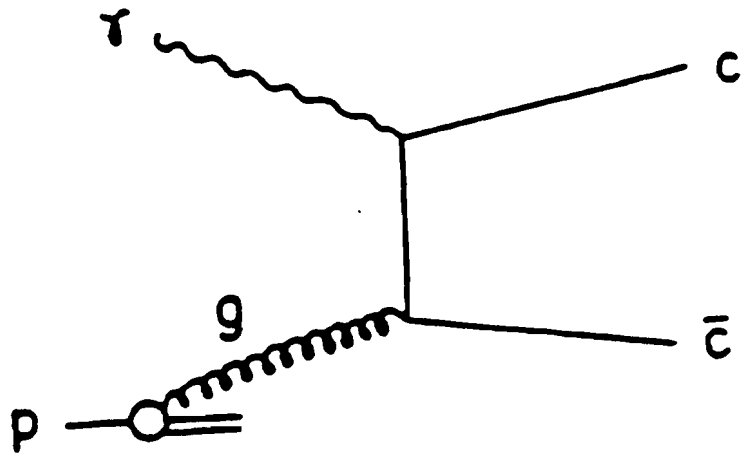

FIGURE 1.3.1. Photon Gluon Fusion

the 1% level by the high mass of the charm quark.* Hadroproduction suffers relative to photoproduction because, in gluon-gluon fusion (the hadronic production mechanism) the gluon coupling to the charm quark depends not on the quark charge but on the gluon momentum distribution which is skewed to low $X^{[2]}$ (X is the fraction of the particle's momentum carried by the gluon).

Naively, e^+e^- production of charm would be the favorite method of charm production, with hadroproduction the least favorite. The absolute production rate in real photon charm production is, however, orders of magnitude higher than e^+e^- production because of the higher effective luminosity in the photon experiment ($\mathcal{L}_{e^+e^-} \sim 1$ pb^{-1}/day[16] : $\mathcal{L}_{E691} \sim 10^3$ pb^{-1}/day). If one were able to control the increased backgrounds inherent in the real photon charm production, this increased rate of production could be put to advantage. Charm particle lifetime studies would be of particular interest since the boost the particle receives in the fixed target interaction is much greater than that received in the e^+e^- interaction ($P_{charm} \sim 3$ GeV/c^2 (e^+e^-) typically : 20 GeV/c^2 < P_{charm} < 140 GeV/c^2 (fixed target) in E691). Charm decay distances ($=\gamma c\tau$) would therefore be much greater in the fixed target interaction and hence measured more easily.

1.3.2 Detection

Detecting the charm signal produced in the experiment presents many problems. The first problem one notices is the low branching fractions of all charm decay modes. Typical values of 5% (compare this to the decay $\Lambda_0 \rightarrow p\pi$, with the branching fraction of $\sim$ 64%) imply that, for specific signals, we access not 1% of the total cross section, as discussed above,

* PGF productions crossections peak for low values of M^2 ($\equiv$ mass of the created particle pair).[16] Low mass quark photoproduction is therefore enhanced relative to charmed quark production.

but .05%. More worrisome still are the large number of possible track combinations in a typical fixed target event (the combinatorics). This problem is aggravated not only by the high track multiplicity (5-10) associated with these events but by the dominant non-charm event fraction as well. Given these considerations, the efficiency with which we reconstruct a given charm decay mode turns out to be on the order of 5%. Thus, for a charm decay with these characteristics (5% branching fraction; 5% efficiency $\Rightarrow$ strong candidate mode), only 2.5×10^{-4} of the recorded events would produce a reconstructed charm decay in this channel. We would therefore need to record 10^8 events to tape to reconstruct 2500 of these charm decays.

Recording 10^8 events does not solve the problem however. The goal of the experiment is not just to produce large signals but to produce large *significant* signals. The background, which is a product of the combinatorics discussed above, must then be separated from the signal by some means, and removed. From the advent of charm physics,[19] identifying and isolating the charm vertex from the production vertex was considered the most fertile signature available with which to identify charm signals. The decay distance in the beam direction of a typical charm particle would be on the order of millimeters for a fixed target experiment, given $c\tau_{charm} \sim 100\mu m$ (= proper decay length of the charm particle). For decay lengths of this size, one would need transverse resolution of $< 25\mu m$ from the vertex detector (section 3.2) to obtain significant separation of the charm and production vertices.

The fact that the charm quark decays predominantly to a strange quark is another well known signature for charm. This tendency (expressed quantitatively with the Cabbibo angle) implies that a strange particle is

normally among the charm particle's decay products. An effective particle identification scheme (section 3.5) that would allow one to separate the kaons and protons in these charm decays from the prevalent pions in the background events would lead to a large reduction in the combinatorics and provide a powerful background filter for the analyses of the charm decay modes.

The history of experimental fixed target charm physics teaches us one thing; charm signals have very large background levels. The e^+e^- experiments succeeded because they had manageable background levels to begin with. Fixed target experimenters had to learn how to manage their much larger background levels by exploiting the charm signatures discussed above.

1.4 A Brief History of Experiment E691

Each of the experimental refinements outlined in the previous section (a 10^8 event data sample, a high resolution vertex detector, superior particle identification) was realized by experiment E691. A critical study of the previous run, experiment E516, led to numerous important improvements in the spectrometer. The crucial improvement was the inclusion of the silicon microstrip detector (see section 3.2) which provided an additional background suppression of two orders of magnitude in the analysis of the charm decay modes. This enabled E691 to do fixed target charm physics effectively.

The experiment ran from late April 1985 until the end of August 1985 during which time $\sim 10^8$ events were written to tape. It should be noted that these events were taken with a transverse energy trigger that enhanced charm about 2.5 to 1 with respect to normal hadronic trigger events (see section 3.9). The analysis presented in this thesis includes the entire data set.

CHAPTER 2

THE PROTON AND PHOTON BEAMS

The study of the decay properties of charm particles was the goal of experiment E691, with an emphasis on lifetime and branching ratio determination. The hardware involved in the experiment was designed to maximize the production and optimize the detection of these charm particles. The decisions involving the hardware were constrained by competing considerations. Upstream of the photon-nucleon interaction, the beam flux, the electron and photon beam energy, and the beam purity were of most concern. Downstream of this interaction, accepting, identifying, and resolving the positions and momentum of the charm particle decay products, and rejecting non-charm background, were the primary concerns. The structural form and the function of each element of the beamline and the detector will be discussed as will the physical principles governing these devices.

2.1 The Proton Beam

The proton beam reached 800 GeV through a five stage process. First, hydrogen gas was ionized. The protons were then, in turn, accelerated to 750 KeV/c^2 by a Cockroft-Walton, to 200 MeV/c^2 by a linac, to 8 GeV by a booster ring, to 150 GeV by the Main Ring, and finally, to 800 GeV by the Tevatron which is a strong-focusing synchrotron using superconducting magnets. During the Main Ring acceleration stage, the protons were grouped into 'buckets', 2 ns in length and 19 ns apart, and the beam maintained this time structure at all subsequent stages. The protons were extracted from the

Tevatron during a 22 second spill and a new spill started every 65 seconds. Upon extraction, a septum split the beam between 3 beamlines; Meson, Neutrino, and Proton (fig(2.1.1). The Proton beam was shared between 3 more beamlines; PWEST, PCENTER, and PEAST, where PEAST contained the photon beamline used in this experiment. On average, PEAST received 20% of the 10^{13} protons generated in a typical Tevatron spill. Figure 2.1.1 shows the layout of the fixed target beamlines at Fermilab.

2.2 The Photon Beam

Conversion of this proton beam into a photon beam was handled in the following manner (fig 2.2.1).[20] The PEAST proton beam was directed onto a 30 cm berylium target (a) where secondary particles, charged and neutral, were created. The charged particles were swept into a beam dump by a magnet (b), while the neutral particles, mainly K_L^0s, neutrons, and photons from π^0s, continued on. The photons impacted a lead radiator (c) and converted to electron-positron pairs. At this point, we chose the electron beam which became the source, via bremstrahlung, of the final photon beam. An electron beam was chosen because, knowing the energy of this beam, and measuring the post-bremstrahlung electron energies (see section 2.3), we could derive the photon energy (i.e. tag the photon). The beam energy was selected using a set of adjustable magnets and horizontal collimators while the dispersion of the beam was determined by the size of the collimator openings. This beam was transported to the Tagged Photon Laboratory where it impacted a tungsten radiator (d) and produced a bremstrahlung photon (with $N_\gamma \sim 1/E_\gamma$[21]). The photon beam spot was then centered on the experimental target and was easily contained within the (2.5cm×2.5cm) transverse dimensions of the target.

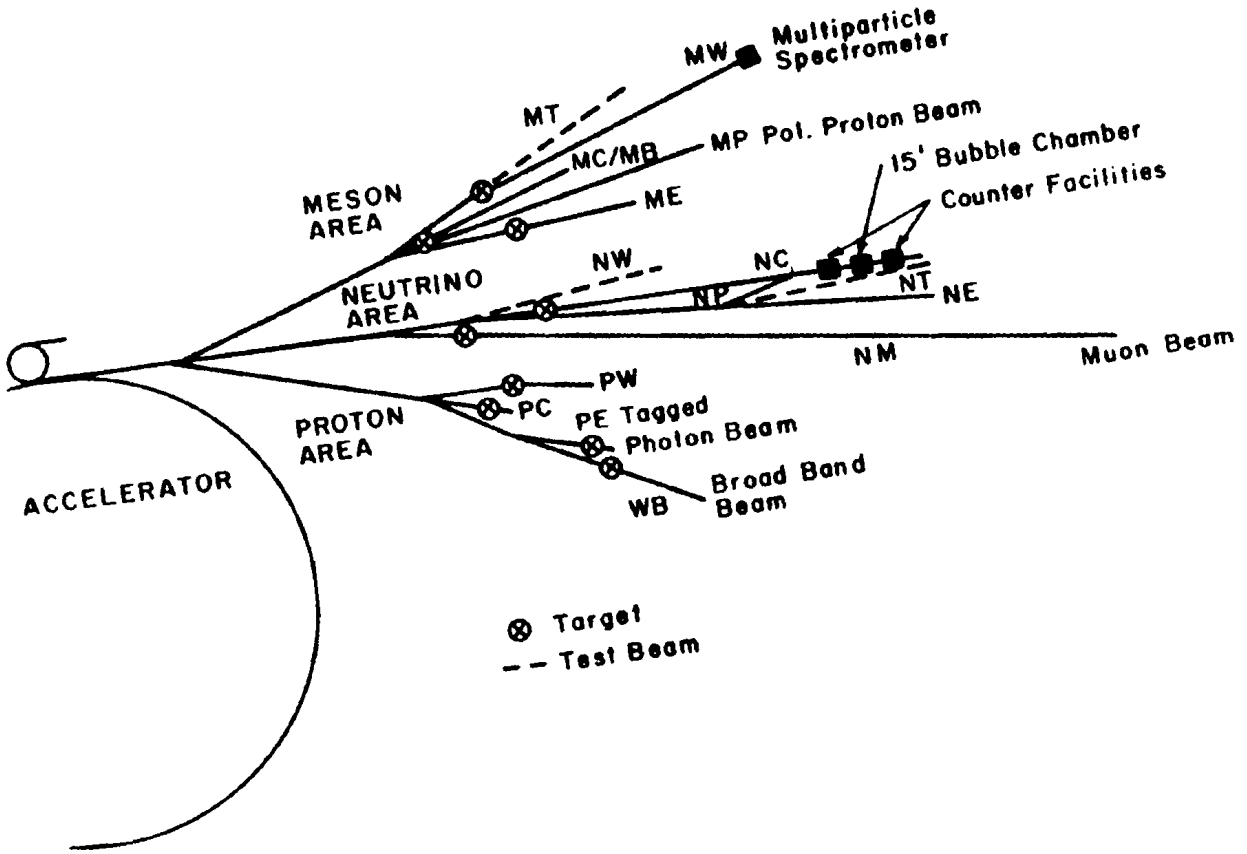

FIGURE 2.1.1. Fixed Target Beamlines

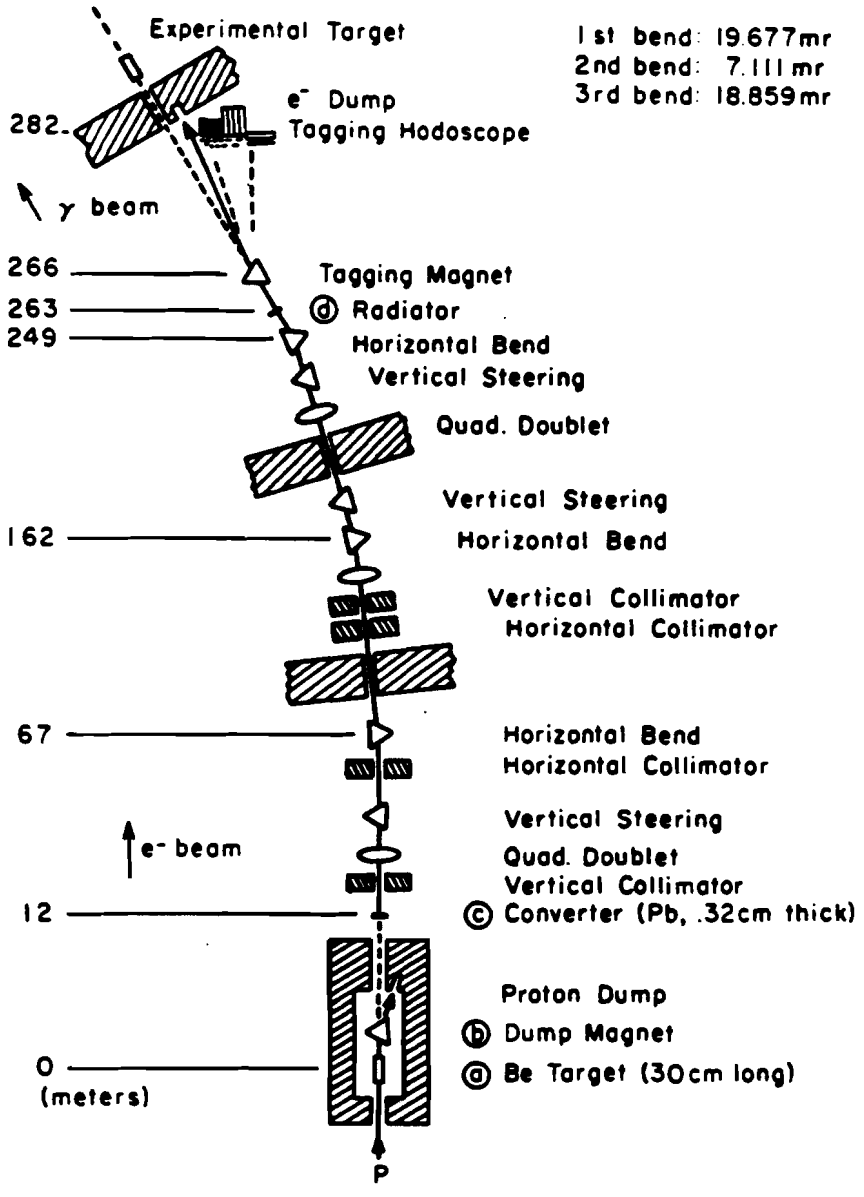

FIGURE 2.2.1. PEAST Beamline

To ensure the purity of the beam, the pion and muon contamination had to be minimized. The lead radiator was .5 radiation lengths and .02 interaction lengths thick so that the pion contamination introduced at this point by neutral hadronic interactions was small. The pions that were produced here had a much higher average P_t than the electron beam so, using tight vertical collimators in the beamline (fig 2.2.1), the pion contamination was reduced below the 1% level (the characteristic collinearity of the electron-photon system is exploited many times in the hardware design). The muon halo on the photon beam,which originated at the charged particle beam dump, was minimized by building the electron beamline 7 meters offline ($\sim$ 7 mr offset) from the original direction of the PEAST proton beam.

The choice of the beam energy, the beam flux and the tagging radiator then had to be made. A high electron beam energy was desirable because charm production cross sections rise significantly as the photon beam energy rises. The beam flux, on the other hand, decreases with the beam energy (fig 2.2.2) and thus had to be chosen in congress with the energy. All three choices affected our ability to tag the photon.

A radiator of .2 radiation lengths was chosen to suppress double bremstrahlung by the electron and pair production by the interaction photon, as both these effects made tagging the photon difficult. The choice of beam energy, 260$\pm$8.5 GeV, was motivated mainly by a desire to maximize the mean photon energy while maintaining sufficient flux. With this energy and radiator, the photon flux we obtained ($\sim 10^7\gamma$/spill > 80 GeV/c^2) produced enough interactions in the target to saturate the E691 data aquisition system (DA); $\sim$ 2200 events/spill with 30% deadtime (see section 4.2).

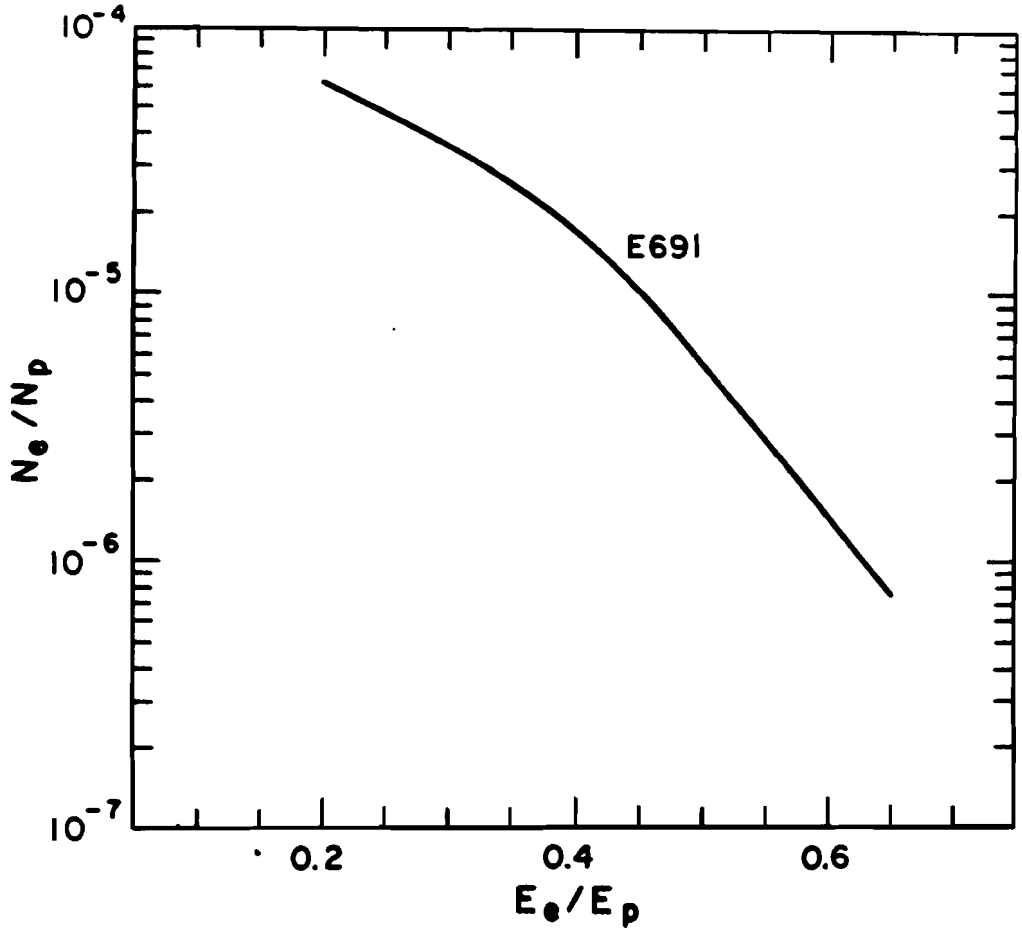

FIGURE 2.2.2. N_e/N_P = Fractional Electron Yield; E_e/E_P = Fractional Electron Energy. E691 operated at $E_e/E_P = 250/800$ with an electron yield of $\sim 2 \times 10^{-5}$.

With regards to tagging the photon beam, this beam flux implied that only 5% of the beam buckets entering the Tagged Photon Laboratory contained electrons and only 10% of these contained more than one. Multi-electron buckets were therefore not a serious problem for the tagging system since these buckets produced more than one photon only a few percent of the time. Double bremstrahlung in single electron buckets was also kept within reasonable limits, occurring $\sim$ 15% of the time. An attempt was made to address this problem (see section 2.3). In any event, with nearly the maximum electron beam energy (300 GeV = maximum energy transportable by the TPL beamline), we saturated our DA and kept double bremstrahlung and pair production in the radiator at acceptable levels.

2.3 The Tagging System

The tagging system provided the interaction photon energy for use in the study of charm photoproduction. After radiating the interaction photon, the electron was bent into the tagging system by 3 bending magnets. This system (fig 2.3.1) consisted of thirteen total absorption counters (L1-L13: 2 lead lucite, 11 lead glass blocks), thirteen hodoscopes (H1-H13) which intersect in the center of each absorption counter, 11 anti counters (A1-A11) to pick up electrons from pair production of the interaction photon in the radiator or from electron-electron scattering, and 2 dump counters (D1-D2) for very high (low) energy electrons (photons). The absorption counters were located relative to the beam line such that, given the strength of the tagging fields, the photon could be tagged in the energy range of $70 - 230$ GeV. They were coupled with RCA 6342A phototubes; the anode signal was fed into LRS 2249 ADC's and the dynode signal was latched and used to indicate whether this photon had been tagged (TAG). TAG originally required the

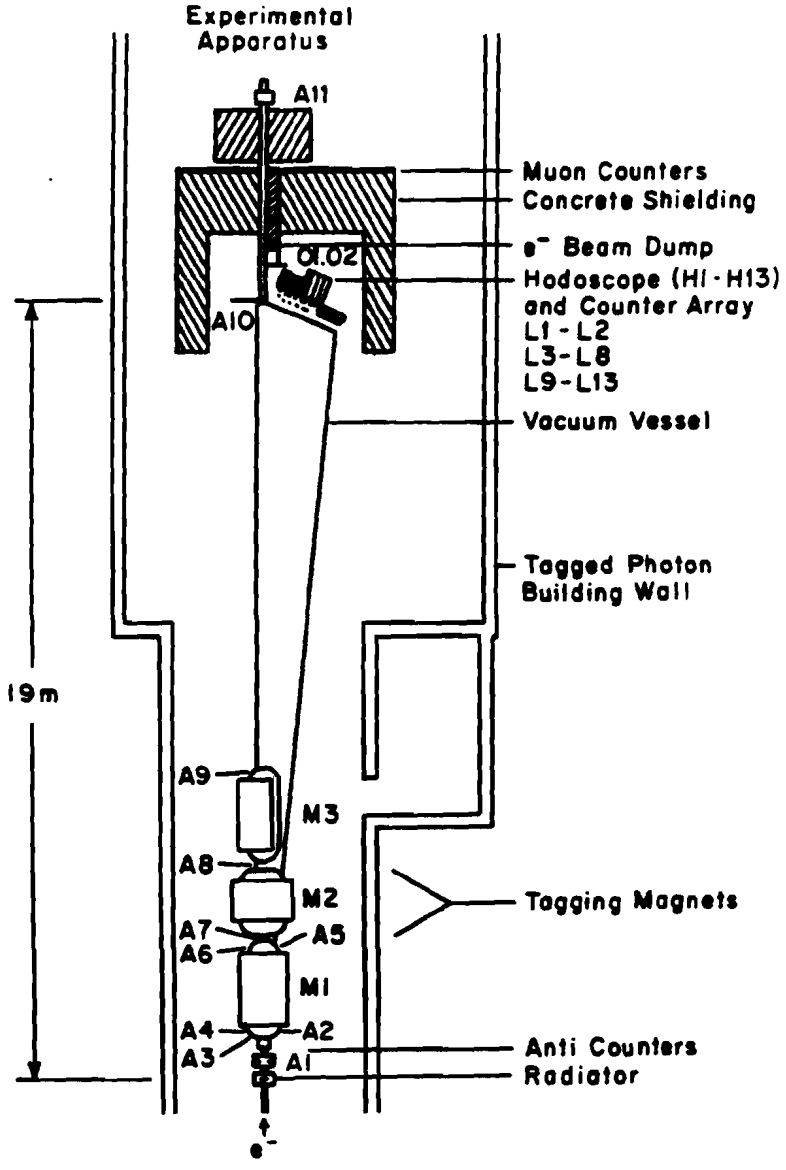

FIGURE 2.3.1. The Tagging System

logical AND of two adjacent hodoscope elements and the absorption counter directly behind it. However, the hodoscopes proved inefficient and were removed from the TAG logic for the last half of the experiment (see section 3.10).

The final element of the tagging hardware was the C-counter. This total absorption counter was placed after the last set of drift chamber planes, directly downstream of the target. It's purpose was to measure the energy of the non-interacting photons produced by multiple bremstrahlung in the radiator. The final photon energy would be given as

$$E_\gamma = E_{beam} - E_{TAG} - E_C$$

Due to the high flux of particles into this counter during the run, however, the more accurate measure of photon energy was simply,

$$E_\gamma = E_{beam} - E_{TAG}. \tag{2.3.1}$$

Calibrating the tagging system was a three step process. First, the C-counter was calibrated by turning off the tagging magnets and removing the target. Since the electron beam energy was known, the ADC counts per GeV in the C-counter was easily obtained (the linearity of the C-counter was tested with double electron buckets). Turning the tagging magnets back on but leaving the target out, we then calibrated the tagging system, with the photon energy measured by the C-counter,

$$E_{TAG} = E_{beam} - E_C; E_C = E_\gamma \tag{2.3.2}$$

Minimizing (for many events),

$$\chi^2 = \sum_{i=1}^{13} (E_{TAG} - g_i ADC_i)^2$$

we obtained the gains, g_i, of the phototubes.

Finally, the electron beam energy itself was calibrated using elastic ρ (and independently, Ψ) production ($\gamma p \rightarrow \rho X$; $\rho \rightarrow \pi^+\pi^-$). A check for energy deposition in the calorimeters and for high momentum tracks was made to ensure that this interaction was elastic. To good approximation,

$$E_{beam} = E_\gamma + E_{TAG}; E_\gamma = E_{\pi 1} + E_{\pi 2}$$

with the invariant mass of the two pions restricted to the ρ mass region. An in depth discussion of this procedure can be found elsewhere.[22]

CHAPTER 3

THE DETECTOR

The Tagged Photon Laboratory (TPL) spectrometer is a two magnet spectrometer with large acceptance, good mass resolution, good particle identification using Cerenkov counters, muon detectors, and electromagnetic and hadronic calorimeters, and very good secondary vertex detection using silicon microstrip detectors. The spectrometer is shown in figure 3.0.1. Each component of this detector is discussed below.

3.1 The Target

In choosing a target for the photon beam, we had to choose both the target material and the target size. The charm cross-section is $\widetilde{\propto}$ A and the dominant background for a photon beam is pair production which is $\propto Z^2$, so we had to minimize the ratio Z^2/A. The material with the smallest value of Z^2/A is deuterium, but, to obtain sufficient interaction rates with liquid D_2, the target would have had to be on the order of a meter in length. This poses some serious problems, because, for a one meter target, angular resolution and multiple scattering would dominate the resolution of the SMD's for most tracks associated with an interaction vertex (ideally, the intrinsic resolution of the SMDs provides the dominant contribution to the overall resolution). In addition to this, the charged track acceptance drops as the distance between the interaction vertex and the SMDs increases. Given these considerations, we chose a 5cm long berylium target. With this target, we achieved sufficient interaction rates, the multiple scattering and angular resolution contributions

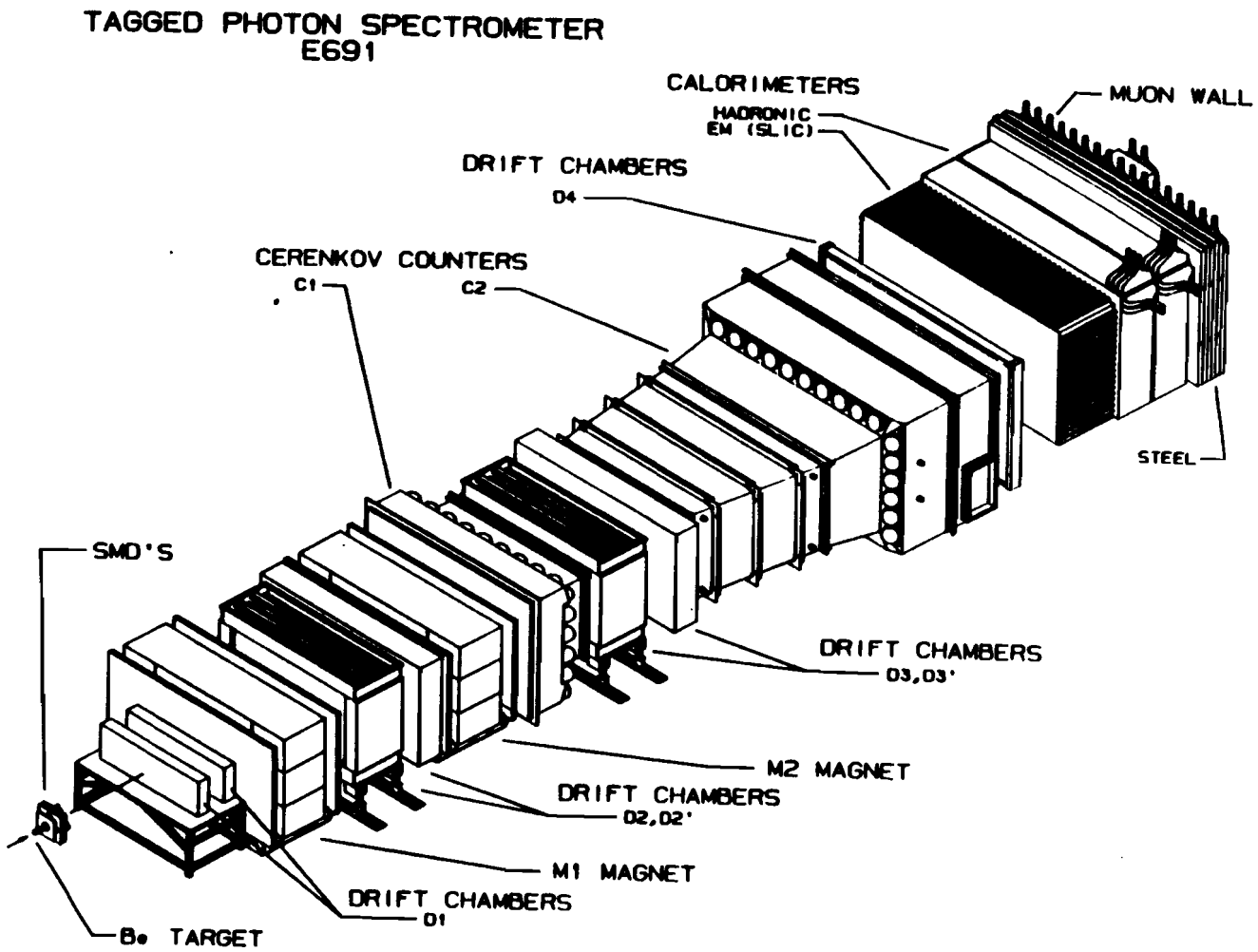

FIGURE 3.0.1. The Tagged Photon Spectrometer.

to the resolution were small, and the charged track acceptance was good. The tradeoff is that $(Z^2/A)_{Be} \simeq 4\times(Z^2/A)_{D_2}$ which was acceptable.

The frequency with which the photons interact a second time (secondary interactions) is also dependent on the choice of target length and material. These interactions are $\tilde{\propto} A^{2/3}$ so lowering this rate would have meant using a shorter target and, thus, lowering the primary interaction rate. The primary interaction rate could have only been made up with a higher photon beam flux which, as discussed earlier, meant a lower electron beam energy and a lower average photon spectrum energy. Thus, in order to maintain a constant primary rate of interaction, the average photon energy would have to drop as the target size decreased. The target chosen above was $\sim$ .1 interaction lengths which proved to be a satisfactory compromise choice implying a secondary interaction rate $\sim$ 5%.

The B-counter (not shown in the figure 3.0.1) was a small (2.5cm $\times$ 2.5cm active area) scintillation counter set directly downstream of the target. It was thin, to minimize secondary interactions and multiple scattering, and its phototube and base were designed to handle high rates. It was used to indicate that an interaction had occurred and it's threshold was set at just above 1 minimum ionizing particle (MIP). It's primary function was to set the timing of the experiment and to be used as an element in the trigger.

3.2 The Silicon Microstrip Detector

The purpose of the silicon microstrip detectors (SMD) was to detect the small separation (a few mm) between the interaction and the charm decay vertices. As mentioned earlier, charm particles decay weakly so transverse decay distances on the order of $100\mu m$ are expected, with $c\tau \sim 100\mu m$. Our system of 9 SMD planes (see table 3.2.1) had a pitch of $50\mu m$ and,

thus, an intrinsic transverse resolution of $14\mu m$ per plane[23] (experimentally measured resolution $16\mu m$[24]) which was sufficient to isolate the secondary vertex. Requiring a significant separation between the charm decay and interaction vertices in the data analysis would typically drop background levels by two orders of magnitude.

Table 3.2.1: Characteristics of the Silicon Microstrip Detectors

Triplet	**1**	**2**	**3**
size	2.6cm×2.6cm	5.0×5.0	5.0×5.0
pitch	$50\mu m$	$50\mu m$	$50\mu m$
strip width	$300\mu m$	$300\mu m$	$300\mu m$
working strips/plane	512	768	1000
z(central)	6.684cm	14.956cm	23.876cm

Figure 3.2.1 shows a cross-section of a silicon microstrip plane. The structure is that of a P-I-N diode[25] , with boron implanted in strips on the upper surface, arsenic implanted on the lower surface, and aluminum deposited on top of these layers to provide the electrical connection. Applying an electric field to this plane creates charged layers on either side of the P-I junction because the conduction electrons in the undoped silicon drift into the P+ (boron) region until the field created by the charge imbalance prevents further migration. The positively charged layer is called the depletion zone because this migration depletes the conduction band in the silicon. The entire undoped silicon wafer can be depleted by applying a 'reverse bias' voltage of about 90V across the microstrip plane. During the operation of the detector, this wafer must be fully depleted to prevent the holes from recombining with conduction band electrons as this would reduce the signal. Once

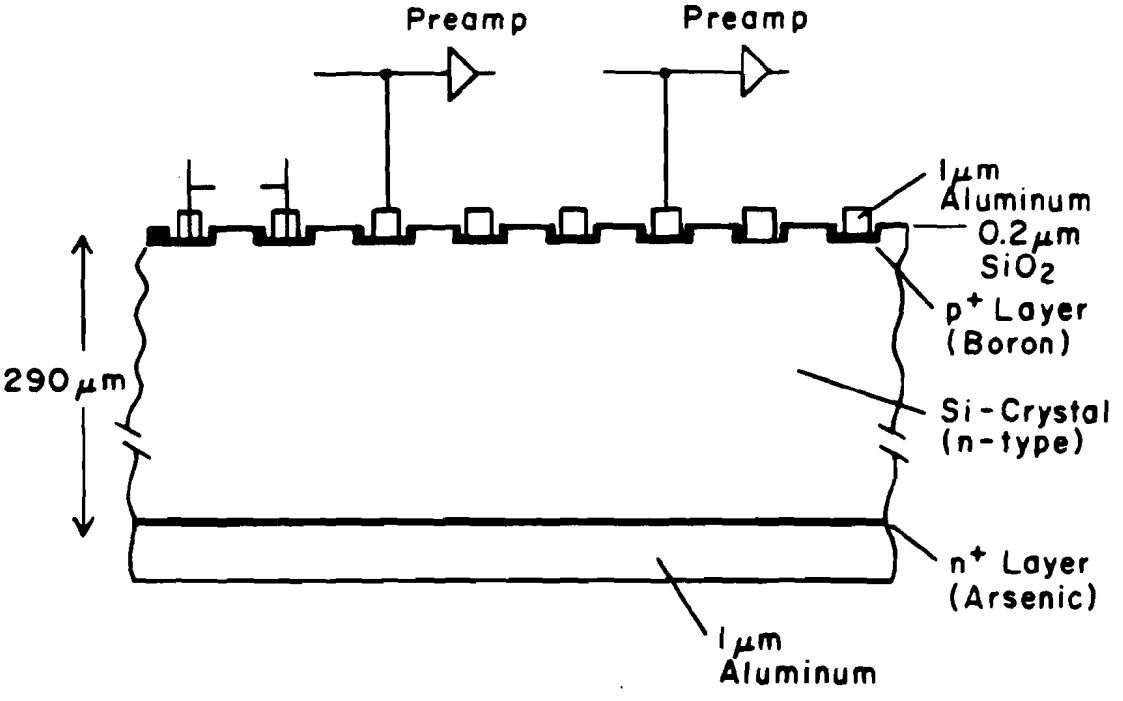

FIGURE 3.2.1. Cross-section of a Silicon Microstrip Plane.

fully depleted, any electron-hole pair created in the silicon is efficiently swept out by the field across the plane; the holes to the P+ layer, the electrons to the N+ layer (which is held at ground). The passage of a MIP through the depleted microstrip plane created $\sim$ 24000 electron-hole pairs and the signal picked up by the strips (the hole cloud) was collected in less than 10ns with a typical transverse extension of $10\mu m$.

The size of the detectors and of the output signals they generated presented major experimental difficulties. With 6840 instrumented channels, the volume increase in hardware from the microstrips to their CAMAC readout was greater than 3 orders of magnitude. To complicate things further, the signals from the SMD's were $\sim$ 4 femtocoulombs so everything had to be shielded and efficiently grounded. To be specific, the preamplifier assigned to each instrumented strip had to be positioned close to that strip to minimize the capacitance and, thus, the noise introduced at this stage. In addition to this, the rotational position of each detector plane, as well as its position with respect to the beam axis, had to be extremely well defined to take full advantage of the spatial resolution of this detector. Finally, the leakage currents across these planes, caused by noise induced electron-hole pair generation in the silicon,[25] had to be closely monitored. Fortunately, these currents remained under control during the run due to proper preparatory care of the detectors.

The 9 SMD planes were ordered into 3 triplets of 3 views each; X, Y, and V (+20.5° to X). Each triplet was located in a light tight, rf shielded box and positioned with a plane to plane precision of $12\mu m$ and relative rotational offset precision of .8mr. The preamps were attached directly to the rf boxes and generated outputs of $\sim$ 1mV. This signal was transmitted to the readout

system by 4m shielded cables of 9 channels each; 4 channels carrying signal and the 5 alternate channels connected to ground to reduce cross-talk. The signals were fed into 8 channel Nanosystem S710/810 MWPC shift register cards which were discriminated at $\sim$ .4mV and read out serially by CAMAC. With this discriminator level and a 50ns gate for the event, we averaged 1 noise hit per plane per event while the track detection efficiency at large angles dropped by only 20% (transverse extent of signal here $> 25\mu m$). In general, the per plane track detection efficiency was $\sim$ 90%. Further details on the construction and operation of this detector can be found elsewhere.[24]

3.3 The Drift Chamber System

The drift chamber system provided additional track position information and in conjunction with the magnets, determined the track momenta. There were 35 drift chamber planes grouped into 11 assemblies, each assembly generating a space point (triplet) for each track. These assemblies were, in turn, grouped into 4 drift chamber stations with which we could obtain a measurement of the track direction and position at particular locations along the spectrometer and thus determine its momentum (see table 3.3.1).

In a typical drift chamber plane, the grounded sense wires alternate with field shaping wires which are held at high negative voltage ($\sim$ -2 kV). This plane is sandwiched between two planes of wires all of which are set to high negative voltage ($\sim$ -2.4 kV). The electric field one obtains in the region bordered by the field shaping wires and the high voltage planes is approximately constant in magnitude and direction, except near the sense wire; this region is called a cell. For certain gas environments (ours: 50-50 argon/ethane + 1.5% ethanol to quench sparks) and high voltage settings, the electrons freed in this cell by the passage of a charged particle will drift

to the sense wire with an approximately constant drift velocity which is reasonably insensitive to small voltage changes. Thus, given the measured drift time Δt and the drift velocity v_{drift}, a reliable measure of the distance from the impact point of the ionizing particle to the sense wire can be made, $d_{drift} = v_{drift} \times \Delta t$, and position resolutions of $\sim 300\mu m$ can be achieved.

Table 3.3.1: Characteristics of the Drift Chambers

Station	**D1**	**D2**	**D3**	**D4**
dimensions	160cm×120cm	230×200	330×200	550×300
No. of assemblies	2	4	4	1
No. of planes	8	12	12	3
cell size: X/UV	.446/.476	.953/.893	1.588/1.487	3.18/2.98
resolution	$350\mu m$	300	300	800
z(upstream end)	154cm	382	928	1738

There are some serious complications inherent in this cell construction scheme. To begin with, we don't know on which side of the wire any given hit was made; all hits are 'left-right ambiguous'. Most of these ambiguities were removed by taking 3 position measurements, at X, U, and V where U and V are $\pm$ 20.5° from X, respectively. (In the drift chamber assembly upstream of the first magnet, an additional plane X′ offset in x from the X plane was added because of the high track density in these chambers). In addition, the high noise rate of the chambers, along with the left-right ambiguities, generated 10-100 times more false than true triplets in the drift chambers. This problem was handled by stacking redundant assemblies next to each other to filter out the false triplets (see table 3.3.1). As a final complication, the approximation of a constant drift velocity falls apart as the

signal electrons approach the high fields at the sense wire. This limited our ability to resolve the impact point with the simple linear equation for d_{drift} given above (on a positive note, the avalanche caused by the signal electrons in this region would typically amplify this signal into the convenient 1mV range). These and other problems are discussed in detail elsewhere[26] .

To obtain d_{drift} from the hardware, we need v_{drift} and Δt, as stated above. The time actually measured by the Time to Digital Converter (TDC) connected to this sense wire is $\Delta t' = T_{stop} - T_{start}$. T_{start} is the time at which the signal from the sense wire reaches the TDC and T_{stop} is generated by the trigger logic such that any sensible T_{start} is before T_{stop}. For our case then,

$$\Delta t = (T_{stop} - T_{start}(0)) - \Delta t'$$

with $T_{start}(0)$ equal to the time measured by the hardware when a track *hits* the sense wire (it is determined by cable lengths, electronic response, and the z-position of the cell in question).

In the drift chamber vernacular we get;

$$(T_{stop} - T_{start}(0)) = T_{rel} + T_{abs}.$$

T_{abs} is the time assigned to each plane to account for the intrinsic time differences between the planes while T_{rel} accounts for the cell to cell time differences by measuring the response of the cells in this plane relative to T_{abs}. Knowing the constant time offsets between the planes and between the cells in each plane, we can obtain the physically pertinent quantity, the drift time. Finally,

$$\Delta t = T_{rel} + T_{abs} - \Delta t' \tag{3.3.1}$$

The LRS 4290 system is able to account for T_{rel} on-line by pulsing the planes during the run[26] . Therefore, the value we write to tape is,

$$(\Delta t' - T_{rel}) = T_{abs} - \Delta t \tag{3.3.2}$$

This distribution is shown in figure 3.3.2 where t_2=T_{abs}, t=0=T_{stop}, and t_1=time measured from the edge of the cell.

The muon halo, discussed earlier, provided a clean source of tracks with which to calibrate not only the T_{abs}, but v_{drift}, and the chamber alignment offsets as well[26] . With Δt and v_{drift} in hand, we obtained d_{drift} and could then proceed to determine the positions and momenta of the tracks throughout the spectrometer. The drift chamber planar efficiencies were $\sim$ 90%.

As stated earlier, the eleven assemblies are split up into 4 drift chamber stations so that we could obtain a reliable measure of the direction and positions of the tracks. D1, assisting the SMDs, pinned down the tracks upstream of the first magnet, M1. D2's four assemblies provide the tracking between M1 and the second magnet, M2. D3 provides the final particle trajectories and positions with an assist from D4 (which had limited usefulness because charged particles back scattered from interactions in the SLIC (sec 3.6) reduced this chamber's position resolving capabilities[22]). We obtain the momentum using the relation,

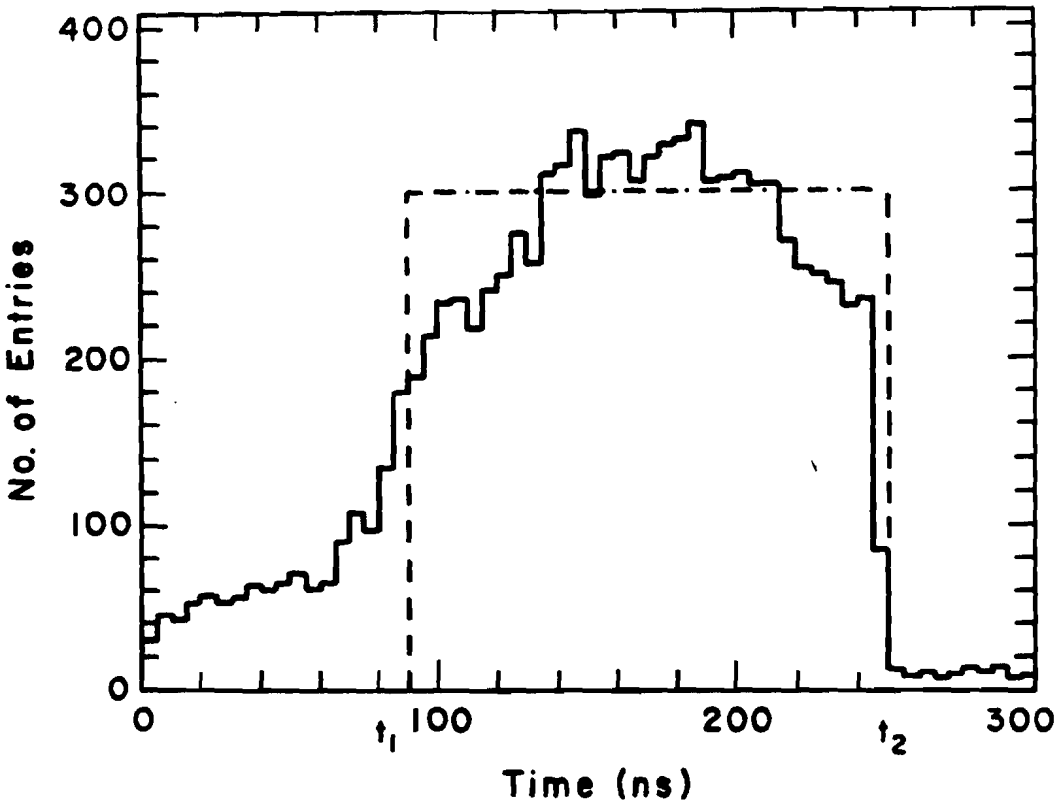

FIGURE 3.3.2. T0 Distribution. The dashed curve represents the response of a perfect cell with $t_2 = T0_{ABS}$ and t_1 = outer edge of cell. The histogram represents the response of a physical cell where non-linear drift velocities, etc. have affected the shape of the distribution.

$$p = \frac{.3 \int B \cdot dl}{\Delta\theta}, \tag{3.3.3}$$

where $\Delta\theta$ is the measured change in trajectory from one side of a magnet to the other. The momentum resolution is given by

$$|\sigma_p/p| \simeq \frac{p}{.3 \int B \cdot dl} \sigma_{ang}, \tag{3.3.4}$$

where

$$\sigma_{ang} \tilde{\propto} \frac{\sigma_x}{L\sqrt{N}}, \tag{3.3.5}$$

with σ_x the error in the drift chamber position measurement, N the number of planes, and L their separation. We see that momentum resolution improves with increasing field and increased redundancy. For E691, the momentum resolution for tracks that penetrate both magnets was $\Delta p/p \simeq .05p(\mathrm{GeV/c^2})\% + .5\%$[26] where the last term is due to multiple scattering.

3.4 The Magnets

The characteristics of the E691 magnets are given in table 3.4.1. They were used not only to derive track momenta but to sweep low energy e^+e^- pairs out of the spectrometer and to increase charged track separation (implying better tracking in the drift chambers downstream of them). The fields were measured using a zip-track which employed a small cart with 3 small perpendicular wire coils. It ran on an aluminum track which penetrated both magnet apertures allowing the coils to test the field at well defined values of (x, y, z). These values were written to tape and then fit with orthogonal polynomials consistent with Maxwell's equations. The field

strengths used by E691 are in the table. The quality of the map was measured by studying the $K_s \rightarrow \pi\pi$ mass and comparing its average value to the Particle Data Group[2] value.

Table 3.4.1: Characteristics of the TPL Magnets

Magnet	M1	M2
entrance	154cm×73cm	154cm×69cm
exit	183cm×91cm	183cm×86cm
length	165cm	208cm
$\int$B·dl	−.071 T-m	−1.07 T-m
P_t kick	0.21GeV/c^2	0.32GeV/c^2

3.5 The Cerenkov Counters

The Cerenkov counters were the primary responsibility of the Colorado group. It was my responsibility to maintain them during the experimental run and therefore this detector will be discussed in more detail than the other detectors in the spectrometer. They were used to identify the protons and charged kaons from among the more prevalent pions in the data, for the presence of these less copiously produced particles is a signature of charm particle decays.[19]

A particle exceeding the speed of light in a given medium emits Cerenkov radiation,[27] implying that the momentum at which the radiation is first produced is,

$$p_{th} \cong \frac{mc}{\sqrt{2\epsilon}} \tag{3.5.1}$$

with ϵ=n(λ)-1 and n(λ)=index of refraction of medium. This is called the

threshold momentum. Further, the amount of radiation emitted per unit λ, per unit length is,[27]

$$\frac{dN_\gamma}{d\lambda dl} = \frac{2\pi\alpha}{\lambda^2(1 - cos^2\theta_c)} \tag{3.5.2}$$

where $cos\theta_c = 1/\beta^2 n^2(\lambda)$ is the cosine of the angle of emission of the radiation with respect to the direction of the emitting particle. Given the momentum of a track, we set limits on its mass using the threshold behavior of the Cerenkov counters (eqn 3.5.1). The mass hypotheses still allowed within these limits were then each assigned a probability based on a comparison of the actual response of the counters to the response expected for each proposed mass.

3.5.1 Counter Design

The upstream end of the most upstream Cerenkov counter (C1) is five meters from the target, thus we must differentiate between the five particle types that reach this detector; electrons, muons, pions, kaons, and protons. The momentum distribution of charm decay tracks, for Monte Carlo and for data, is given in figure 3.5.1. The bulk of the tracks have momentum in the range 5-35GeV/c^2 so the index of refraction of the gas in the Cerenkov counters was chosen to optimize proton/kaon/pion identification for these momenta. C1 was filled with pure nitrogen (n=1.000309 $\Rightarrow$ π threshold 6.0 GeV/c^2) and C2 was filled with 80% helium and 20% nitrogen (n=1.0000901 $\Rightarrow$ π threshold 10.5 GeV/c^2). Leptons from pion or kaon decay, i.e. most leptons, are also well separated from pions by this choice of refractive indices since their momenta are peaked well below 10GeV/c^2 . Leptons with high momentum from charm decay rely on information from

the SLIC (sec 3.6) and the muon wall (sec 3.8) to augment the Cerenkov information. The threshold behavior of the two Cerenkov counters for the three prevalent particle types is illustrated in figure 3.5.2.

The Cerenkov counters are shown in figure 3.5.3 and their parameters described in table 3.5.1. The design specifications of the two counters are straight forward. The length of both counters was chosen so that, allowing for the index of refraction of the gas, absorption in the gas, reflectivities, and the quantum efficiency[28] of the phototube, approximately fifteen photoelectrons would be obtained in each. The Cerenkov light is emitted, as stated earlier, at an angle $\cos(\theta_c) = (1/\beta^2 n^2(\lambda))$ with respect to the particle direction, and isotropically in the angle ϕ. The radiation pattern for a constant velocity particle is, therefore, disk-like with radius = L $\times$ $\tan\theta_c$ (where L = length of the Cerenkov counter). This radiation pattern hits a wall of spherical mirrors at the counter's downstream end. The mirror walls in C1 and C2 (with 28 and 32 mirrors respectively) are shown in figure 3.5.4.

Table 3.5.1: Characteristics of the Cerenkov Counters

Counter	C1	C2
length	3.7 m	6.6 m
No. of cells	28	32
gas	N_2	80% He + 20% N_2
refractive index	1.000309	1.0000901
radius of light pattern(max)	8.4cm	8.7cm
π threshold	6.0GeV/c^2	10.5GeV/c^2
z(mirror plane)	866cm	1653

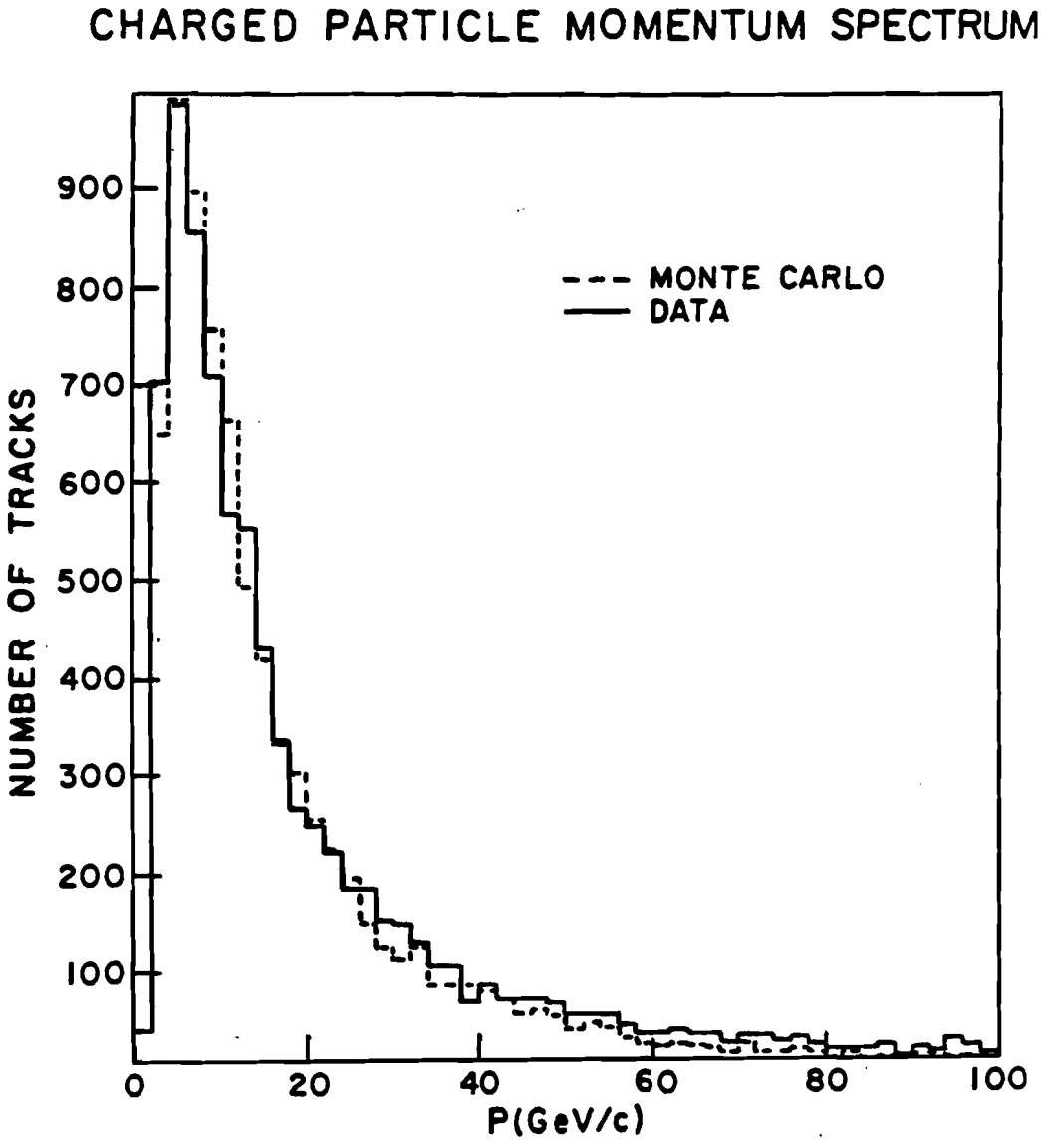

FIGURE 3.5.1. Predicted and Observed Momentum Spectrum of 2-Magnet Tracks.

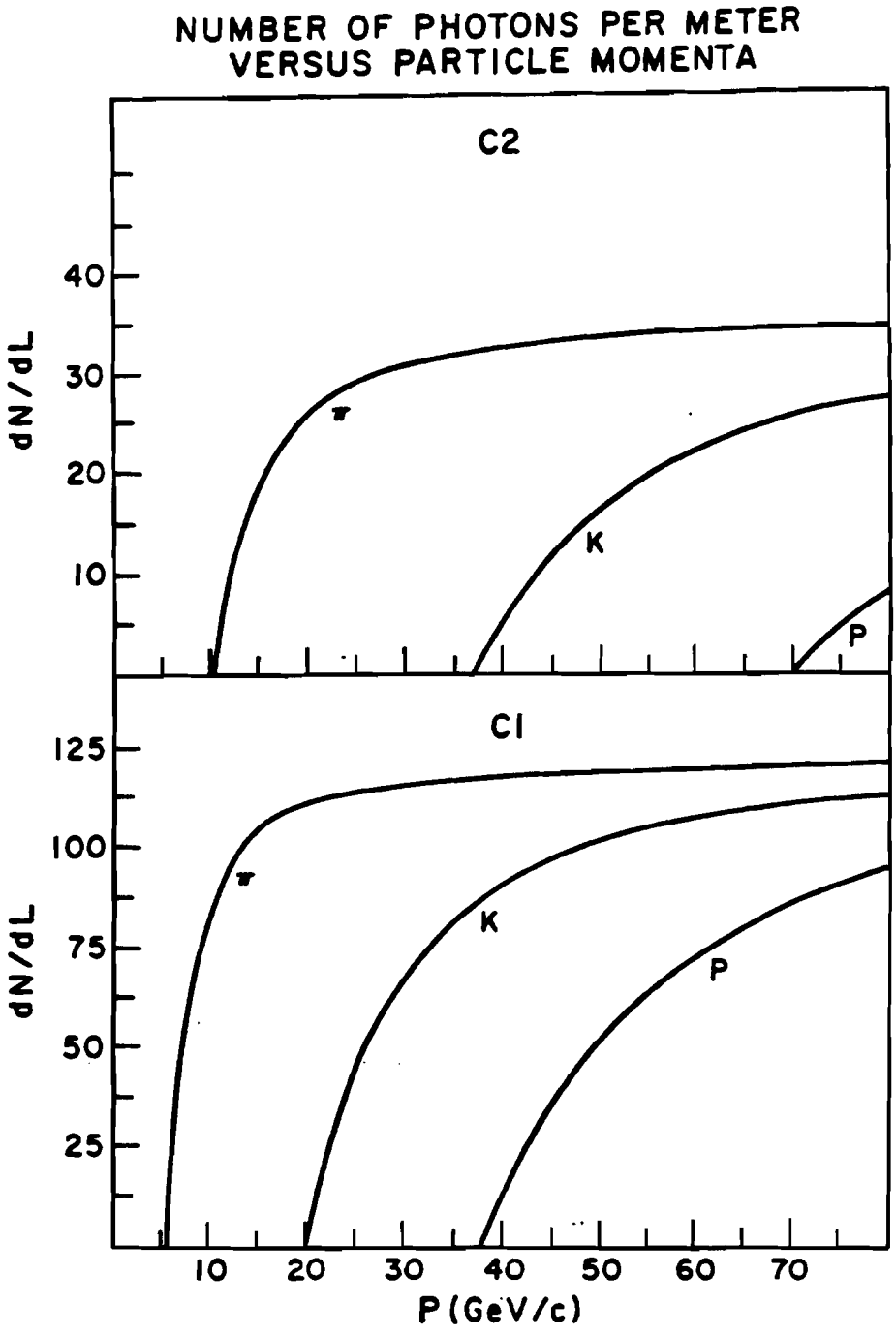

FIGURE 3.5.2. Threshold Behaviour of the Cerenkov Counters.

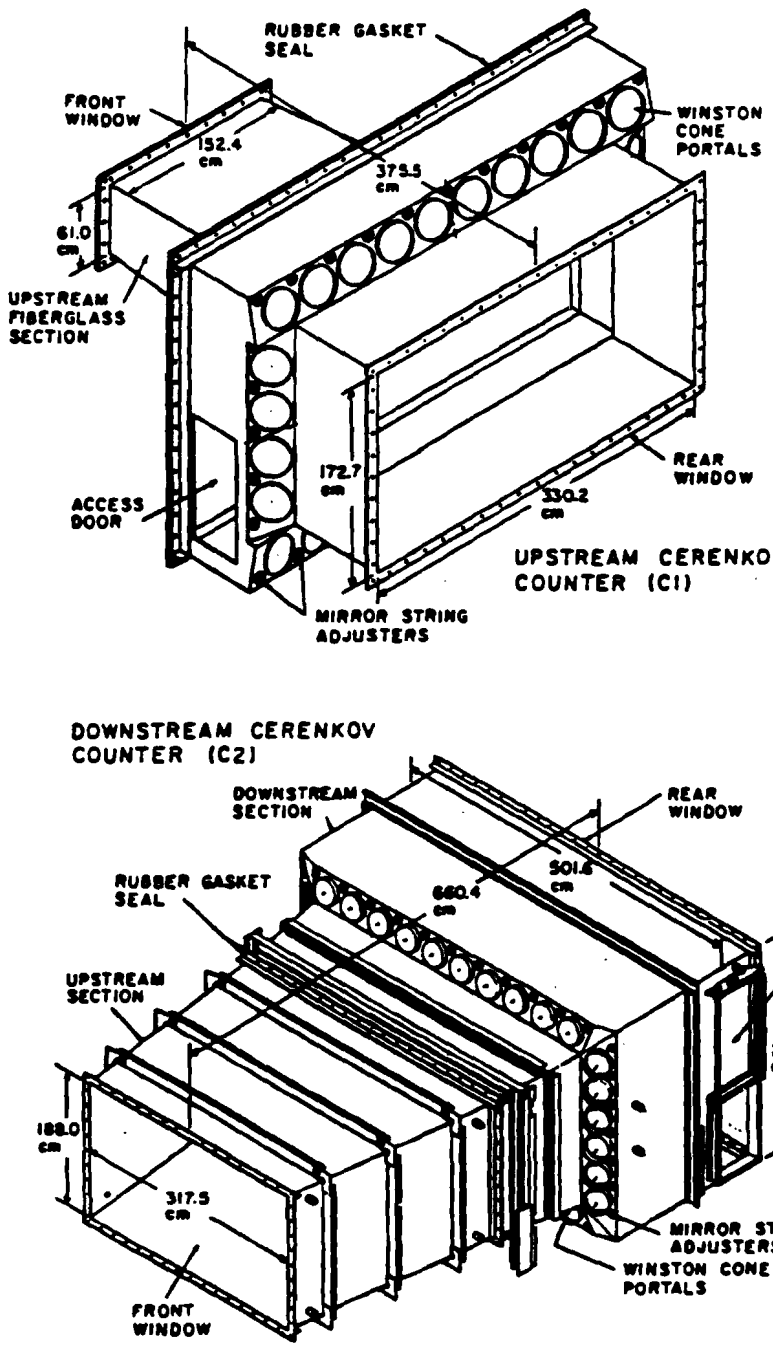

FIGURE 3.5.3. Schematic of the Cerenkov Counters. C1 is shown in (A) and C2 is shown in (B).

C1 MIRROR ARRAY

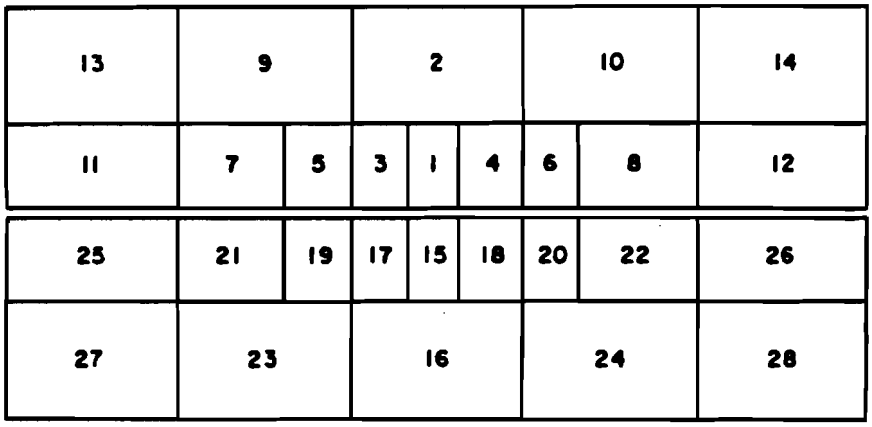

C2 MIRROR ARRAY

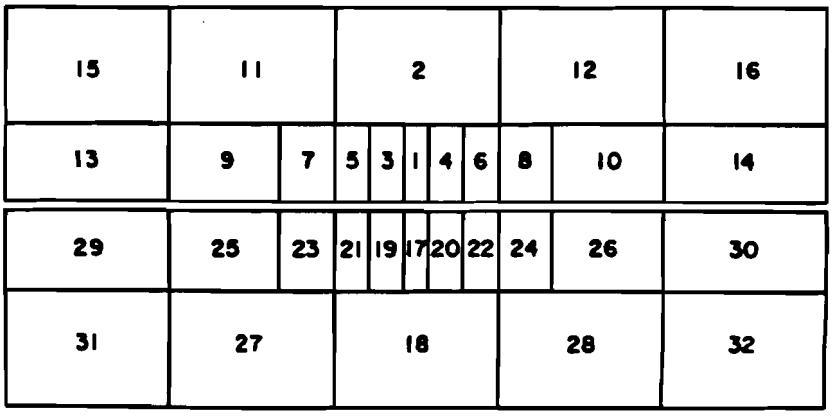

FIGURE 3.5.4. Mirror Patterns of the Cerenkov Counters.

The mirror segmentation pattern was chosen, using Monte Carlo techniques, to reduce the chance of two tracks throwing light on the same mirror, since good Cerenkov identification requires a unique knowledge of the light produced by each track. The minimum mirror size allowed in this segmentation scheme ~ contained the light pattern thrown by a centered high momentum track (maximum radius of Cerenkov light pattern= 8.4cm(C1) or 8.7cm(C2)). With this mirror arrangement, the chance that two (or more) tracks would radiate any one mirror in C1 or C2 was < 10%.[29]

The mirrors were slumped by industry[30] and coated at the University of Colorado. Window pane glass was used for the mirrors in both C1 (2.4mm thick) and C2 (3.2mm thick) and was slumped with a focal length of 190±20cm. Mirrors with major surface distortions were not accepted. The aluminum was deposited on the mirror at a deposition rate of ~ 35 $\AA$/sec for 30sec at ~ 10^{-6} Torr and was overcoated with a 250$\AA$ layer of MgF_2 to prevent oxidation of the aluminum surface. Reflectivities were then tested at small wavelengths (2525$\AA$) since, for Cerenkov radiation, $N_\gamma \propto 1/\lambda^2$ (see eqn 3.5.2). The apparatus used to test these reflectivities is shown in fig 3.5.5. To begin the test, an ultraviolet light source, equipped with a low wavelength filter, was placed in position (A) and the phototube output was recorded. The source was then placed at position (B), the mirror was removed, and the phototube output again recorded. This second measurement was used to normalize the first, thus providing a measure of the reflectivity of the mirror being tested. Reflectivities of ~ 85% were standard and any mirror with < 80% reflection efficiency was rejected (Fig 3.5.6). The performance of the Cerenkov counters is a direct measure of the high quality of these mirrors.

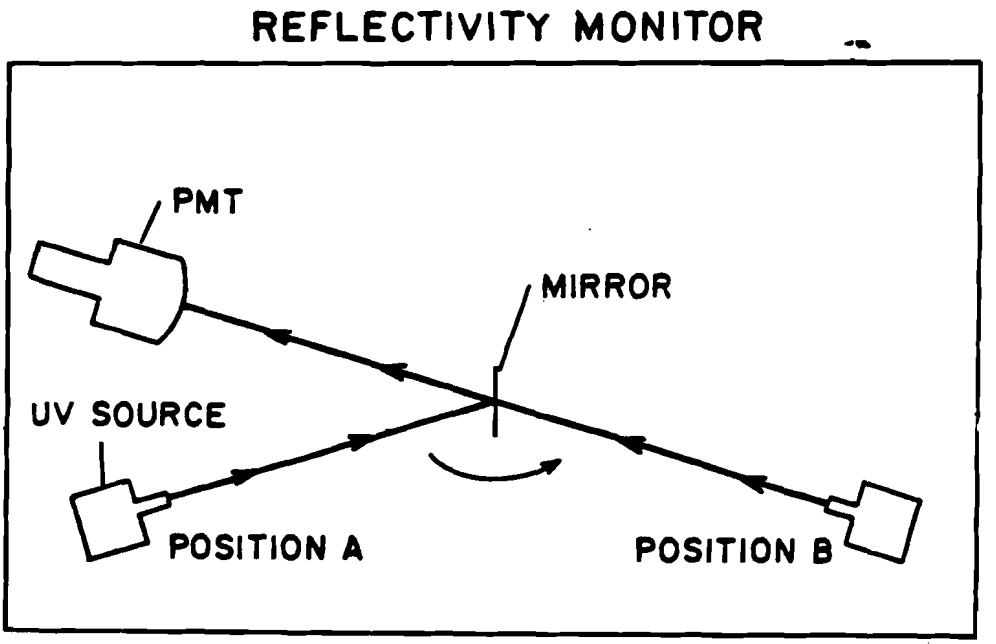

FIGURE 3.5.5. The Mirror Testing Apparatus. The light pathlength from position B to the phototube is equivalent to the pathlength from position A to the phototube.

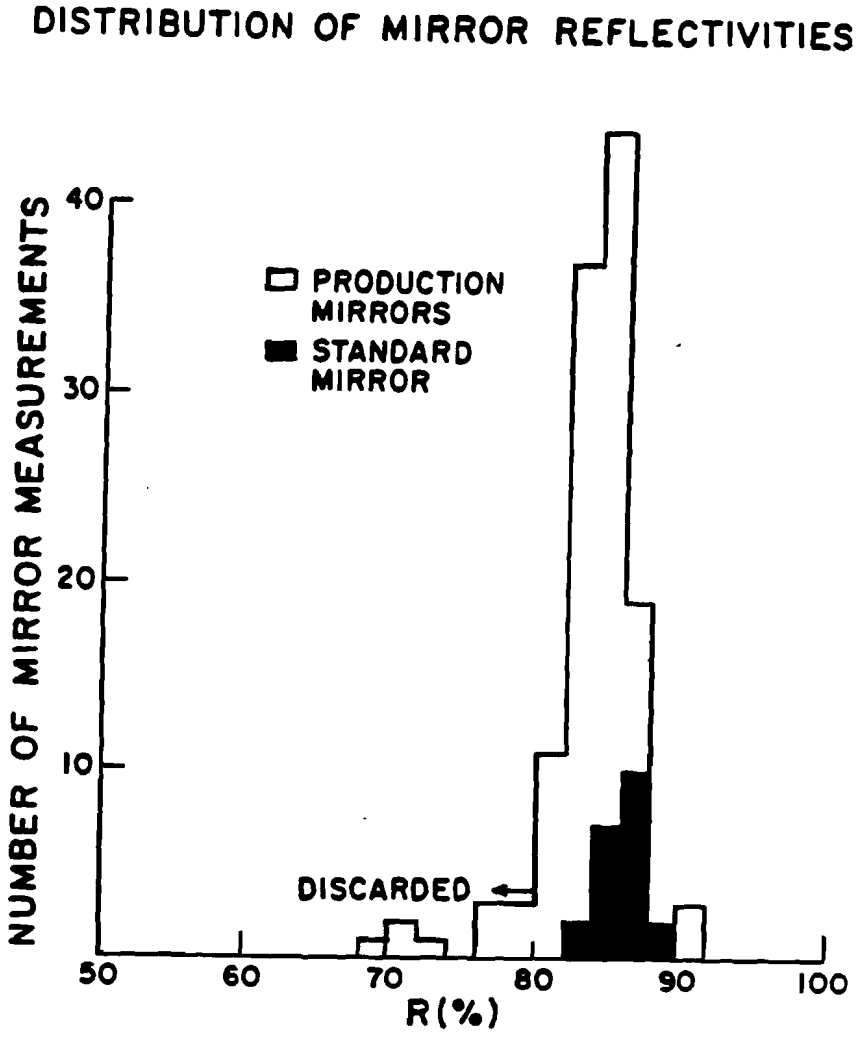

FIGURE 3.5.6. Distribution of estimated Cerenkov mirror reflectivities. Results using the standard mirror coated by Acton Research Corp[31] is shown in black. The reflectivities are measured for light of wavelength 2525Å.

(A)

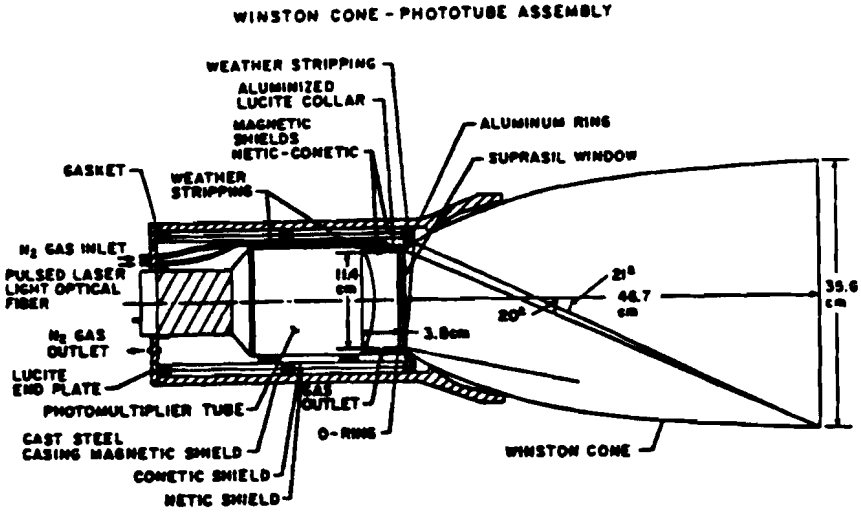

(B)

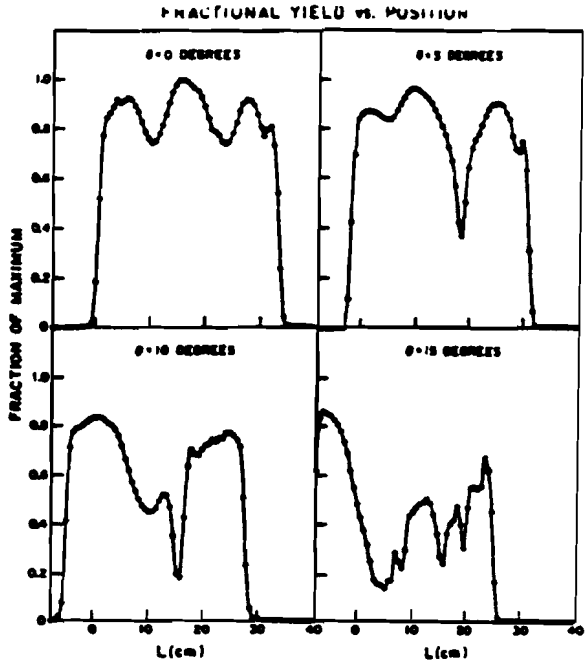

FIGURE 3.5.7. The schematic of a typical Winston cone is shown in (A). The response of the Winston cone to light incident at different angles with respect to the cone axis is shown in (B).

The mirror plane focused the circular Cerenkov light pattern impacting them into rings of characteristic radius r = f×tanθ_c, where f is the focal length of the mirror and r is measured in the focal plane of the mirror. Ellipsoidal cones (Winston cones, fig 3.5.7a) were positioned at the focal plane of the mirror to direct these rings of light onto the phototubes which were attached to the back of the cones. The cones were constructed of nickel, .16cm thick, with a 'flash' of copper deposited on the inner surface followed by 300$\mathring{A}$ of aluminum and 100$\mathring{A}$ MgF_2. They were designed to reflect the Cerenkov photons onto the phototube face with one bounce while rejecting photons with angle of incidence greater than 20 degrees, thus cutting background light down to a negligible amount ($\sim$ 1-2 photoelectrons) (fig 3.5.7b).

The phototubes used were RCA 8854s which have a gallium-arsenide doped cathode of high quantum efficiency ($\sim$ 25% for λ = 4000$\mathring{A}$).[28] The gain of the first stage is an order of magnitude better than the gain of an undoped cathode and thus the signal obtained from a true photoelectron will be enhanced with respect to noise generated at any of the other thirteen stages. This allows for easy phototube calibration since one can actually see the Single Photoelectron Peak (SPEP) (see figure 3.5.8). Note that the second and third photo-electron peak are also evident (Fig 3.5.8a). The surface of the phototube was coated with a wave shifter (p-terphenyl) so that the short wavelength photons preferentially produced as Cerenkov radiation could then be absorbed and shifted to a longer wavelength for which the phototube is generally more efficient.[32]

The phototubes were powered by LRS HV4032A[33] (32 channel) high voltage supplies which supplied $\geq$ 3000kV to each phototube. We ran these supplies very near maximum voltage (3300kV max) on every channel and, for

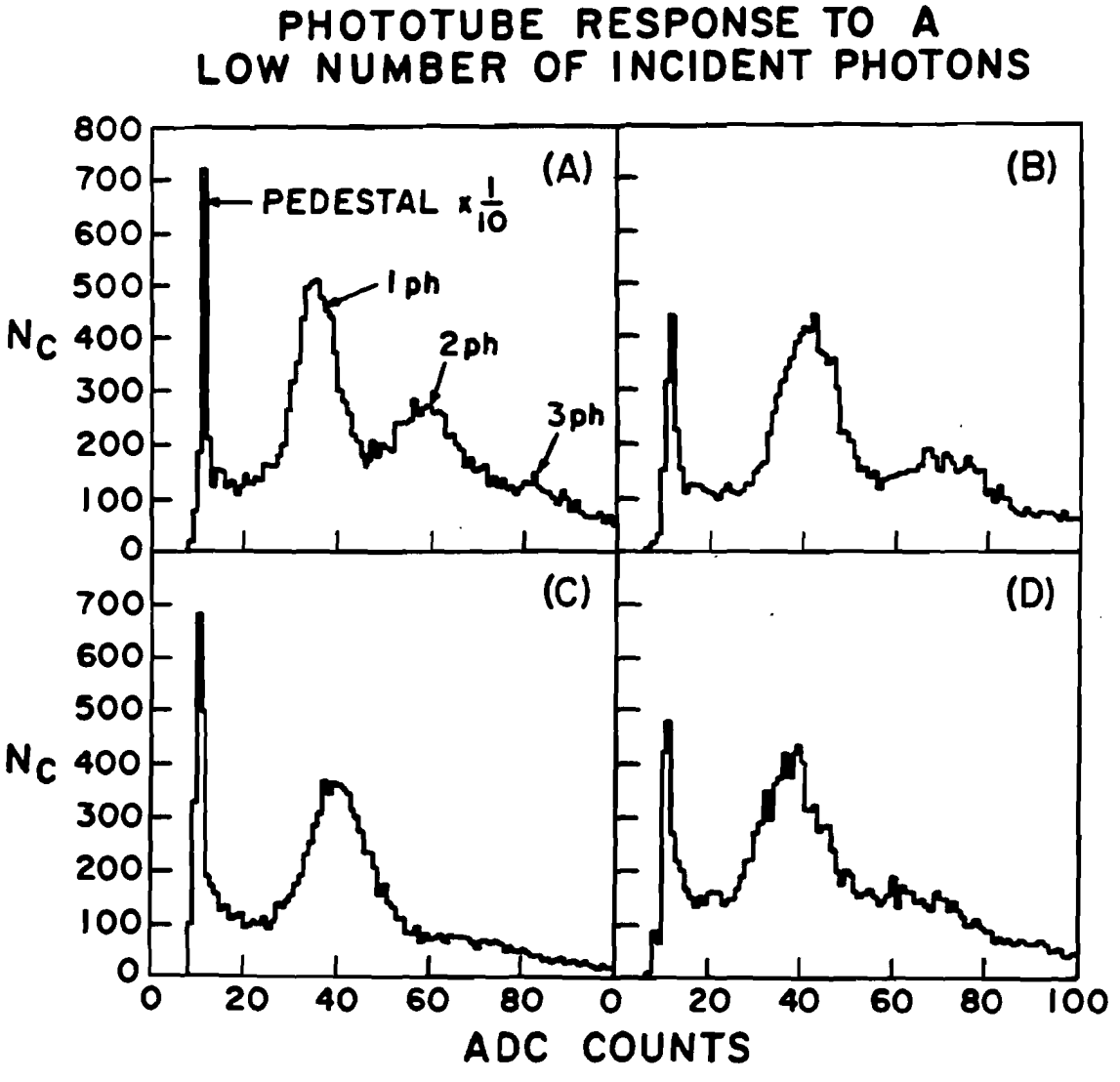

FIGURE 3.5.8. The single photo-electron peaks of four different phototubes are shown. The SPEP is clearly displayed in each case, with multiple peaks evident (A).

C2 at least, used every channel available. A channel would fail if it couldn't maintain it's chosen voltage. Their performance was erratic; supply failure was the most bothersome hardware problem during the run.

The signals produced by the phototubes due to the Cerenkov photons were fed into an LRS 2249 ADCs[33] which were set so that one accepted photon gave about 30 ADC counts above pedestal (SPEP=30) as in figure 3.5.8. The pedestal (NPED) for these devices was set at about 30 counts. Once one has set the SPEP for a given phototube, counting the photons seen in this phototube during an event is trivial, given the ADC output = NADC;

$$NPH = (NADC - NPED)/SPEP \qquad (3.5.3)$$

The maximum readout of the ADC is 1024 so we could detect greater than 30 photons at any one time in any given phototube.

Other design characteristics common to both counters included a system of baffles set up at beam height ($\pm$ 3.5cm from y=0) to eliminate light from the e^+e^- pairs produced by the photon beam (again, using the electron-photon collinearity intrinsic to pair production). On average, an electron traversing this region would generate only $\sim$ .5 photoelectrons. The counters were also painted black on the inside to reduce background light reflections.

The two Cerenkov counters differed in some ways. To minimize interactions, dacron strings were used in C1 to hold the mirrors in place whereas in C2 we used an aluminum frame since interactions weren't as much of a concern at that point. The C2 phototubes also had to be specially protected from the helium in that counter since it could penetrate the phototube and

degrade its vacuum if unhindered. At these high voltages, phototube breakdown (caused by avalanching of knock-off electrons from the helium that had leaked into the phototube) would soon occur and the phototube would be rendered useless.[34] In order to prevent helium from reaching the phototube face, the mouth of the Winston cone was sealed with a Suprasil[35] quartz window (90% efficient for light transmission down to 1600Å) and the region between the window and the phototube was flushed with dry nitrogen (fig 3.5.7a). One phototube was lost to helium poisoning when a hole in one of its RTV seals was overlooked. For C1, the quartz windows were removed and the N_2 gas was held at a slight overpressure to counteract O_2 contamination.

Another major difference between the two Cerenkov counters was that C1 was placed in the field of the second magnet. For this reason, the snout of C1 (see fig 3.5.3a) was constructed of fiberglass to prevent eddy currents, produced by accidental magnetic field changes, from damaging the counter. The path a C1 photon took to its Winston cone included one extra bounce (figure 3.5.9) so that the phototubes could be placed as far away from the magnetic field as possible. This makes sense since a spurious magnetic field can bend the photoelectrons away from the first dynode and severely degrade the output of the phototube. Further protection included to control this effect was a set of three shields; a large massive iron pipe used to cut out large fields, and two thin, very high permeability inner shields (of netic-conetic material) to contain the flux from smaller residual fields. Despite all these precautions, this protection had to be augmented for the C1 phototubes. When the magnets were on, nearly all C1 phototube efficiencies dropped and for one particular phototube, the efficiency went to zero. This problem was solved using 'bucking fields' generated by wrapping $\sim$ 100 turns

of wire around the large iron pipes and running DC current through them at the value that maximized the 'magnet on' efficiency of the phototube in question. Since any current could be chosen and any number of turns of wire used, a reasonable solution was found for each problem tube. In the worst case, the phototube with zero 'magnet on' efficiency was brought up to 80% of its 'magnet off' value.

The magnetic field in C1 provided one further complication. It would bend the particles traversing the counter as they emitted their Cerenkov light. The light pattern at the mirror wall would then spread horizontally into the shape of an ellipse which the mirrors would focus into an elliptical ring at the mouth of the Winston cone. The horizontal dimension of the ring depended on the magnetic field strength; as the field increased, the acceptance of the photons decreased.[29] From the three current settings for which the magnets were mapped, the medium strength field was chosen, given this acceptance consideration and the normal resolution considerations.

3.5.2 Monitoring

As discussed above, the counter design was motivated by a desire to generate an adequate number of photoelectrons for each track. In addition, the apparatus had to operate in a stable manner to ensure successful particle identification. The counters were monitored to make sure that not only were the individual cells working, but that they were stable.

Throughout the run, in between spills, test triggers were taken during which the phototubes were pulsed with filtered laser light passed through a single light fiber. Changes in the response of the phototubes to this light would give the first indication of a change in the performance of the phototube or of the phototube readout. The Cerenkov On-Line Monitoring System

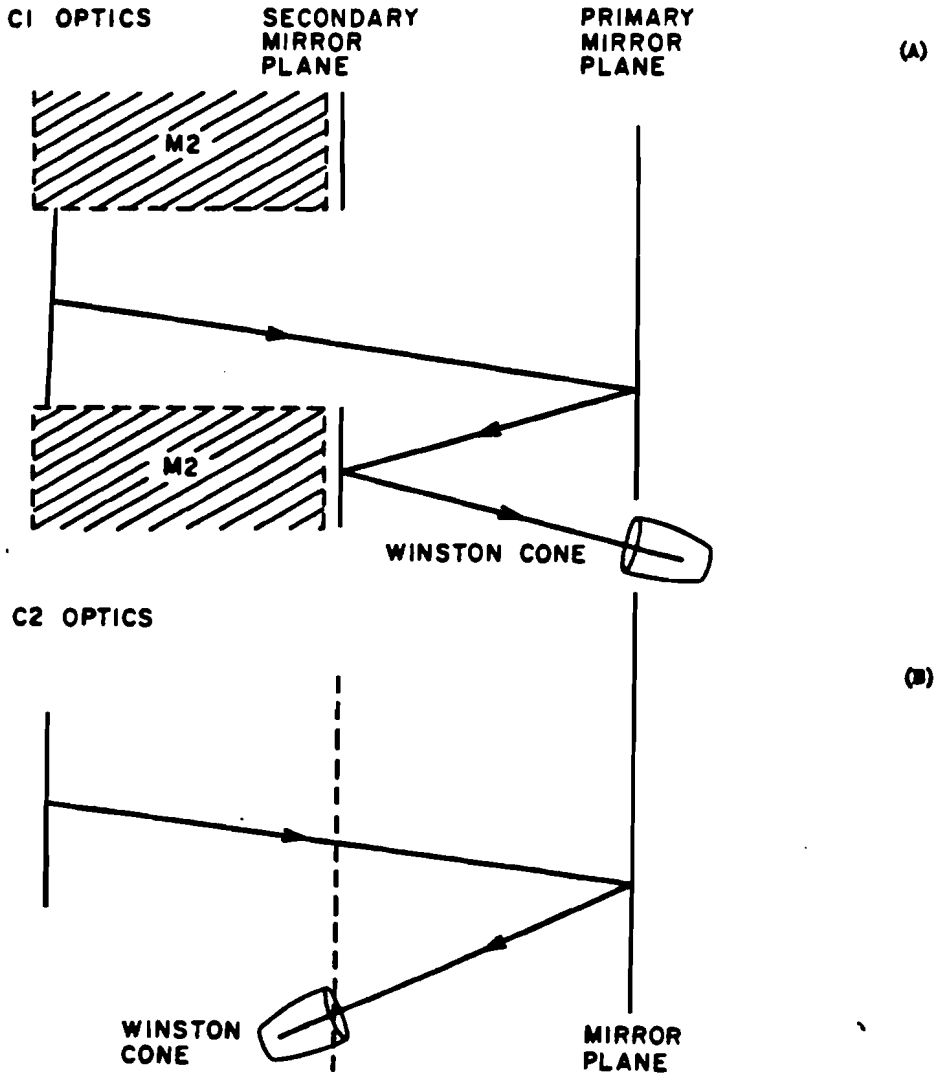

FIGURE 3.5.9. The path taken by the cerenkov light in C1 (A) and C2 (B) is shown. Note the presence of the second magnet in (A).

(OLMS[26]) program would compare each phototubes' response to its benchmark value and issue alarms if the response was outside the set limits. Test triggers were also taken without pulsing the phototube with laser light to monitor the pedestals. In this manner, the detector components from the phototube to the ADC were monitored effectively.

An additional technique that monitored the condition of all the Cerenkov elements involved accumulating the output of the cells during physics events. These cell outputs were compared one to another and also to a standard plot that showed the response of all the cells during good running conditions (Fig 3.5.10). The response of an entire Cerenkov counter, and thus its gas purity, could be monitored by comparing newly generated cell output profiles with this standard. Individual problem cells could also be monitored by watching their response, relative to the other cells, degrade with time. Finally, the gas composition and oxygen contamination of the counters were tested bi-weekly using a gas chromatograph whereby we could track the helium, nitrogen, and oxygen percentages in the counters.

Almost all the problems that came up were detected in the test triggers since almost all the problems we had were in the equipment monitored by them. The mirror and Winston cone reflectivities and positions were remarkably stable throughout the run (APR 85-AUG 85), as the gain curves in figure 3.5.11 show.

3.5.3 Calibration

The calibration of the Cerenkov counter had to provide the SPEP's, the PED's, and the gains and widths of each phototube as well as the threshold behavior and alignment constants of each counter. These numbers were

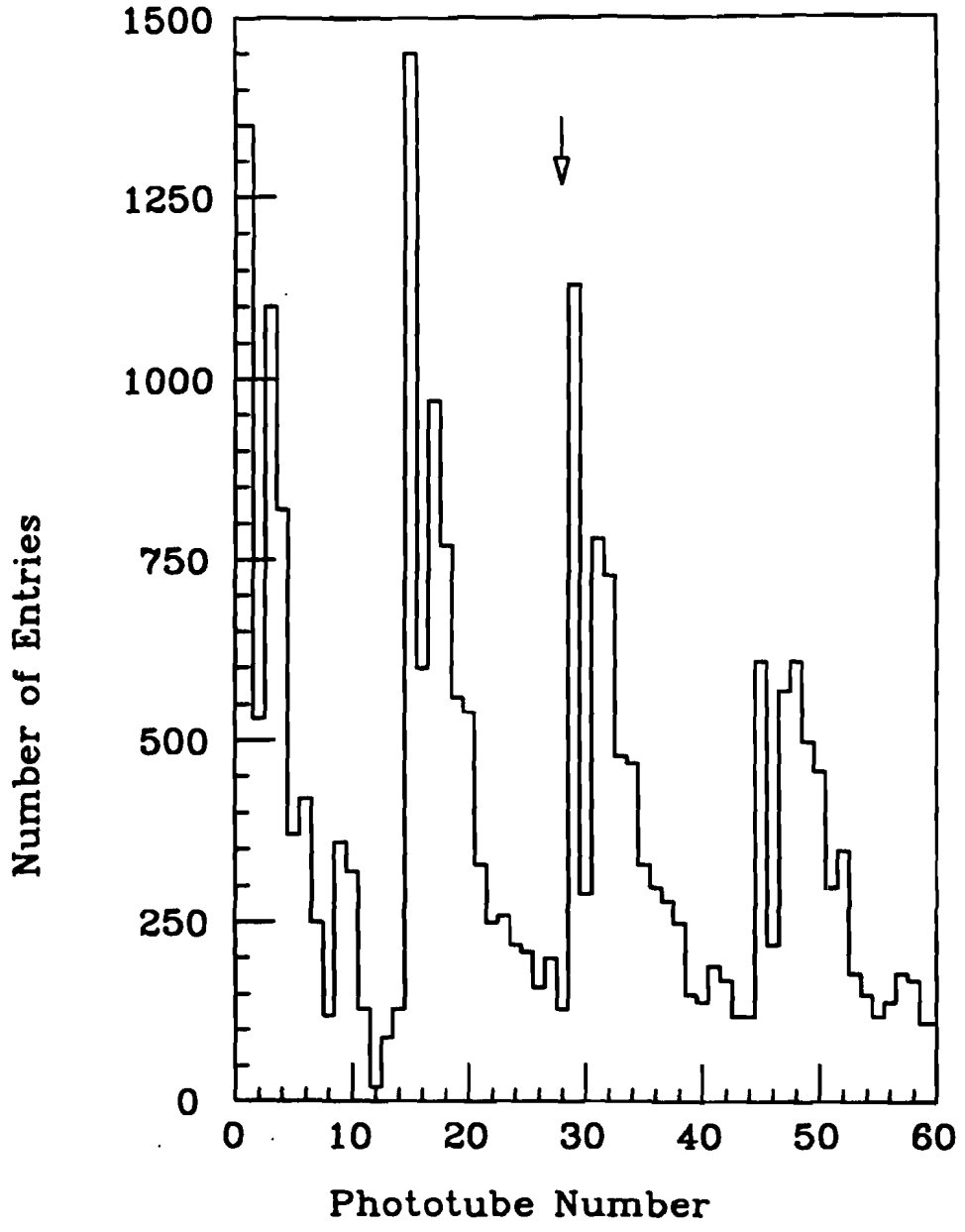

FIGURE 3.5.10. The response of all the cerenkov phototubes to data events is displayed. The C1 phototubes are plotted to the left of the arrow (entries 0-28), the C2 phototubes to the right (entries 29-60). The cells with the high response are the closest to beam center.

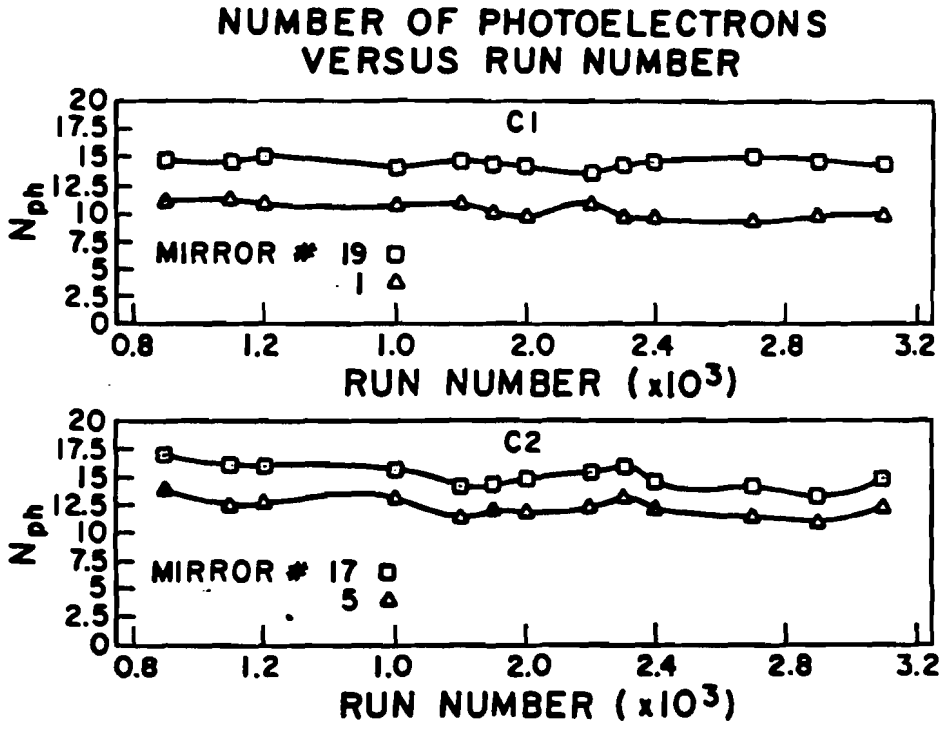

FIGURE 3.5.11. Gain curves for two cerenkov cells are displayed. The gain of a cell is the final measure of its performance since it is the "maximum average response of the cell to a single track".

regenerated after any noticable change in the cerenkov performance; we generated different calibration constants for $\sim$ every 100 runs.

The SPEP's and PED's were taken straight off the raw data tapes. Single tracks centered on a given mirror would generate $\sim$ 12 photoelectrons in that cell (as discussed below) but the typical response of the phototubes during data events was < 1 photoelectron since, in any given event, most mirrors are not impacted by a track. As noted earlier,the SPEP's and PED's obtained from the raw data are quite pronounced (see fig 3.5.8).

The gain of a given phototube was obtained by selecting a subset of tracks from the data which impacted the mirror associated with the phototube, were well separated from other tracks, and had momenta well above the pion threshold; so called 'pristine' tracks. Generally, only a fraction of the light from these tracks hit the mirror in question (must be $\geq 50\%$) so the phototube response had to be scaled up by the missing fraction to get the gain. The gain of a phototube is the average of this scaled up response distribution or, more succinctly, it is the maximum average response of a given cell to a single track. It is also the definitive measure of the performance of that cell. Table 3.5.2 presents the gains of each cell.

The 'widths' mentioned above are more accurately described as the deviation of the phototube response distribution from a pure Poisson. The response distribution is fit to a *compound* Poisson distribution;

$$P(N,\mu,b) = \frac{\mu^N}{N!}(1+b\mu)^{-N-1/b} \times \prod_{m=1}^{N-1}(1+mb) \qquad (3.5.4)$$

where the parameter μ is the gain as defined above (held constant in the fit) and b measures the deviation of this distribution from a pure Poisson (b=0).

Although each incremental element of the photocathode emits photoelectrons with a Poisson distribution, the integrated response of the photocathode is described more accurately with the compound Poisson distribution because of the variation of the photocathode conversion efficiency across the face of the phototube. The b parameters were derived once and assumed to hold constant throughout the run (in all cases, b<10%). With a well defined model for the response of the phototube, we could compare the number of photoelectrons obtained for a given track, NPH (eqn 3.5.3), with the expected number for each viable mass hypothesis and, thus, were able to derive the probabilities for this track. The details of this process are given in section 5.2.2.

We began the process of aligning the Cerenkov mirrors with respect to the drift chamber coordinate system by measuring the positions of the mirrors relative to one another. A set of isolated, high momentum tracks similiar to the set used to generate the gains was then selected. As we varied the position of each central mirror within the mirror plane, the subset of tracks that impacted the mirror at each new position was determined and the frequency with which these tracks prompted a response in that mirror's phototube was plotted. The x-y position of the mirror evoking the highest response rate was chosen to be the "true" mirror position as measured in the drift chamber coordinate system. The x-y offsets that were derived for the central mirrors were then applied to the entire mirror set.

The final step in the calibration was to determine the threshold behavior of the counters. We used isolated tracks of varied momentum and observed the measured radiation in all the cells affected by this track as a function of momentum, assuming these tracks were mostly pions. A fit (fig

Table 3.5.2: Cerenkov Cell Gains for C1 and C2

Mirror	C1	C2	Mirror	C1	C2
1	11.1	13.2	17	10.4	16.2
2	15.0	14.6	18	9.8	9.6
3	14.4	14.2	19	14.6	11.4
4	12.3	12.6	20	16.4	14.4
5	8.0	12.9	21	13.9	17.0
6	18.2	13.9	22	14.0	13.9
7	10.8	13.7	23	14.2	14.1
8	7.5	12.3	24	11.1	14.3
9	12.9	16.3	25	14.7	12.5
10	9.9	14.9	26	15.1	9.1
11	14.3	13.2	27	7.8	6.9
12	13.3	7.6	28	14.6	9.4
13	12.1	13.3	29		14.0
14	16.6	13.8	30		13.4
15	18.0	12.6	31		16.2
16	22.2	12.2	32		13.0

3.5.12) to the observed number of photoelectrons was performed over a momentum range which was below the kaon radiation threshold, thus excluding kaon or proton contamination. The fit near the pion threshold was of the form $1 - p_{th}^2/p^2$. This behaviour as a function of momentum was included in the reconstruction algorithm (see section 5.2.2).

3.6 The SLIC and Pair Plane

Many important charm decay channels require good identification of either a π^0 or a high momentum electron ($D^0 \rightarrow K^-\pi^+\pi^0$, $D^0 \rightarrow K^-e^+\nu$). The SLIC, Scintillator Lead Interleaved Counter, was used to identify and provide the energies and positions of electrons, positrons, and photons. Two photon combinations were then used to form π^0s. In addition to this, the SLIC was an integral element of the triggers.

The SLIC is shown in figure 3.6.1. It has 60 layers, each composed of .32cm of lead and 1.3cm of liquid scintillator. This is the equivalent of 20 radiation lengths (and 2 interaction lengths) of material. The scintillator was isolated from the lead (which would poison it) and segmented by corrugated aluminum panels with corrugations of 3.2cm in the central region of the counter and 6.4cm in the less confused outer region. These panels were layered perpendicular to the beam with the corrugations either horizontal (Y view), or at $\pm 20.5°$ to the vertical (U, V view respectively). The aluminum panels were coated with teflon and since teflon has a lower index of refraction than the scintillator, light emitted in the scintillator at $< 20°$ to the teflon surface was totally internally reflected. This scintillator light could then be efficiently transported to the light collection apparatus.

The segments in the z direction in each of the three views were collected into a single channel by a waveshifter bar (see fig 3.6.1). This

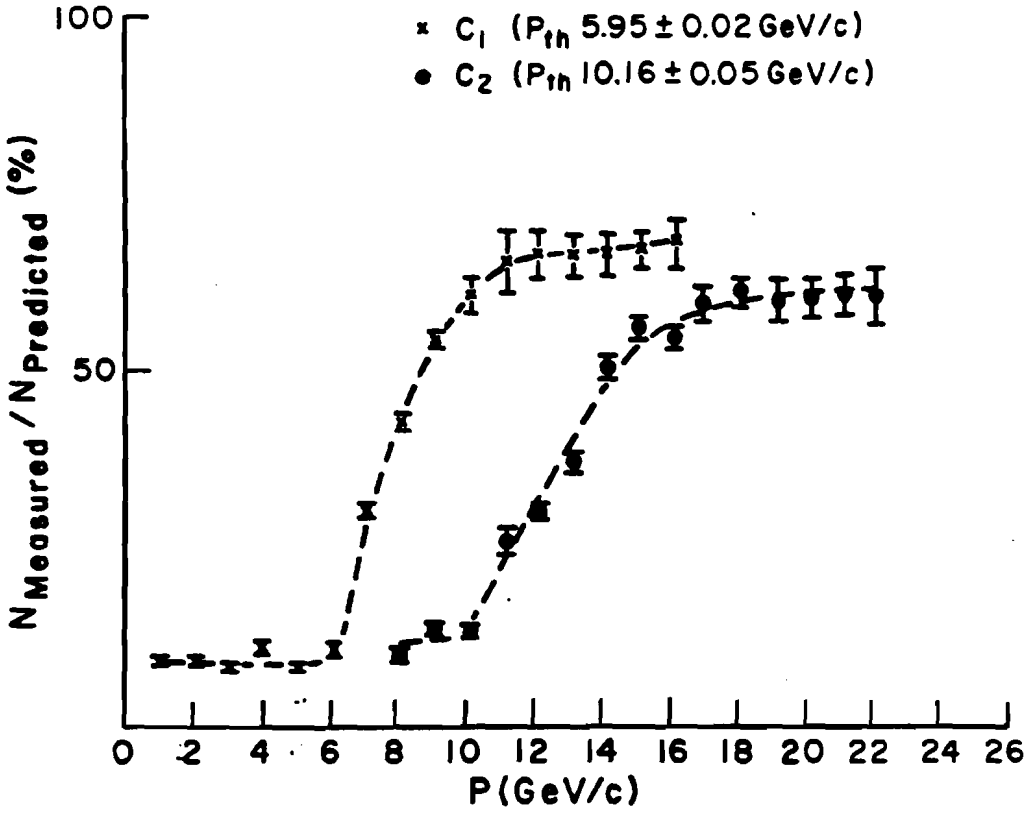

FIGURE 3.5.12. The momentum threshold of both Cerenkov counters is displayed. The curves are generated with light emitted by pions only (the curves are cut off before the kaon light threshold is reached). The fraction of light measured well above threshold is < 100% because some of the light emitted by the track misses the mirror being sampled.

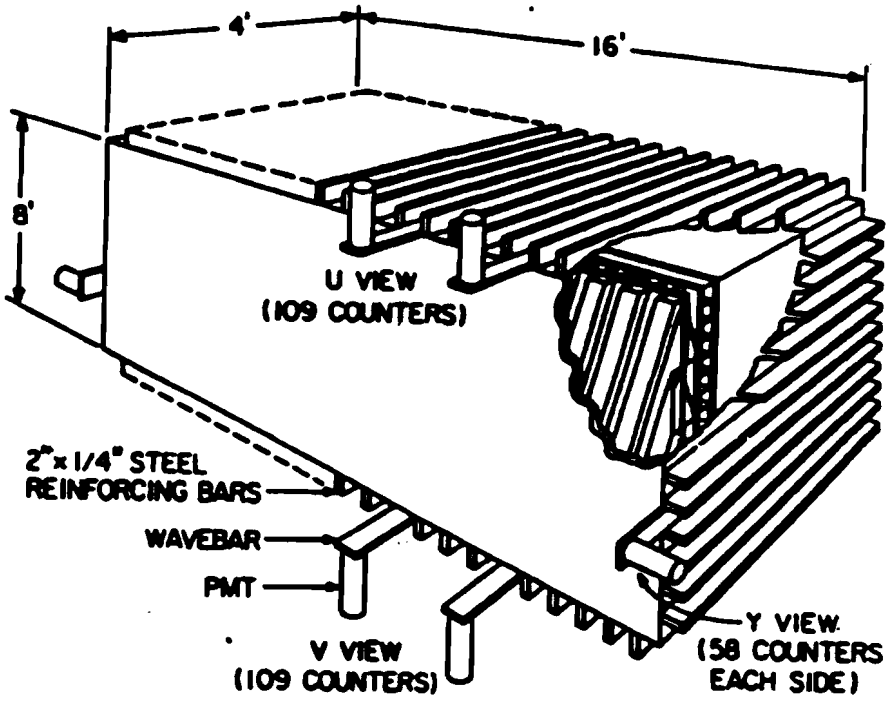

FIGURE 3.6.1. Schematic of the Lead/Liquid Scintillator Shower Counter (SLIC).

bar shifted the ultra-violet scintillator light into green light for which the phototubes (2" RCA4902 in the central region/3" RCA4900 in the outer region) were more efficient. The anode output of the phototubes was read into LRS 2280 ADCs while the dynode signal was fed into the trigger. The U and V views had 109 channels each, read out at the top and bottom of the counter respectively while the Y view had 116 channels with half read out on the east side and half on the west side of the detector.

The same clean muons used to calibrate the drift chambers were used to calibrate the SLIC. Pairs were also used to check the consistency of the muon calibration, at least in the central counters accessible to them. Details of the calibration are discussed elsewhere.[22]

The pair plane was a set of 19 counters lined up in x and placed directly behind the last drift chamber assembly (D4), at beam height. These absorption counters constituted 20 radiations lengths of material and were followed by 10 radiation lengths of lead. The C-counter, discussed in section 2.3, was the central pair plane counter. The pair plane was to serve two functions, to help filter pairs out before they reached and flooded the SLIC, and to measure the energy of the particles that it absorbed. As in the case of the C-counter, the congestion in this region prevented us from making reliable measurements of the energies of the absorbed particles.

3.7 The Hadrometer

Good neutral hadron detection would have given us access to some otherwise inaccessible charm decay modes (e.g. modes with $\Sigma^- \rightarrow n\pi^-$ (100%)). Unfortunately, the fractional energy resolution of the hadrometer was 75% / $\sqrt{E}$ which prohibited effective analysis. The default responsibility of the hadrometer was as an element of the triggers for which it played an

important role. It was also used as a hadron veto for the SLIC and to augment the muon identification.

The hadrometer was a multilayer steel and scintillator sandwich (fig 3.7.1) used to detect energy from hadron showers and from the passage of muons. It was comprised of an upstream and downstream module, separated by a 5cm airgap, and with 18 layers in each module. The layers contained 2.5cm of steel and 1cm of scintillator each. The hadrometer provided 2 views, X and Y, which were alternated with each layer, and read out on the top (X view) and on the sides (Y view). The 38 Y and 33 X channels were formed by summing, in the z direction, the nine channels belonging to each view in each module. These signals were transported by lucite lightguides to 5" EMI 9791KB phototubes and readout by LRS 2280 ADCs.

The hadrometer was calibrated cell by cell using the same set of calibration muons as the SLIC. This was an important task because the dynode outputs from the hadrometer channels were used in the E_t trigger. Details of this calibration process are found elsewhere[22] .

3.8 The Muon Wall

The main function of the muon wall was to detect high energy muon pairs for the J/ψ analysis. It was also used in coincidence with the front muon wall to trigger the calibration muons used in the drift chambers, the SLIC, and the hadrometer.

The wall of 46cm and 61cm scintillators used to detect the muons was separated from the hadrometer by $\sim$ 100cm of steel. Low energy muons and effectively all hadrons were absorbed before reaching the wall. The scintillator light was transported by lightguides to 5" EMI 9791KB phototubes, the outputs were discriminated and latched, and the discriminator output

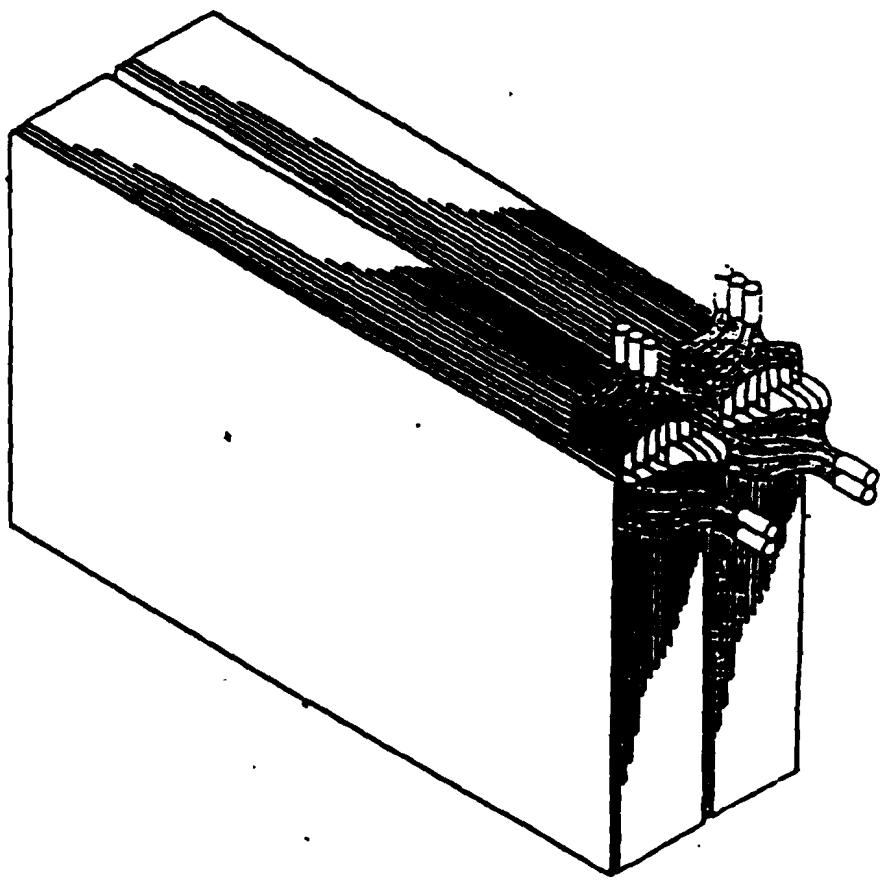

FIGURE 3.7.1. Schematic of the Hadrometer.

used to stop a TDC from which we could obtain a measure of the y position of the muon. The efficiencies of the counters and the reference values for the TDCs were derived by setting a double paddle counter behind each muon counter at 3 different positions and requiring a triple coincidence of this muon counter with the paddle counters.

CHAPTER 4

THE DATA ACQUISITION SYSTEM

The data acquisition system consisted of the data selection logic and the data readout and recording systems with which the raw input from the spectrometer was chosen, ordered, and written to tape. This chapter is divided into two sections, the first of which deals with the triggers used to select our data while, in the second section, the details of the data recording are discussed.

4.1 The Physics Triggers

There were two main triggers employed during the E691 data run. They were chosen to enhance the charm content of the data at the expense of the hadronic and electromagnetic backgrounds. The hadronic trigger (TAGH) required a deposit of 40 GeV/c^2 of hadronic energy in the calorimeters (the SLIC and the hadrometer) and eliminated most of the electromagnetic background. The transverse energy trigger (E_t) required that this energy deposition have a reasonable component transverse to the photon beam direction of $\geq$ 2.2 GeV/c^2 . The bulk of our data (87%) was taken with the E_t trigger because Monte Carlo studies had indicated that TAGH data with $>$ 2GeV/c^2 transverse energy would have $\sim$ double the charm content of a sample selected with only the unbiased hadronic trigger. In general, the high mass of the charm particle leads to higher average transverse momentum for the charm decay products. Upon completion of the experiment, a tranverse

energy cut of 2.2 GeV/c^2 was applied to the TAGH data sample. The resultant sample contained 80% of the charm found in the original sample yet contained only 1/3 as many events; an enhancement factor of > 2.5.

The TAGH trigger required the coincidence of an interaction (detected by the B-counter) and a 40 GeV/c^2 deposition in the calorimeters. No TAG was required. The E_t trigger, besides requiring > 2.2 GeV/c^2 transverse energy, needed either a TAGH with a good TAG or a TAGH with a minimum energy deposition of 70 GeV/c^2 in the calorimeters (to allow for poor tagging of very high energy photons) *plus* some minimal response from the first Cerenkov counter (C1). This last coincidence was necessary because the PCENTER beam would periodically flood our experimental hall with muons that, combined with a typical hadronic interaction, would imitate an E_t event beautifully.

The E_t and TAGH trigger schematic is shown in figure 4.1.1. All the dynode signals from the SLIC and the hadrometer were input to LRS 628 NIM modules at Level 1. The dynodes in each individual module were from counters approximately equidistant from the SLIC or hadrometer detector center. At this point, the SLIC output was attenuated by 12dB, as indicated by the relative calibration of the two calorimeters, and summed with the hadrometer output to form the hadronic energy. The relative transverse energies of each module were formed at Level 2 by attenuating the Level 1 outputs with the appropriate resistors. They were summed at Level 4 to get E_t where, again, the SLIC response had to be attenuated by 12dB. At each level, the output was sampled and monitored to ensure the performance of the trigger. The E_t signal was then fed into a charge discriminator module

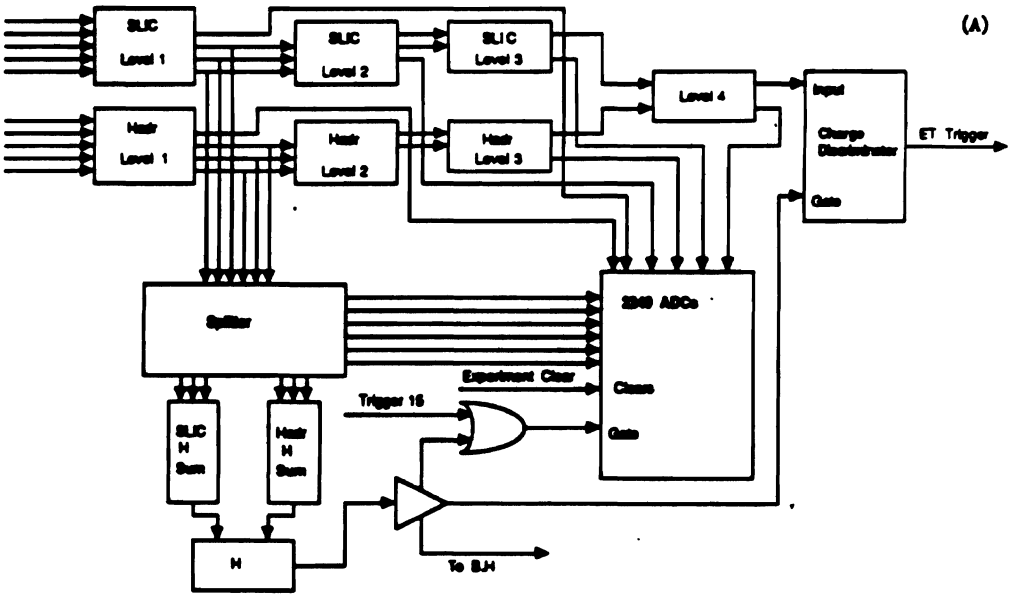

FIGURE 4.9.1. The E_t trigger logic is shown in (A). A schematic of both the TAGH and E_t triggers is shown in (B).

with which we applied the E_t cut on our data. The discriminator unit was calibrated along with the calorimeters and we obtained the relation;

$$E_t = .36 + .4\times N \text{ where N=discriminator setting}$$
$$=4.5 \text{ for } E_t > 2.2\text{GeV}/c^2 .$$

From figure 4.1.2, it appears that choosing $E_t > 2.2\text{GeV}/c^2$ was rather conservative. However, the experimental deadtime rose with E_t and, since maximizing the charm written per second was our goal (and not maximizing the charm written per tape), the E_t cut was set at a lower value than this simple curve indicated. A discussion of the dimuon trigger and the other trigger types used in E691 as well as details on the charge discriminator unit can be found elsewhere[26] .

4.2 The Data Recording

The data recording system was responsible for collecting, organizing, and recording onto tape the response of our spectrometer to the photon interaction. For most of our data (93%), the calibration triggers, the E_t trigger, and the dimuon trigger were fed into a logical OR which indicated when an acceptable trigger had been generated (for the other 7% of our data, the TAGH trigger was added to this OR). If this OR was within the beamgate generated by the B-counter, and if the CAMAC was ready to accept new data (the computer wasn't reading CAMAC out to memory or another trigger's response wasn't being digitized) this OR would prompt a BEAM STROBE which began the gates for the ADCs, sent the TDC stops, and strobed the Latches. A BUSY indicator which rejected all new triggers was also set by the computer at this time. If the computer wasn't writing events on tape, this strobe would initiate a computer interrupt so that this event could be transferred from CAMAC to the computer's memory. Once

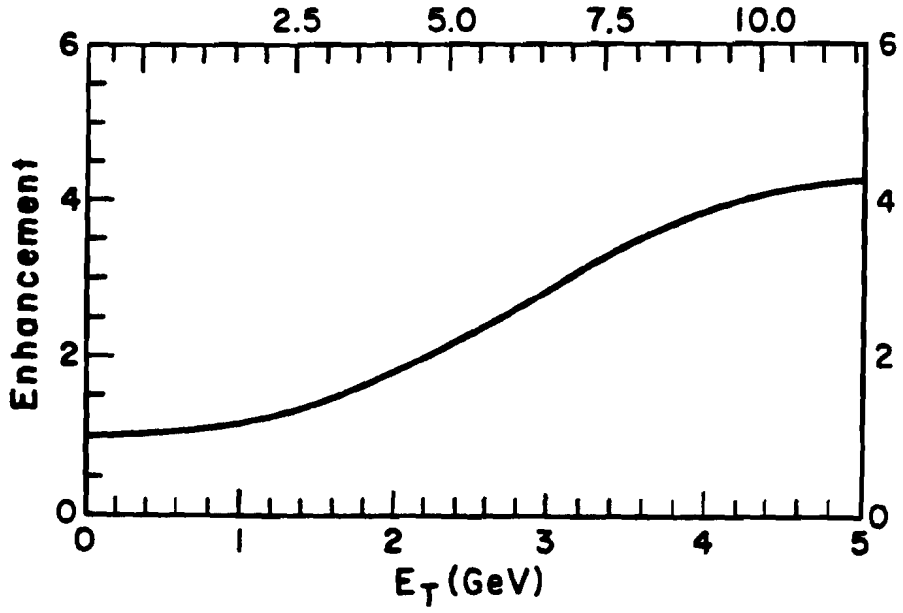

FIGURE 4.1.2. Charm enhancement as a function of transverse energy is displayed. The lower scale gives the transverse energy in GeV/c^2 while the upper scale is the hardware value at which the charge discriminator was set.

the event was safely in the memory, the BUSY was dropped and a CLEAR was sent to the CAMAC modules to ready them for new data.

The fraction of the time that this system was unresponsive to new data is referred to as the deadtime, whether the computer is writing tape or reading out CAMAC, or another event is being digitized. For E691, we had a measured deadtime of $\sim$ 30% while taking data at approximately 100 events/sec. The data acquisition hardware (fig 4.2.1) consisted of a PDP-11/55 computer with fast bipolar memory and two Jorway 411 CAMAC branch drivers for the two CAMAC branches employed by E691. The tapedrive was an STC 1921. It is worth noting that positioning the tapedrive between the CPU and the branch drivers allowed us to write tape while the CAMAC digitized data which almost doubled our DA rates. This would not have been possible if the positions of the tape drive and the CAMAC were reversed because the device closest to the CPU had priority for data transfers.

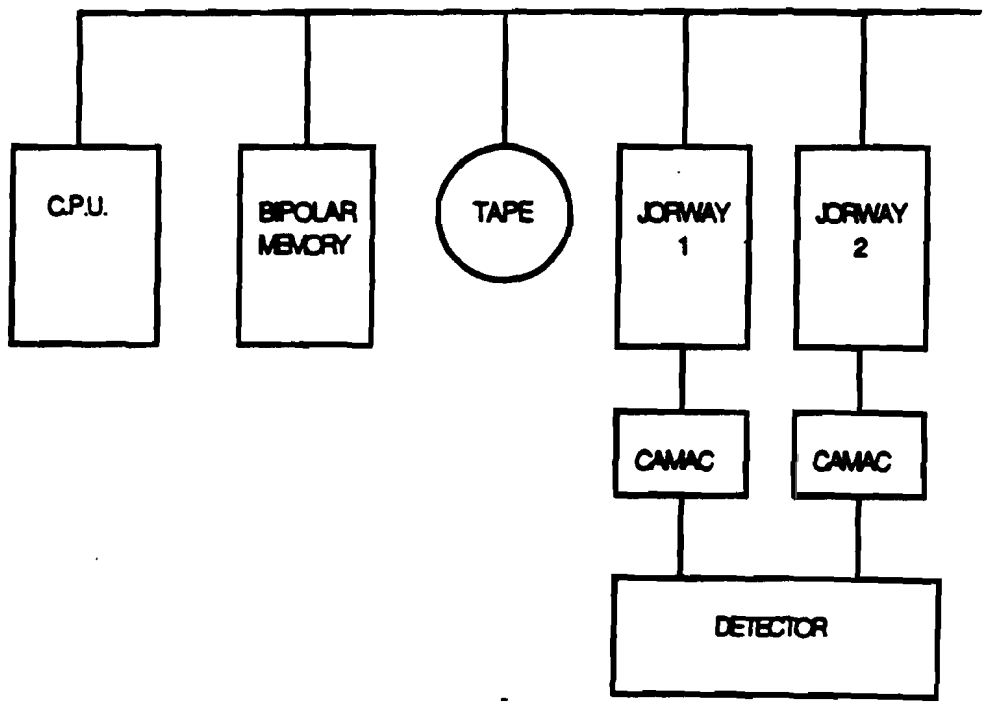

FIGURE 4.2.1. The Data Acquisition System

CHAPTER 5

THE RECONSTRUCTION PROGRAM

The raw data events written at TPL contained many thousands of strictly ordered, scrupulously monitored drift chamber drift times, SMD hits, phototube pulse heights, and set latch bits. These had to be sensibly converted to particle types, positions, and momenta. A computer program, therefore, had to be written which would read in this raw data, interpret it, and output the above information.

The E691 data reconstruction computer program was divided into two steps called PASS1 and PASS2. PASS1 handled pattern recognition (track finding) and the momentum determination, while PASS2 used PASS1 output to reconstruct the raw tagging, SLIC, and Cerenkov information and to find the candidate vertices in the data. On average, PASS1 used .7 Cyber 175 seconds of CPU time per event and PASS2 used .25 seconds per event. Given these reconstruction rates and the size of the Fermilab Cyber Computer system, complete reconstruction of the 10^8 data events written at TPL would have taken $\sim$ 3 years. We were fortunate, however, to have access to a microprocessor farm (the Advanced Computer Program (ACP)), which, since it was dedicated to E691, reconstructed our data $\sim$ 10 times faster than the Cyber system. Due to this dramatic increase, the data set was reconstructed more than a year earlier than had been projected.

5.1 PASS1

The PASS1 program had two main internal routines; S1234 and SESTR. The S1234 routine was responsible for searching the SMD for tracks originating in the target while the SESTR routine was used to find tracks originating downstream of the SMD (e.g. Λ^0, K_s^0 decay products). S1234 ran first and it began by finding the tracks in the region upstream of the first magnet (see figure 3.0.1). The track finding started in the SMD and not the (less congested) drift chambers because of (a) the superior tracking efficiency of this detector, (b) the excellent redundancy (3 planes for each of the XYV views in the SMD, 2 planes for each of the XUV(X′) views in D1) of the SMD/D1 region, (c) the fact that we start the tracking in the region of best resolution, and (d) the high reconstruction rates obtained with this method.

Tracks with three hits in any 2 of the 3 SMD views were considered first. The track segment defined by these 2 views was projected into the third view and tracks with 3, 2, or 1 hits in that view were selected. Tracks with hit patterns of 3-2-2, 3-2-1, and 2-2-2 respectively were then picked up using D1 to help with the views with less than 3 hits. Having established the SMD/D1 track candidates, S1234 would project them into D3 in the Y view (D3 was less congested than D2) and link these tracks to XUV triplets in that drift chamber. Linking was initiated in the Y view because the fields bent the particles appreciably only in the X direction. The X position of a matched triplet established the horizontal bend of the track and thus fully constrained it. Using a single bendpoint approximation for the magnetic fields, we then swam the track through the entire detector and the drift chamber triplets associated with this track were determined. S1234 would

then perform a momentum fit on this track candidate using these triplets, the SMD information, and the full field map of the magnets. Finally, the S1234 routine applied the track quality cuts to this set of tracks; dropping tracks with too few SMD hits, with a bad χ^2 from the momentum fit, and tracks that shared too many hits with a stronger track. The overall tracking efficiency obtained was > 90% for high momentum tracks. This routine took .5 seconds of CPU time on average and one second on average for charm events, which were higher multiplicity events.

The SESTR routine was called at this point to search for tracks originating outside the SMD. It ran quite efficiently, needing only .2 sec/event of CPU time, because hits assigned to SMD tracks by S1234 weren't reused in this tracking package.

5.2 PASS2

5.2.1 The SLIC Reconstruction Program

The SLIC reconstruction was a complex multi-step process. First, the counter outputs were converted to physical energies using gain curves obtained during calibration. Adjacent counters in each view whose energies were above a particular threshold were then grouped into 'cells'. These cells were, in turn, split into 'sectors' which were defined as any set of counters within this cell whose central counter energy was a local maximum. A list of candidate sectors was constructed for each cell.

These candidate sectors were subjected to a stepwise regression fit[36] in order to determine the final set of sectors for this cell and to sensibly distribute the cell energy among them. The fit also generated the sector energy errors which were determined by the significance of the energy deposition in

the sector as well as the nature of the deposition (hadronic or electromagnetic). A list of candidate particles was then created for the event. If well defined energy depositions in the V and Y view could predict the position and magnitude of a U deposition, the YUV triplet was considered a candidate. The set of candidates was subjected to another stepwise regression fit in order to determine the SLIC particle list, the particle energies, and the energy errors.

These particles were then checked to make sure that the showers assigned to them were electromagnetic in character. The probability that the energy deposition associated with a given SLIC particle was electromagnetic was estimated by comparing the transverse energy distribution associated with each particle to electromagnetic shower shapes created by Monte Carlo simulations and stored in the reconstruction code. This check was important because large hadronic showers would often generate smaller 'satellite' showers that could effectively imitate the energy depositions of genuine SLIC particles. Using this comparison, we could filter these 'satellite' showers out. In addition, the probability derived above was included in the derivation of the overall probabilities assigned to the SLIC particles.

The major problems encountered in this reconstruction had to do with overlapping energy depositions in the central region and the 'hadronic satellite' shower problem mentioned above. The hadronic satellite showers were handled not only by comparing measured and predicted shower shapes as described above, but also by comparing the location of the SLIC energy deposit with the energy deposit in the hadrometer from this track, and by throwing out small candidate sectors which were close to large energy depositions. The fractional energy resolution obtained for the SLIC was $\frac{21\%}{\sqrt{E}}$.

Details of these and other problems and details of the above fits are described elsewhere[36] .

Finally, the π^0s were reconstructed and the electron probabilities were calculated. The π^0s were 2γ combinations that gave the correct π^0 mass, had E_γ >2Gev, and that passed a (SLIC) product probability cut. The average reconstruction efficiency for π^0s in the charm decay $D^0 \rightarrow K^-\pi^+\pi^0$ was $\sim$ 15%. Electrons were defined using the following four criteria; (1) the ratio of SLIC energy to reconstructed track momentum, (2) the comparison of track position in the SLIC and in the track reconstruction, (3) the transverse width of the electron shower, and (4) the hadronic characteristics of the track. Electron probability cuts that were 80% efficient for the electron introduced $\sim$ 1% pion contamination.

5.2.2 The Cerenkov Reconstruction Program

The Cerenkov reconstruction program requires knowledge of the measured and of the predicted response of a track in the Cerenkov counters. The measured response of a *cell* is;

$$NMEAS_{cell} = NPH_k = (NADC_k - NPED_k)/NSPEP_k \qquad (5.2.1)$$

which is equation 3.5.3. In order to assign this value to a given track, we must be sure that this track is the only one throwing light on the cell's mirror. Assuming each track is a pion (since electron production is at the 2% level),[29] we propagate all charged tracks through the counters (including field effects in C1), throwing their Cerenkov light onto the mirror plane at the characteristic Cerenkov angle. Checking the mirrors near the impact

position in the mirror plane of a specific track, we can identify that set of M cells (M≤4) into which only this track throws light; denoting this set of mirrors as C(M). The measured response of these cells can then be uniquely assigned to this track;

$$N_{track,cell} = N_{j,k} = NMEAS_k; k \in C(M).$$

The predicted response of these cells is calculated as follows. Consider only the set of cells, C(M), into which this track throws Cerenkov light. The track throws only a fraction of its light onto a given cell's mirror; call it F^{geo}. In addition, the phototube response to a track near threshold is scaled down by the fraction (see section 3.5.3);

$$F^{mom} = (1 - (p_{th}/p)^2) \tag{5.2.2}$$

where the threshold momentum, p_{th}, is derived in the calibration. F^{geo} and F^{mom} are derived for each track, for each Cerenkov cell, and for all viable mass hypotheses (from the set; [e^-, μ, π,K, p] see section 3.5.1). Multiplying the gain (the maximum average response of a cell to a single track) by these fractions, we get the general expression for the predicted response of a cell to a given track with a given mass;

$$\overline{NPRED}_{mass,track,cell} = \overline{\mu}_{i,j,k} = F^{geo}_{i,j,k} \times F^{mom}_{i,j} \times GAIN_k. \tag{5.2.3}$$

The task now at hand is to generate probabilities for each track and each mass hypothesis, by comparing the predicted and measured responses

obtained above. We begin by summing the measured and predicted responses of all the cells ($\in$C(M)) which were uniquely assigned to the track in question;

$$N = N_j = \Sigma_k N_{j,k},$$

$$\mu = \mu_{i,j} = \Sigma_k \overline{\mu}_{i,j,k}$$

At the same time, we calculate the proper values for the width of the distribution function;

$$b = \overline{b}_{i,j} = \Sigma_k b_k \overline{\mu}^2_{i,j,k} / \overline{\mu}^2_{i,j}.$$

These were summed to provide adequate statistics for the compound Poisson distribution function (again, see section 3.5.3) which then gives the probabilities;

$$P_{i,j}(N, \mu, b) = \frac{\mu^N}{N!}(1 - b\mu)^{-N-1/b} \times \prod_{m=1}^{N-1}(1 + mb) \qquad (5.2.4)$$

The sum of these probabilities was normalized to 1 for each track, forming a set of consistency probabilities. Each of these probabilities measured, for a particular mass hypothesis, the likelihood that this track would generate the response actually measured in the Cerenkov counter. They were derived separately for each Cerenkov counter.

Using Bayes Theorem,[37] we combine the probabilities from both counters with the probability with which this particle type occurs in the data (the apriori probability = PROBAP$_i$)[38] ;

$$CVPROB_{i,j} = PROBC1_{i,j} \times PROBC2_{i,j} \times PROBAP_i \qquad (5.2.5)$$

and we have the final probabilities for all tracks and mass hypotheses. This procedure is used only on tracks for which we have Cerenkov information.

Tracks with no unshared mirrors or tracks that don't traverse the Cerenkov counters are simply assigned the apriori probabilities.

Figure 6.1.1 shows Λ^0(fig 6.1.1a,b) and K_s(fig 6.1.1e,f) mass plots before and after Cerenkov product probability cuts on their neutral decay products. For both neutral particles, it is clear that the Cerenkov cut drops the background by a factor of two without significantly affecting the signal.

5.2.3 The Vertexing Reconstruction

The vertexing reconstruction began with a global refit of all SMD tracks using only SMD hits. Information from D1 was used only to assign SMD hits to weak tracks, as this information didn't improve the vertexing. The procedure began by finding a 2 track vertex with χ^2 per degree of freedom(dof) < 3. Tracks are then added to this vertex, keeping only those for which the overall χ^2/dof remained under 3. The rejected tracks formed a new track set which was handled in the same manner as the initial track set. This procedure was followed until all tracks that could be assigned to a vertex were so assigned.

In practice, a similiar vertex set had to be reconstructed for every candidate secondary vertex. In the analysis, one first chooses the track combination of interest, calculates its vertex (the secondary vertex) and χ^2/dof, and then excludes these tracks from the main vertex track set. The vertex package (not including the global refit) is then run on the track subset to generate the candidate main vertices. Each secondary vertex selected in this manner is independent of the candidate main vertex set and, thus, a reliable measure of the separation of the main and secondary vertices can be made.

Errors on the vertices, including contributions from multiple scattering as well as from the vertex fit itself, are typically;

$$\sigma_x \simeq 13 + \frac{50}{p(Gev)}\mu m \tag{5.2.6}$$

$$\sigma_{dx/dz} \simeq 0.1 + \frac{3.3}{p(Gev)} mrad. \tag{5.2.7}$$

Figure 5.2.1 shows an exceptional event with two vertices associated with charm particle decays. The error ellipses shown represent $\sim 1\sigma$ errors.

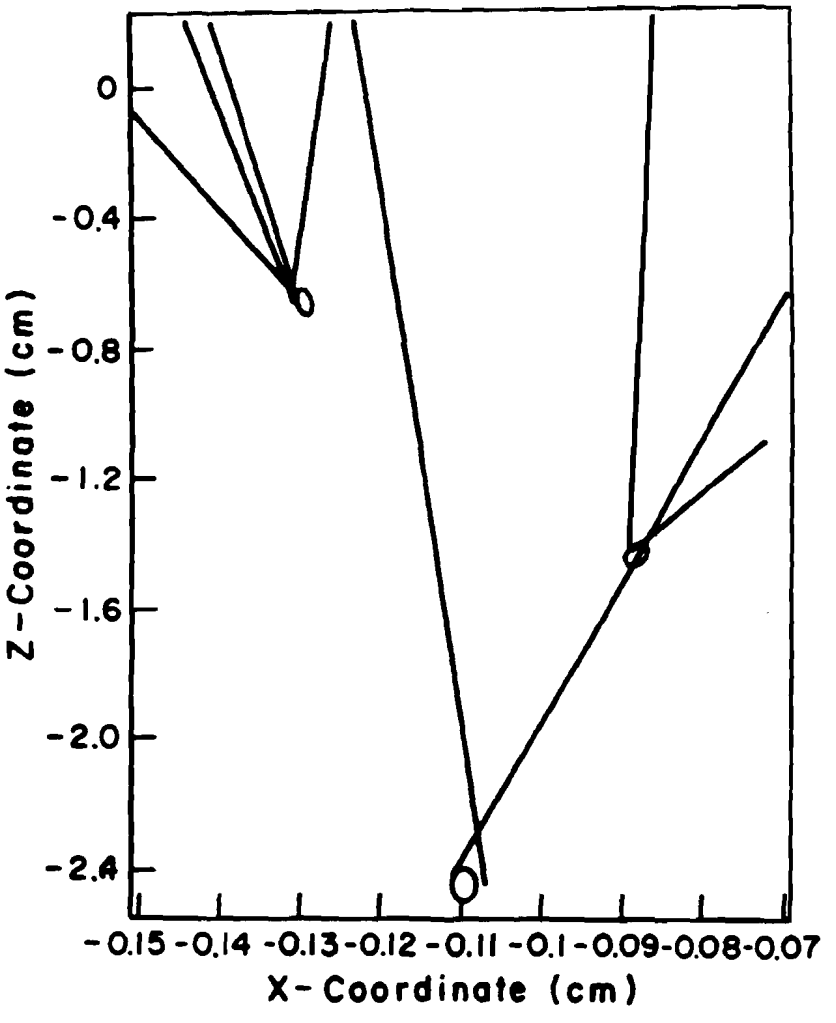

FIGURE 5.2.1. Charm event with two charm decays and main vertex reconstructed.

CHAPTER 6

THE ANALYSIS

A search through the full 10^8 event sample was made for decays of the four Λ_c^+ states; $\Lambda\pi$, $\Lambda\pi\pi\pi$, $p\overline{K_0}$, and $p\overline{K_0}\pi\pi$. The charge conjugates states are included for each of these decays. Theoretical predictions for the two-body modes ($\Lambda\pi$,$p\overline{K_0}$) exist which makes these modes particularly interesting.[11,13,15] The multi-body decay modes ($\Lambda\pi\pi\pi$,$p\overline{K_0}\pi\pi$) also engender interest because the branching fractions in these modes are not well known experimentally. The analysis of these modes involved first selecting the neutral particle data samples and then determining the appropriate event selection criteria separately for each mode. The vertex analysis of the two-body modes was especially challenging since a standard charm decay vertex could not be defined. In this chapter, the neutral particle strips and the charm decay mode substrips are discussed in detail as a prelude to the discussion of the final analysis cuts and the physics results in chapter 7.

6.1 The Neutral Particle Cuts

The initial step in the analysis was to select the neutral particle data samples ($\Lambda^0 \rightarrow p\pi$, $\overline{K_0} \rightarrow K_s \rightarrow \pi\pi$). Data samples are chosen, in general, using physically sensible event selection criteria. With the neutral particle decay samples, the track quality and Cerenkov behavior of the neutral decay products had to meet certain criteria as did the invariant mass and decay vertex formed from these two tracks. These criteria are presented below. The selection criteria, or 'cuts', chosen for the lambda (Λ^0) data sample

preserved about 3/4 of the reconstructed Λ^0 s (reconstruction efficiency $\sim$ .5) while reducing the background by almost a factor of 10. The cuts chosen for the K_s sample preserved 3/4 of the reconstructed signal (reconstruction efficiency $\sim$ .6) while reducing the background by a factor of 10 (see figure 6.1.1).

The Λ^0 cuts are outlined in Table 6.1.1 and described as follows. First, tracks detected in the SMDs ('SESTR' tracks) were excluded. The neutrals were thus formed using only 'ESTR' tracks; tracks detected only in the drift chamber system. This dramatically reduced the number of track combinations used to form Λ^0 candidates. The remaining tracks were then subjected to a general set of track quality cuts (which were applied to all tracks used in all the analyses, see Table 6.1.1A). The momentum fit performed on this track could have a χ^2 per degree of freedom (χ^2/DoF) of 5 or less, the momentum of the track had to be less than 250 GeV/c^2 as dictated by the electron beam energy, and all tracks had to penetrate at least the first magnet. This last cut was enforced by limiting the 'category' of the track (JCAT). To illustrate how track categories were determined, consider a track which was detected in all four drift chamber stations. The 4 bits associated with these 4 drift chamber stations in the reconstruction were all set 'on' and the track category was generated by summing the bits for this track; JCAT=1+2+4+8=15. A fifth bit was set if the track quality was poor. Restricting the track category between 3 and 15, as was standard practice in the analysis discussed below, was equivalent to requiring a good track that had been detected in at least the first two drift chamber stations, and therefore, had a well defined momentum, since these chambers straddle the first magnet.

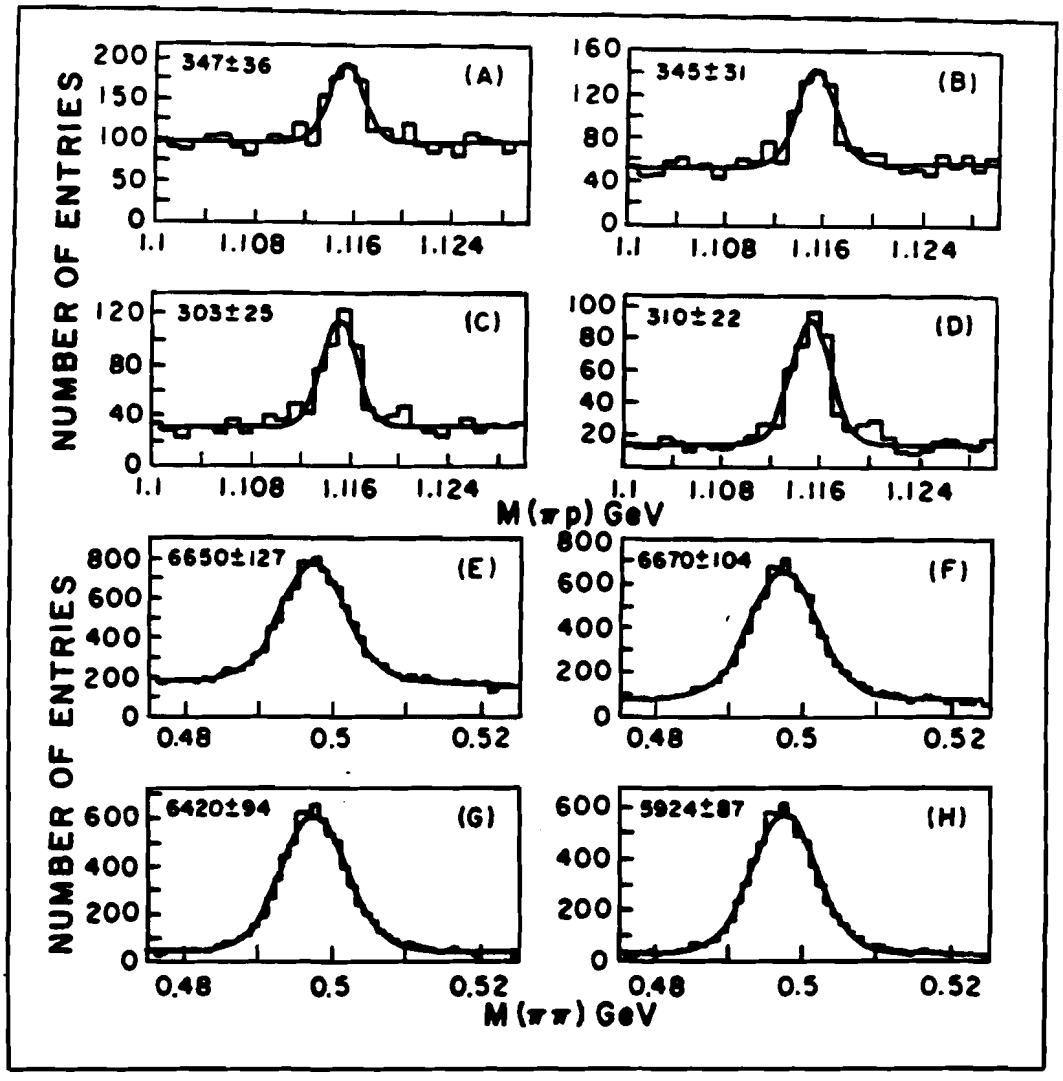

FIGURE 6.1.1. Plots (A-D) show the Λ^0 signal prior to any neutral particle vertex cuts (A), after Cerenkov cut (B), after vertex position cut (C), and after DCA cut(D). Plots (E-H) show the behavior of the K_{short} signal with the same cuts. The plots were fit to a gaussian plus a linear background where the width and mass of the signal is allowed to float.

Table 6.1.1A Standard Track Cuts

Cut	Value
χ^2	< 5.0
P	< 250 GeV/c^2
JCAT	$3 - 15$

Table 6.1.1B Neutral Particle Cuts

Standard Λ^0 Cuts	**Standard K_s Cuts**
Track Type ESTR	Track Type ESTR
$Q_{pr} \neq Q_{\pi}$	$Q_{\pi 1} \neq Q_{\pi 2}$
$\check{C}(pr) \times \check{C}(\pi) > 2.5\%$	$\check{C}(\pi 1) \times \check{C}(\pi 2) > 50\%$
M^0_Λ [1.11 - 1.121]GeV/c^2	M_{K_s} [.486 - .51]GeV/c^2
$Z_{vertex} > 0.$	$Z_{vertex} > 5.$
DCA $< 1.$	DCA $< .5$
$P_{pr} > P_{\pi}$	

For all Λ^0 candidates, the proton was chosen to be the track with the highest momentum. In addition, the Cerenkov probability formed from the product of the Cerenkov probabilities assigned to the Λ^0 decay products (the proton and pion) had to be > 2.5%. Very low ($P_{proton} < 5$ GeV/c^2) and very high momentum ($P_{proton} > 70$ GeV/c^2) Λ^0s whose proton and pion had been assigned the apriori Cerenkov probabilities were accepted with this cut. Furthermore, the proton had to penetrate both magnets (JCAT $\geq$ 5), the distance of closest approach (DCA) of the proton and the pion tracks had to be less than 1cm, and the z position of the Λ^0 decay (which is the z position at which the DCA occurs) had to be greater than 0, where z=0 is the downstream end of the target. The z position cut eliminated background from ESTR tracks that originate at the production vertex. Finally, the Λ^0 mass was constrained to be between 1.110 and 1.121 GeV/c^2 . The set of Λ^0 candidates defined by these cuts was the same for both the $\Lambda\pi$ and $\Lambda\pi\pi\pi$ analyses.

The Kshort (K_s) cuts are also outlined in Table 6.1.1. Again, the decay products of the neutral particle had to pass the standard track quality cuts while the product of their pion Cerenkov probabilities had to exceed 50%. Tracks detected in the SMD's were excluded from the analysis. The K_s decay vertex had to be > 5cm from the end of the target and the DCA of the two pions had to be < .5cm. Finally, the K_s mass was constrained to be between .486 and .51 GeV/c^2 .[39] This set of cuts remained unchanged throughout the $p\overline{K_0}$ and $p\overline{K_0}\pi\pi$ analyses. The subset of data events which had combinations that passed the Λ^0 or K_s cuts were (separately) stripped from the full data sample in order to make analysis of charm decay modes containing these neutrals more convenient.

6.2 The Substrips

Although each of these neutral particle event subsets was only a small fraction of the full set of 10^8 events, they were still very large (Λ^0 strip: $>$ 3 million events; K_s strip: $>$ 5 million events). Clearly, they had to be reduced in size so the analyses planned for the charm decay modes containing these neutrals could be done in a reasonable time. Therefore, a 'substrip' was performed on each neutral particle strip for each mode being analyzed, with cuts that depended on that mode. The set of cuts used for the substrips of each of the four Λ_c^+ modes mentioned in the introduction will now be discussed.

A computer program was written that could substrip the Λ^0 strip for both the $\Lambda\pi\pi\pi$ and the $\Lambda\pi$ decay modes. The list of cuts for these modes is given in Table 6.2.1. The goal when substripping a data sample is to achieve sufficient reduction in the size of the sample, while using the smallest number of cuts possible, and without reducing the charm particle 'efficiency'. The efficiency is the fraction of charm particle decays of a given mode that survive all the cuts associated with that mode. It is determined by simulating the response of the spectrometer to the charm particle decay using a Monte Carlo computer program (see section 6.4). These simulated raw data events are then run through the reconstruction and analysis programs just like true raw data events to estimate the effect of the chosen cuts on the charm signal in question.

Cuts that don't affect the efficiency are, naturally, the first cuts we apply to any substrip. For the $\Lambda\pi$ mode, the Λ^0 strip was reduced from 3 million to .5 million events by requiring that the event have at least one $\Lambda\pi$ combination with a mass between 2 and 2.5 GeV/c^2 , and by requiring that

Table 6.2.1A Substrip Cuts: $\Lambda\pi\pi\pi$

$\Lambda\pi\pi\pi$ **Substrip**	$\Lambda\pi\pi\pi$ **Analysis Strip**	ϵ
$\text{Type}_{\pi\pi\pi}$ SESTR	$\text{Type}_{\pi\pi\pi}$ SESTR	.16
$Q_{\pi 1}+ Q_{\pi 2}+ Q_{\pi 3} = Q_{pr_\Lambda}$	$Q_{\pi 1}+ Q_{\pi 2}+Q_{\pi 3} = Q_{pr_\Lambda}$	.145
$M_{\Lambda_c^+}$ [2 - 2.5]GeV/c^2	$M_{\Lambda_c^+}$ [2 - 2.5]GeV/c^2	.145
	$\check{C}_{3\pi} > .25$	.13
	1 JCAT 3 Track Only	.115
	$\chi^2_{sec} < 10$	.078
	DIP $< 150\mu$	.065
	SDZ > 4	.035
	RAT < 1	.019

Table 6.2.1B Substrip Cuts: $p\overline{K_0}\pi\pi$

$p\overline{K_0}\pi\pi$ **Substrip**	$p\overline{K_0}\pi\pi$ **Analysis Strip**	ϵ
$\text{Type}_{p\pi\pi}$ SESTR	$\text{Type}_{p\pi\pi}$ SESTR	.21
$Q_{\pi 1} = -Q_{\pi 2}$	$Q_{\pi 1} = -Q_{\pi 2}$	.19
$M_{\Lambda_c^+}$ [2 - 2.5]GeV/c^2	$M_{\Lambda_c^+}$ [2 - 2.5]GeV/c^2	.19
$\check{C}_{pr} \times \check{C}_{\pi 1} \times \check{C}_{\pi 2} > 10\%$	$\check{C}_{pr} \times \check{C}_{\pi 1} \times \check{C}_{\pi 2} > 20\%$	.09
	1 JCAT 3 Track Only	.08
	$\chi^2_{sec} < 10$	.05
	DIP $< 150\mu$	.043
	SDZ > 4	.026
	RAT < 2	.02

Table 6.2.1C Substrip Cuts: $p\overline{K_0}$

$p\overline{K_0}$ Substrip	$p\overline{K_0}$ Analysis Strip	ϵ
$Type_{pr}$ SESTR	$Type_{pr}$ SESTR	.24
$M_{\Lambda_c^+}$ [2 - 2.5]GeV/c^2	$M_{\Lambda_c^+}$ [2.1 - 2.5]GeV/c^2	.24
$\check{C}_{pr} > 20\%$	$\check{C}_{pr} > 30\%$	.14
	$JCAT_{pr} \geq 5$	.14
	$ITP_{pr} > 0$	.075

Table 6.2.1D Substrip Cuts: $\Lambda\pi$

$\Lambda\pi$ Substrip	$\Lambda\pi$ Analysis Strip	ϵ
$Type_\pi$ SESTR	$Type_\pi$ SESTR	.20
$Q_\pi = Q_{pr_\Lambda}$	$Q_\pi = Q_{pr_\Lambda}$	.20
$M_{\Lambda_c^+}$ [2 - 2.5]GeV/c^2	$M_{\Lambda_c^+}$ [2. - 2.4]GeV/c^2	.20
	$\check{C}_\pi > 70\%$	.19
	$\lvert\cos_{cm}(\theta)_\pi\rvert < .7$	.14
	$ITP_\pi > 0$	.075

the added pion have the correct charge (Q_π=Q_{pr}), be found in the SMDs, and pass the standard good track cuts. Note that none of these cuts affect the $\Lambda_c^+ \rightarrow \Lambda\pi$ efficiency noticeably. (Efficiency($\Lambda\pi$)$\sim$ 20% after these cuts; we lose 80% of the charm to the Λ^0 and $\Lambda^0\pi^+$ substrip cuts and to fundamental causes such as track acceptance $\epsilon(\Lambda\pi \sim .87)$ and reconstruction $\epsilon(\Lambda\pi \sim .50)$) The substrip cuts for the $\Lambda\pi\pi\pi$ mode were essentially the same as the $\Lambda\pi$ substrip cuts except, in this case, $Q_{\pi 1}+Q_{\pi 2}+Q_{\pi 3}=Q_{pr}$. The $\Lambda\pi\pi\pi$ substrip threw out 2/3 of the Λ^0 strip (leaving 1 million events) with an efficiency of 10%.

The K_s strip was substripped simultaneously for the $p\overline{K^0}$ and $p\overline{K^0}\pi\pi$ charm decay modes. Again, the emphasis of this substrip was to remove background from the data sample with minimal reduction of charm efficiency. The track quality and charge cuts and the charm mass cuts were applied first as in the $\Lambda\pi/\Lambda\pi\pi\pi$ substrip (see Table 6.2.1). Even after these cuts, however, the data subsamples for the $p\overline{K^0}/p\overline{K^0}\pi\pi$ modes were too large. Having exhausted all the efficiency independent cuts for these two modes, we were led to apply a hard Cerenkov cut on the proton probability. This cut did reduce the efficiency but did not affect the analyses of these modes.

As can be seen in figure 6.2.1, the hard proton Cerenkov cut that was applied to the $p\overline{K^0}$ substrip ($\check{C} > 20\%$) eliminated most of the background events in this file by excluding candidate protons which the Cerenkov counters could not separate from pions (apriori proton candidates; $P_{pr} < 5$ GeV/c^2 , or > 70 GeV/c^2). The efficiency of this substrip was also reduced, by a factor of $\sim 1/3$, but this is acceptable given the reduction in the background we obtain with this cut. On the bottom line, the 5 million K_s strip events were reduced to $\sim$ .3 million events while 20% of the charm signal was

preserved in the $p\overline{K^0}$ substrip. The $p\overline{K_0}\pi\pi$ mode was handled in like manner except, in this case, a product Cerenkov cut was applied, with $\check{C}_{p\pi\pi} > 10\%$. This cut had essentially the same effect on the proton as the Cerenkov cut discussed above and, in addition, low Cerenkov probability pions were rejected as candidate charm decay tracks. The substrip for the $p\overline{K^0}\pi\pi$ mode reduced the K_s data sample by a factor of 5 with an efficiency of 11%.

At this point, we had obtained substrip data files for each of the 4 modes of interest. These data files provided a convenient event sample, containing the bulk of the reconstructable charm signal in each mode, from which analysable data files could be stripped.

6.3 The Analysis Files

The final stripping programs were run on the substripped data at this point to generate the (sub-substrip) data files for each mode on which data analyses could be performed efficiently. All the cuts which were available for use on these modes were applied at this last stripping level since we had to reduce the hundreds of thousands of substrip events down to the level of a few thousand events. These cuts are described below.

The vertexing cuts, which were used whenever a standard secondary vertex could be defined (i.e. $\Lambda\pi\pi\pi$, $p\overline{K_0}\pi\pi$ decay modes), included the DIP cut, the SDZ cut, the χ^2_{sec}/DoF cut, and the RAT cut. The χ^2_{sec}/DoF cut variable was the χ^2/DoF assigned to the secondary vertex by the least-squares vertex fit (the fit procedure is discussed in section 5.2.3). Recall that the vertices generated by the reconstruction program had to have χ^2/DoF < 3. Similiar values for the χ^2_{sec}/DoF of the secondary vertex were required in the analysis.

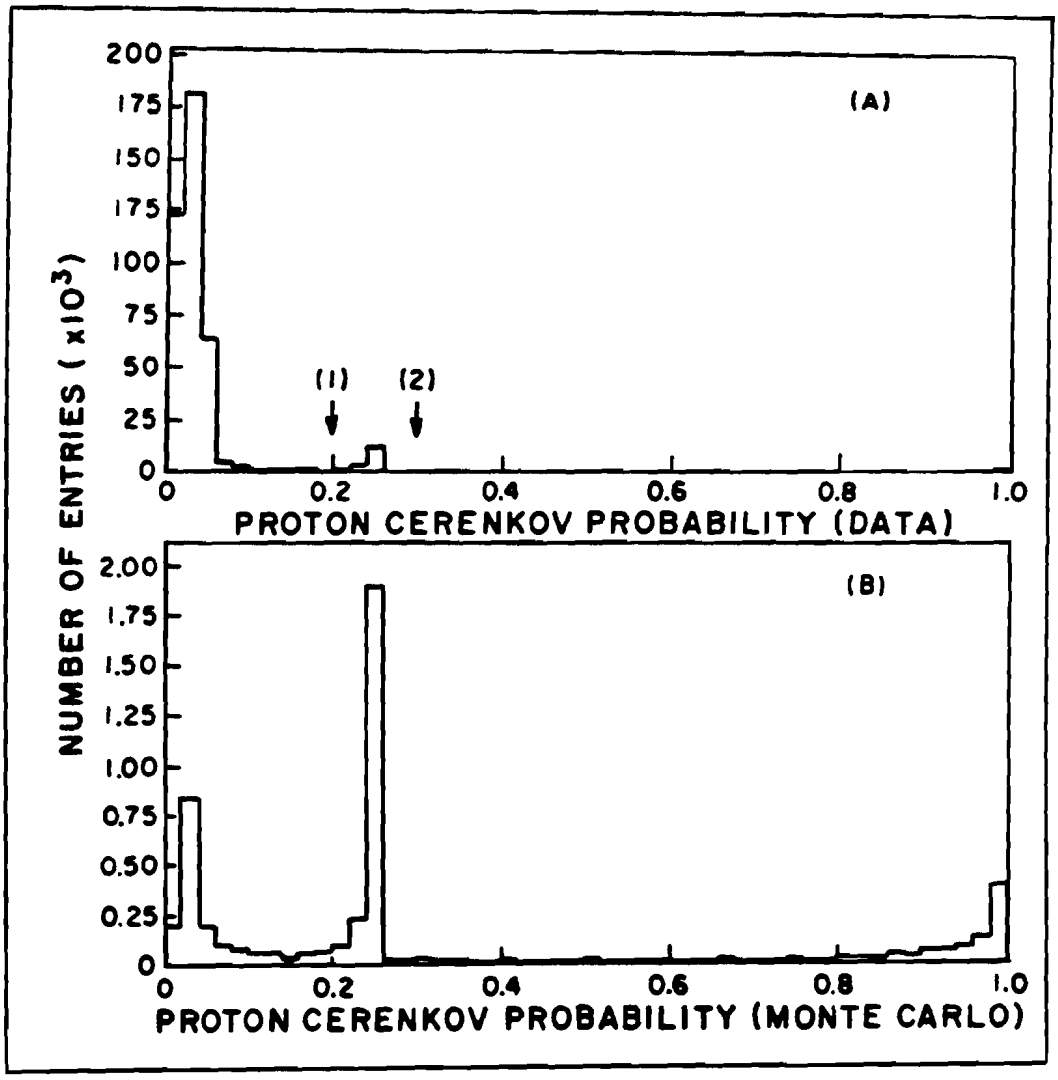

FIGURE 6.2.1. Plot A displays the proton Cerenkov probability for a sample of unbiased data events. Plot B shows the same probability for Monte Carlo protons from the charm decay $\Lambda_c^+ \rightarrow p\overline{K_0}$. The values chosen for the proton Cerenkov cut in the $p\overline{K_0}$ substrip (1) and analysis strip (2) are shown in plot A. The three peaks in plot B represent p/K/π ambiguous, p/K ambiguous, and p definite candidates respectively.

The DIP cut variable was derived in three steps. First, the charm particle momentum was constructed from the charm particle decay products. This vector was then forced to pass through the secondary vertex. Finally, the distance of closest approach between the constrained charm momentum vector and the main vertex was calculated (in the x-y plane perpendicular to the beam and containing the main vertex). This is the Distance In the Plane or DIP cut variable. This distance is zero for an ideal charm particle decay since, in this case, the momentum vector of the charm particle connects the main and secondary vertices.

The SDZ cut variable measured the significance of a given secondary vertex with respect to the main vertex chosen in the analysis. It takes the form,

$$\mathrm{SDZ}=\Delta z/\sigma_z$$

where Δz is the separation between the main and secondary vertices and σ_z is the combination, in quadrature, of the errors in z assigned to the two vertices. The secondary vertex and the candidate main vertex set were derived as described in section 5.2.3. The main vertex chosen in the analysis was the main vertex from this set associated with the smallest DIP.

The RAT cut variable for a given secondary vertex track was calculated by finding the distance of closest approach between the main vertex and this track (DCA_{main}) and between the secondary vertex and this same track (DCA_{sec}) and taking the ratio of $\mathrm{DCA}_{sec}/\mathrm{DCA}_{main}$. This ratio was derived for all secondary vertex tracks and each such ratio was restricted to be within the limit chosen for the particular charm decay mode being analysed. A typical limit of RAT < 1 would select secondary vertex candidates whose tracks were closer to their secondary vertex than to the chosen main vertex,

which is usually the case for tracks associated with a charm particle decay. This cut was effective in eliminating secondary vertex candidates where one (or more) of the tracks associated with this vertex actually came from the main vertex. We could not observe the $\Lambda\pi\pi\pi$ charm signal without this cut.

The cuts chosen to define the analysis data file for the $\Lambda\pi\pi\pi$ mode are given in Table 6.2.1A. They were applied tightly (i.e. close to the optimum value chosen in the final analysis) to achieve sufficient data sample size reduction and this restricted our ability to study the cuts with this file. Even with these tight cuts, however, the analysis data file was large; $>$ 30K events with an efficiency of $\sim$ 2%.

The analysis data file for the $p\overline{K_0}\pi\pi$ decay mode is defined with a set of vertex cuts similiar to those used for the $\Lambda\pi\pi\pi$ mode as can be seen in Table 6.2.1B. The Cerenkov product probability cut, $\check{C}_{p\pi\pi}$, is tightened as well. The combined effect of the vertex and Cerenkov cuts reduced this data file to a reasonable size; $<$ 10K events with an efficiency of $\sim$ 2%.

The substrip data sample for the $\Lambda\pi$ mode was not significantly smaller than the $\Lambda\pi\pi\pi$ sample. Therefore, as in the last case, all the available cuts had to be applied and applied tightly. These cuts were, however, substantially different from the previous set of cuts because, as mentioned in the introduction, we were not able to form a standard secondary vertex with the decay products of this mode. The charm decay modes of this type, with one neutral particle and one SESTR track, form a sub-class of modes; the two-body modes. The basic analysis discussed below is the same for both the $p\overline{K_0}$ and $\Lambda\pi$ decay modes.

The initial thrust of the two-body analysis was to determine the set of cuts that made the best use of the information available in these

modes. We have three tracks with well defined momentum (ESTR track momenta errors are comparable to SESTR track momenta errors since the momenta is determined largely by the drift chamber tracking (see section 3.3)) one of which, the SESTR track, has a well defined position. To begin the analysis, we calculate the vector distance from the SESTR track to a given main vertex candidate in the plane perpendicular to the beam direction and containing the candidate vertex; call this $\overrightarrow{DMISS}$ (see figure 6.3.1). We then break $\overrightarrow{DMISS}$ into components, one of which is contained in the plane defined by the decay products of the charm particle. The remaining component is approximately equal to the distance of closest approach of the main vertex candidate and the charm decay plane (see below). These distances are henceforth labeled In The decay Plane (ITP) and Out of The decay Plane (OTP) distances respectively. The main vertex chosen in this analysis is the candidate vertex associated with the smallest OTP distance.

The procedure used to find these values is as follows (figure 6.3.1). We define a unit vector normal to the charm decay plane by taking the cross product of the charm decay products; the SESTR track momentum with the momentum of the neutral. This unit vector is approximately parallel to the laboratory X-Y plane. Rotating the laboratory X axis counterclockwise[40] into this unit vector, we can define a new coordinate system with the unit vectors $\hat{x}'_1$ and $\hat{y}'_1$. Expressing $\overrightarrow{DMISS}$ in this new coordinate system, we see that $\overrightarrow{DMISS} \bullet \hat{x}'_1$ is the Out of The decay Plane distance (OTP) and $\overrightarrow{DMISS} \bullet \hat{y}'_1$ is the In The decay Plane distance (ITP).

We can also investigate the behavior of the secondary vertex for these decays. Having chosen the main vertex as described above, we can pin the charm momentum vector to this vertex and calculate the distance of closest

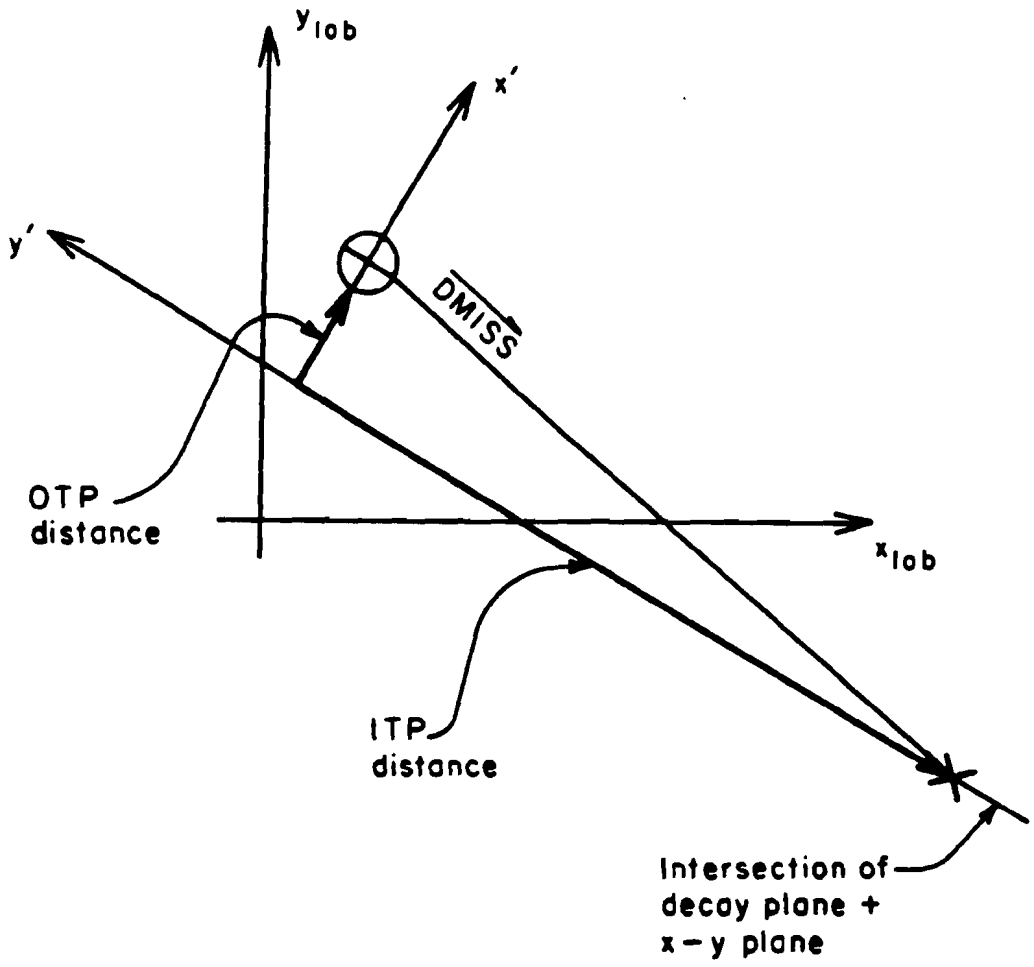

FIGURE 6.3.1. The two-body cut parameters. The x_{lab}-y_{lab} plane is perpendicular to the beam (which is pointing out of the paper) and contains the main vertex candidate, $\otimes$. The $\overrightarrow{DMISS}$ vector connects this vertex to the point of intersection of the SESTR track and the x-y plane, $\times$. The intersection of the charm decay plane and the x_{lab}-y_{lab} plane defines the y' axis. The decomposition of this vector is handled as shown.

approach of the SESTR track and the now well defined charm momentum direction. As mentioned earlier, this DCA is essentially equivalent to the OTP distance.* While deriving the DCA with this procedure, we also obtain the decay distance Δz, which is used in turn to define a two-body value for the SDZ. The error on the secondary vertex, which is the only unknown commodity, is given by the ratio of a constant divided by the angle between the two charm decay products in the laboratory (i.e. the opening angle). The value of the constant is chosen such that this error effectively accounts for the measured secondary vertex position error (see figure 6.3.2). The remaining vertex cut used in the two-body analysis requires that the ITP distance be greater than the OTP distance at all times.

Finally, we can apply a cut on (the cosine of) the angle the SESTR track makes with the charm particle momentum in the charm particle's center of mass, defined as $\cos_{cm}(\theta)$. Figure 6.3.3 illustrates the behavior of this variable for Monte Carlo charm events and data background events. This is clearly an effective cut variable. The strength of this cut in the $\Lambda\pi$ mode comes from the fact that the charm decay products are distributed isotropically in the center of mass of the charm while, in the background events, hard forward pions ($\cos\theta = 1$) are needed to combine with the Λ^0 to form the large Λ_c^+ mass. This cut is important for both two-body modes.

Altogether, then, we have four two-body vertex cuts and the $\cos_{cm}(\theta)$ cut. The most important vertex cut for the $\Lambda\pi$ analysis was the SDZ cut while the three other cuts, the RAT (OTP/ITP) cut, the DCA cut, and

---

* The charm momentum vector is parallel to the charm decay plane and so the minimum distance between this vector and the SESTR track is equivalent to the perpendicular distance from the decay plane to the main vertex. The OTP vector is constrained to the X-Y plane (since $\overrightarrow{DMISS}$ is) and is in general slightly larger in size than the DCA, but negligibly so.

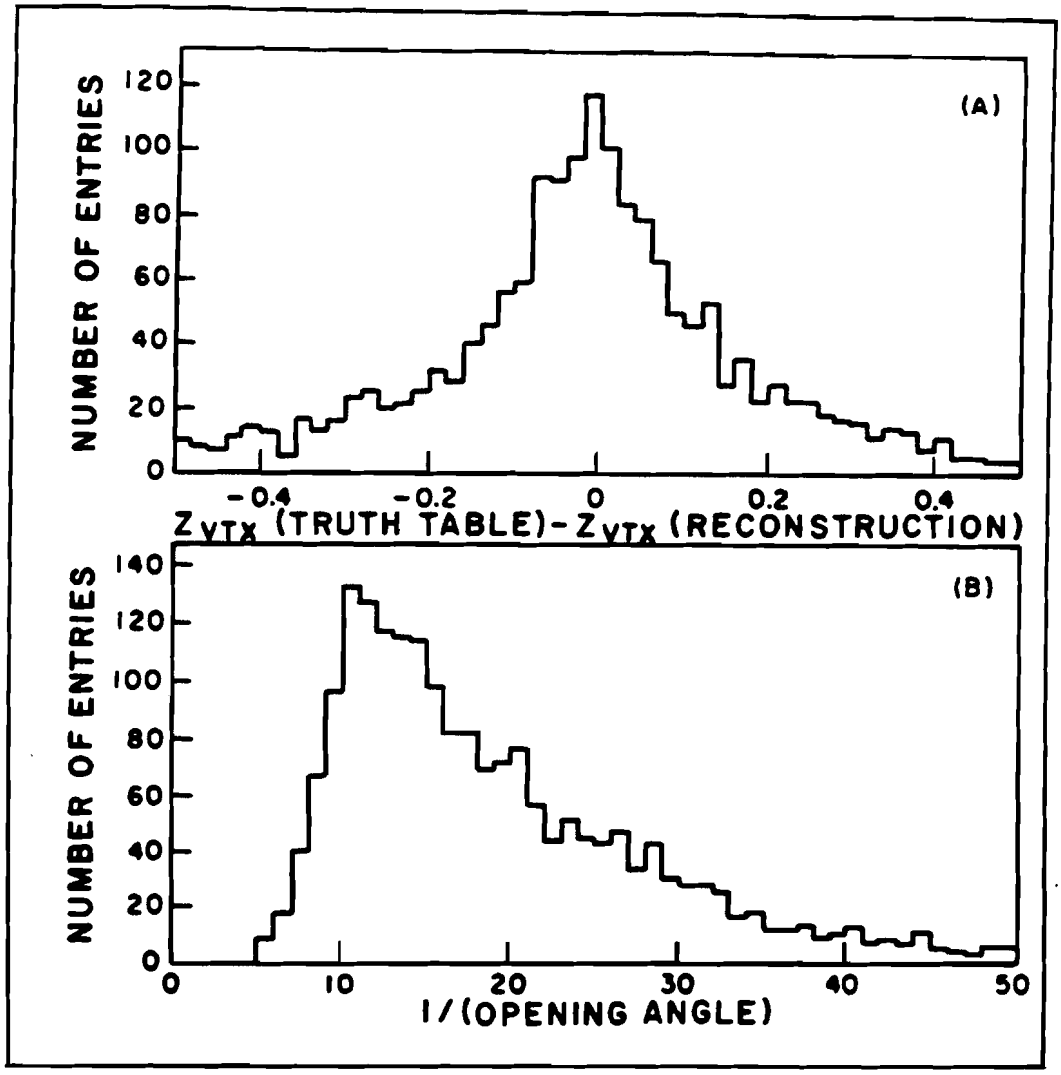

FIGURE 6.3.2. These plots were obtained from the two-body analysis of the $\Lambda_c^+ \rightarrow \Lambda\pi$ decay mode. The difference between the true secondary vertex position and the decay position obtained from the two-body analysis is plotted in (A), with $\sigma \sim 700\mu$. Plot (B) displays the parameter (1/opening angle) which has a mean of $\sim$ 20. A secondary error of $\sim$ .003/(opening angle) (=.003 $\times$ 20. = 600μ on average) is appropriate in this case.

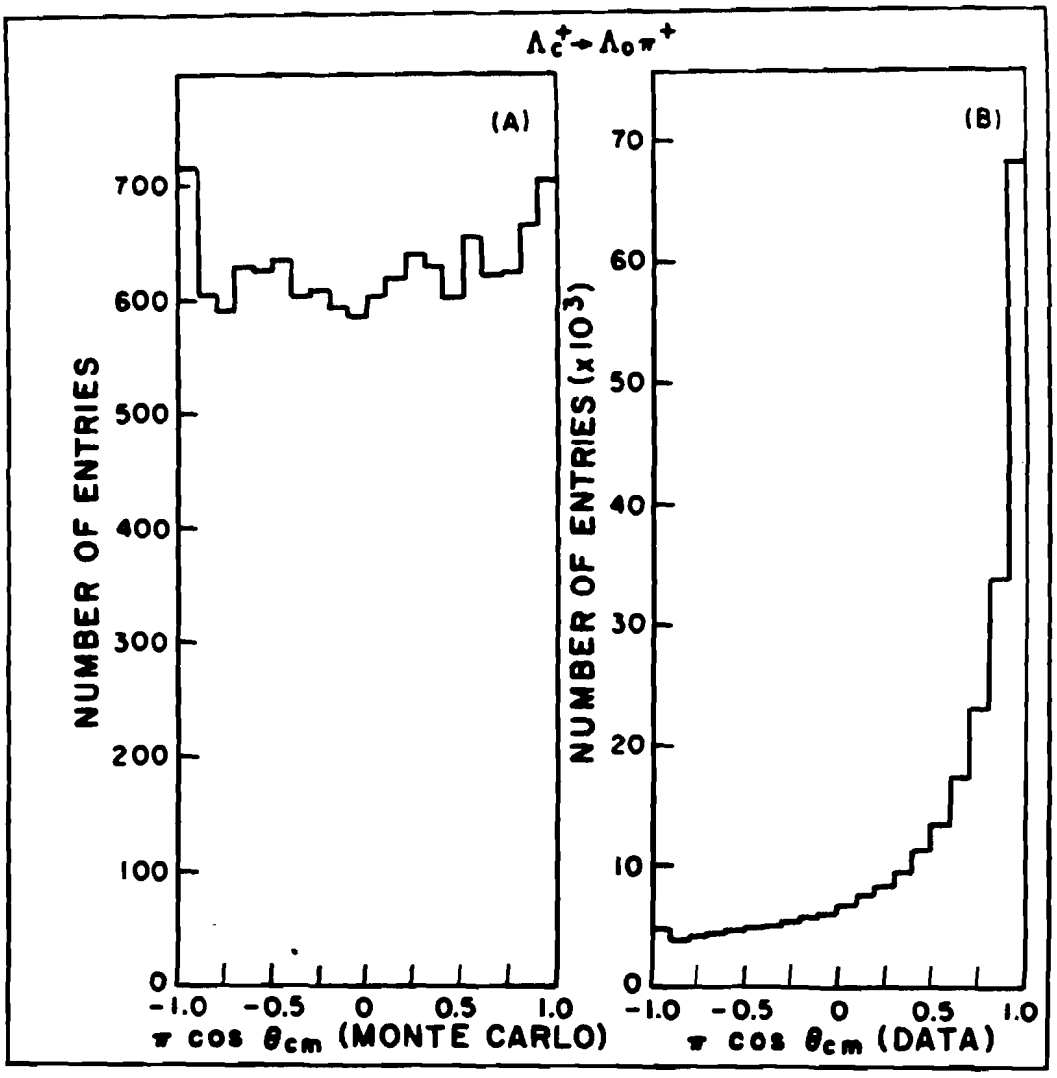

FIGURE 6.3.3. $\Lambda_c^+ \to \Lambda\pi$ decay: (A) shows the angle made by the pion in the center of mass of the Λ_c^+ for Monte Carlo events. (B) shows this angle for background events. A cut at $\cos\theta_{cm} < .6$ was chosen in this case.

the ITP cut were used as background rejection cuts (i.e. they have only a small impact on charm efficiency, see the efficiency tables in chapter 7). For the $p\overline{K^0}$ mode, the proton carried the bulk of the Λ_c^+ momentum and thus degraded the secondary vertex definition. As a result, the ITP cut was the most important cut for this mode.

The analysis data file for the $\Lambda\pi$ mode was created by requiring that ITP > 0 and $|\cos_{cm}(\theta)_\pi| < .7$, and by requiring that the SESTR pion have JCAT ≥ 5 (see Table 6.2.1). Again, the cuts had to be applied tightly to obtain a file of reasonable size (< 10 K events with an efficiency of 7.5%). The $\Lambda_c^+ \rightarrow p\overline{K_0}$ data file was stripped with similiar cuts as can be seen in this table, and, in addition, the proton Cerenkov cut was tightened. This cut was chosen such that only definitely identified protons are accepted (see figure 6.2.1). The efficiency measured for this strip is $\sim 7.5\%$ and the strip file contains < 10 K events, the same values obtained for the $\Lambda\pi$ analysis strip.

6.4 Monte Carlo Studies

The function of the Monte Carlo is to account for the inability of the spectrometer to detect all of the signal particles produced in the experiment. Typically, the spectrometer can fully reconstruct only a few percent of the charm decays produced in the photon interactions. By accounting for this inefficiency, we can generate the *efficiency corrected* charm signal ($= N/\epsilon$ where N = the detected charm signal, and ϵ = efficiency) which is a measure of the amount of charm produced in this decay mode during the experiment. In this thesis, we measure the relative branching fractions of the $p\overline{K_0}$, $\Lambda\pi$, $\Lambda\pi\pi\pi$, and $p\overline{K_0}\pi\pi$ decay modes with respect to the more significant $pK\pi$

decay mode by taking the ratio of efficiency corrected charm signals. This expression takes the form;

$$RBF = \frac{\frac{N}{\epsilon}(p\overline{K_0})}{\frac{N}{\epsilon}(pK\pi)}$$

for the $p\overline{K_0}$ mode, where RBF $\equiv$ the relative branching fraction. By taking the ratio of these numbers, we obtain a physically pertinent result which is independent not only of the spectrometer but of the beam and the charm production characteristics as well. Systematic problems common to both modes also tend to cancel. At this juncture, therefore, we need only worry about how well the Monte Carlo accounts for the differences between the four modes being studied and the pKπ mode.

The Monte Carlo charm events were generated using the photon gluon fusion model (section 1.3) and the subsequent gluon and quark fragments were hadronized using the Lund fragmentation Monte Carlo.[61] These hadrons were propagated through a computer simulation of our spectrometer where the geometrical acceptance, the resolution, and the intrinsic efficiencies of the various component detectors were taken into account. In particular, the Monte Carlo tracking efficiencies were set by measuring the efficiency of each individual microstrip and drift chamber plane to fitted tracks from data charm meson decays with 2, 3, and 4 decay products (D $\rightarrow$ Kπ, K$\pi\pi$, and K$\pi\pi\pi$). The Monte Carlo tracking efficiencies were set to within 1% of the values derived from this data (for example, $\overline{\epsilon_{SMD}}$(plane1)= 88 $\pm$ 1.5% : $\overline{\epsilon_{DC}}$(D1AU)= 93$\pm$.6%). The other free parameters in the Monte Carlo, such as Cerenkov response, were set in a similiar manner and to similiar accuracy as discussed elsewhere.[26] The Monte Carlo was thus 'tuned' to mimic the

data for charm decay modes similiar to those from which these free parameters were obtained ($\Lambda_c^+ \rightarrow pK^-\pi^+$ for instance). The modes discussed in this thesis diverge sharply in character from these large statistical samples of charmed mesons. The presence of a neutral particle in each of these modes was the most distinct difference, although the behavior of the Monte Carlo with respect to the Cerenkov cuts and the modified two-body vertex cuts had to be investigated as well.

The proton Cerenkov cut[42] was the first cut tested. This was done by defining clean Λ^0 data and Monte Carlo samples with cuts similiar to the Λ^0 cuts discussed above, excluding the Cerenkov cut. The Cerenkov cuts were then applied to both samples and, using the pre-Cerenkov Λ^0 signal to normalize the results, we obtained well defined efficiencies for these cuts for both the Monte Carlo and data signals. In this manner, it was determined that the data was 10% more efficient than the Monte Carlo for the proton Cerenkov cut used on the $pK\pi$ mode. The values for the $\Lambda\pi$ and $\Lambda\pi\pi\pi$ relative branching fractions derived in this thesis thus had to be increased by $\sim$ 10% to account for this difference in efficiencies. The proton Cerenkov cut applied to the $p\overline{K^0}$ and $p\overline{K^0}\pi\pi$ decays was the same as that applied to the $pK\pi$ mode and thus no correction was applied to these measurements.

A similiar study of the kaon Cerenkov efficiency using the large charm meson samples[43] showed that a kaon Cerenkov cut that excluded apriori pions was $\sim$ 30% less efficient in the Monte Carlo than in the data for kaons of $> 40 GeV/c^2$ momentum. This problem is closely related to the problem with the proton Cerenkov cut, as definite Cerenkov identification of protons begins at 40 GeV/c^2 . Less than 10% of the kaons in the $pK\pi$ signal have momentum this high and, therefore, this systematic problem is

of little concern in the analyses discussed here. These two studies outline the basic technique used to test the Monte Carlo simulation of data. Clean data and Monte Carlo samples are first isolated without the use of the cut to be tested. The efficiency of the cut is then derived separately for the data and the Monte Carlo and these are compared.

We continue our study of the Monte Carlo with a look at the standard vertex cuts. Consider figure 6.4.1. The histograms on the left of this figure show the attenuation of the Monte Carlo signal with respect to the SDZ, RAT,and DIP cuts for the decay mode $D^* \rightarrow D_0\pi \rightarrow \pi K\pi$ (this was one of the modes used to develope the Monte Carlo). The plots on the right of this figure show the efficiency corrected data signal for this decay ($\frac{N_{data}}{\epsilon}$) with respect to these cuts. This study is possible because we were able to obtain a data signal in this decay mode without the use of any of the vertex cuts. We could therefore compare the pre-cut efficiency corrected signal (the first entry in each plot) to the efficiency corrected signal obtained with the various vertex cuts. It is clear from this figure that the efficiency corrected charm signal is stable to within 10% for all cuts. We can assume, then, that the Monte Carlo is sufficiently stable with respect to these cuts for our study of the $\Lambda\pi\pi\pi$ and $p\overline{K_0}\pi\pi$ decay modes since the statistical errors in these modes are $> 25\%$.

A similiar study of the two-body cuts was then performed using the same $D_0 \rightarrow K\pi$ signal (figures 6.4.2, 6.4.3). First, the kaon (the heavy particle) was excluded from the vertexing so that this decay would imitate the $\Lambda_c^+ \rightarrow \Lambda\pi$ decays. The two-body analysis was then performed with the kaon assuming the role of the Λ^0 and the pion the role of the pion. The plots on the right side of figure 6.4.2 show the behavior of the efficiency corrected

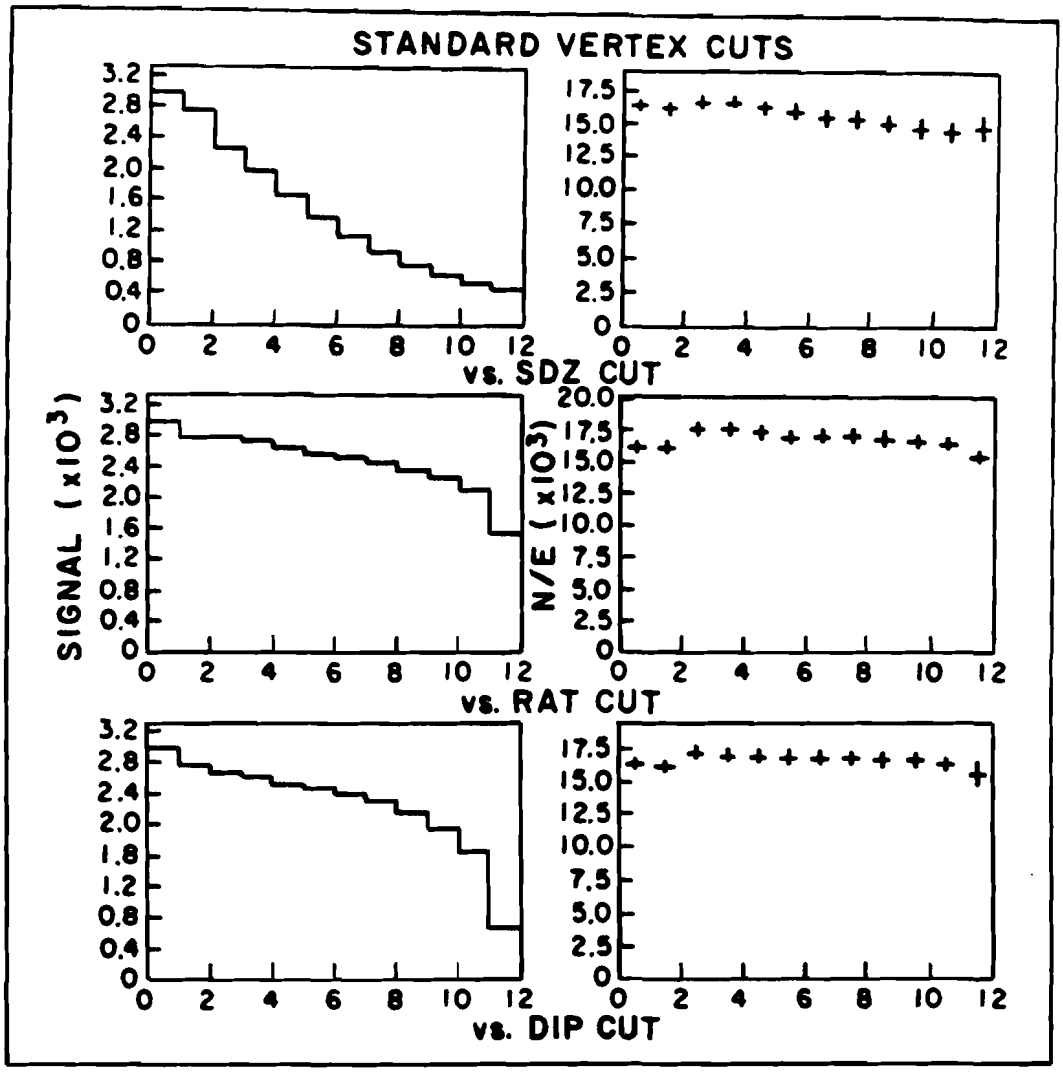

FIGURE 6.4.1. The behaviour of the charm signal $D^0 \rightarrow K^-\pi^+$ with the standard vertex cuts. The attenuation of the signal with the cut is shown on the left, the corresponding efficiency corrected signal is shown on the right. Table 6.4.1 contains the 12 cuts employed for these 3 cut parameters.

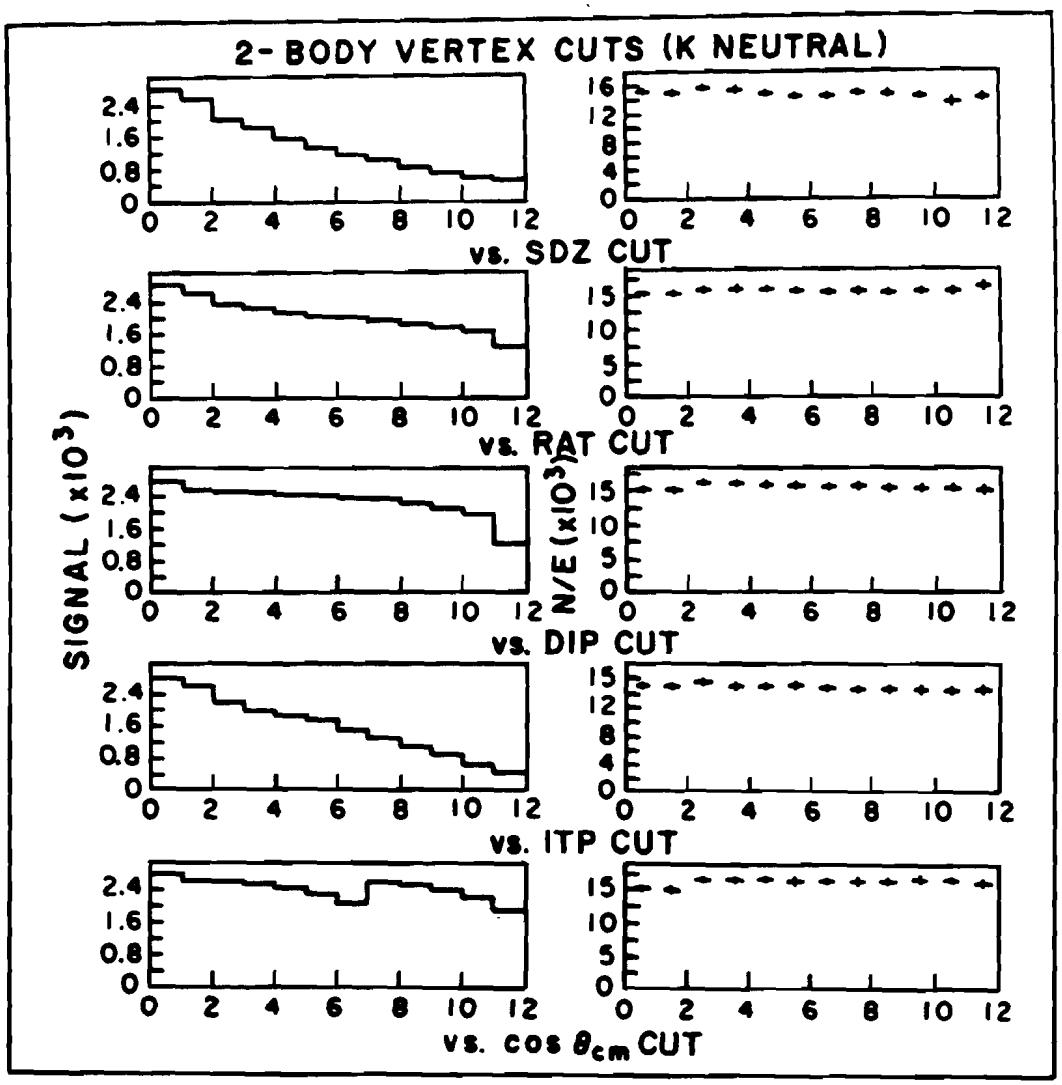

FIGURE 6.4.2. The behaviour of the charm signal $D^0 \rightarrow K^- \pi^+$ with modified 2-body vertex cuts and the kaon excluded from the vertexing. The attenuation of the signal with the cut is shown on the left, the corresponding efficiency corrected signal is shown on the right. Table 6.4.1 contains the 12 cuts employed for each of these 5 cut parameters.

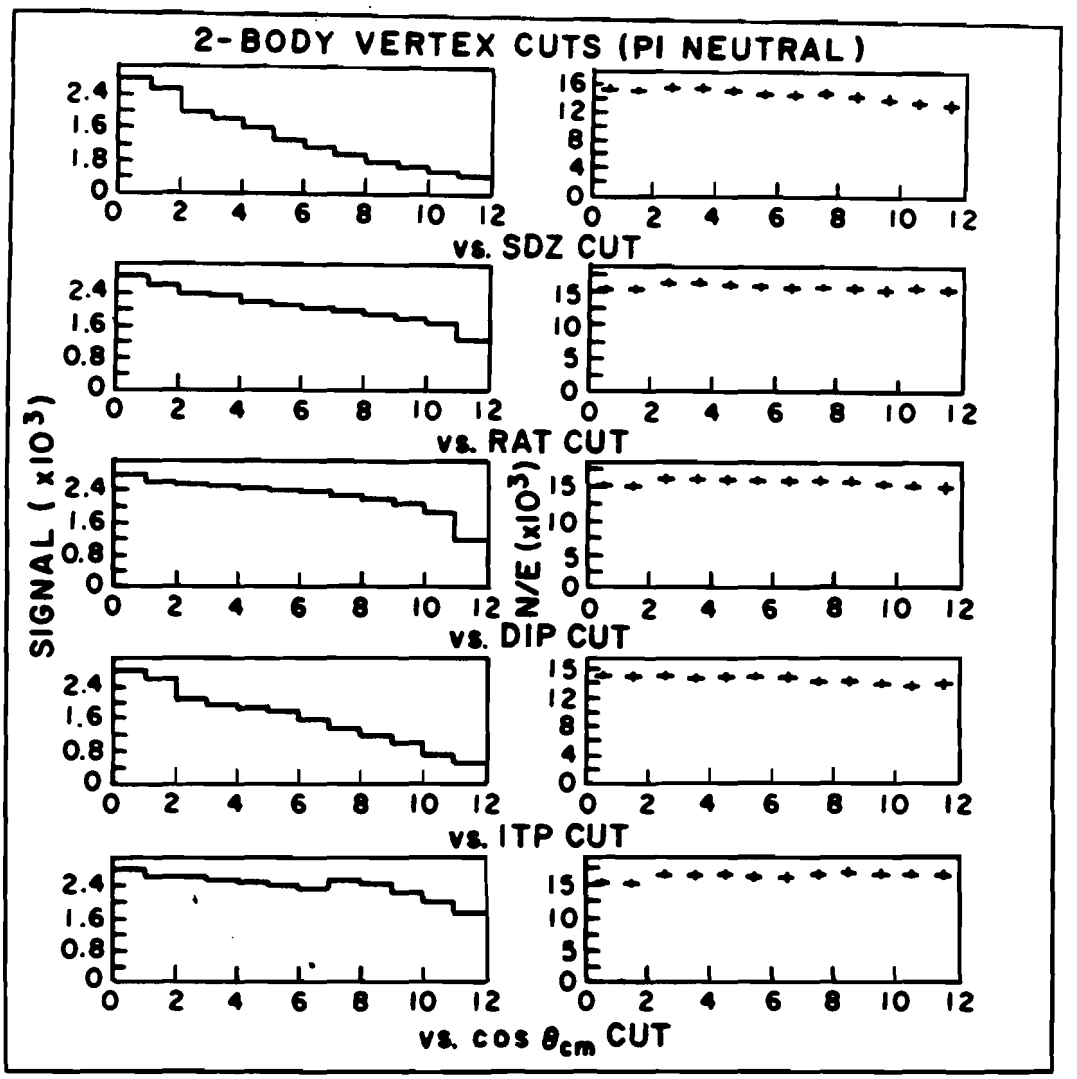

FIGURE 6.4.3. The behaviour of the charm signal $D^0 \rightarrow K^- \pi^+$ with modified 2-body vertex cuts and the pion excluded from the vertexing. The attenuation of the signal with the cut is shown on the left, the corresponding efficiency corrected signal is shown on the right. Table 6.4.1 contains the 12 cuts employed for each of these 5 cut parameters.

charm signal with respect to vertex cuts on the pion. This signal is stable for all cuts to within 10%. The pion was then excluded from the vertexing so that the behavior of the charm signal would more effectively mimic the $\Lambda_c^+ \rightarrow p\overline{K_0}$ mode. The plots on the right side of figure 6.4.3 shows the efficiency corrected signal with respect to the vertexing cuts on the kaon. Again, the signal is stable with respect to these cuts to within 10%.

The values of the cuts used in the plots contained in figures 6.4.1-3 are listed in table 6.4.1. There are twelve cuts listed for each cut parameter as there are twelve entries in each of the plots in these figures. The cuts that are listed in this table naturally correspond one to one to the plot entries. As can be seen in the plots, the cuts are tightened with each succeeding cut value except in the $\cos\theta$ plots where there are two sets of cuts investigated. In this case, the first set of cuts is applied to the cut variable $\cos\theta$ (No Vtx($\Rightarrow$No vertex cuts), NVV$>$ 0 ($\Rightarrow$Main vertex exists), .9, .8, .7, .6, .5) and the second set (.9, .8, .7, .6, .5) is applied to the parameter $|\cos\theta|$.

The final Monte Carlo tests were on the stability of the cuts used to define the neutrals (see section 6.1.1 and figure 6.1.1) and on the tracking efficiency of the neutral particle decay products. Figure 6.4.4 shows the K_s and Λ^0 efficiency corrected signals as a function of the neutral particle vertex cuts. As before, the efficiency corrected signal for both neutrals is stable with respect to these cuts to $< 10\%$.

The tracking efficiency of the neutral particle decay products is tested using large statistic charmed meson decay modes and, independently, using K^{*0} and K^{*+} signals. The study is discussed in Appendix A. In the study, efficiency correction factors were generated as a function of the beam energy

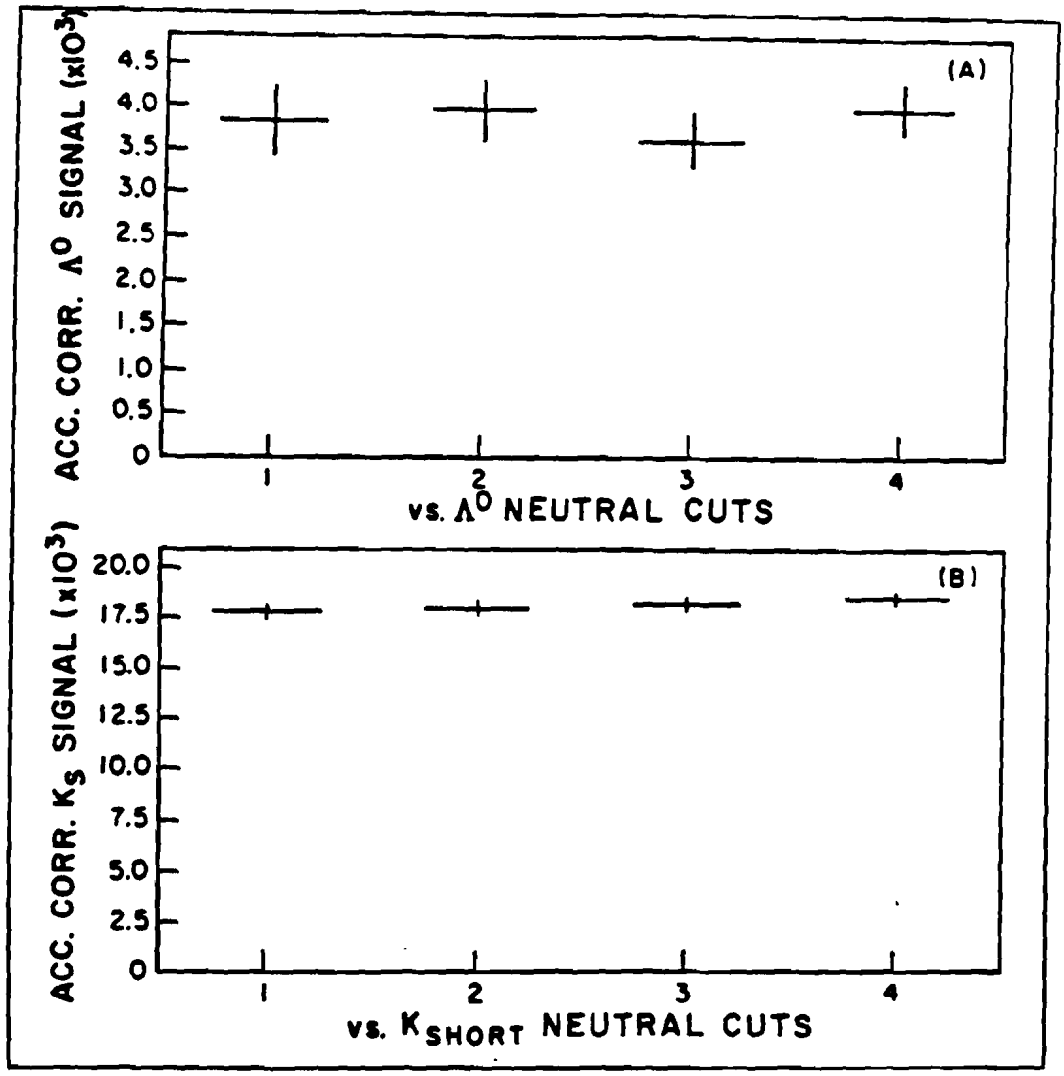

FIGURE 6.4.4. These plots show the stability of the Monte Carlo with respect to the neutral particle cuts; plot (A), the Λs and plot (B), the K_ss. The cuts are outlined in figure 6.1.1 which also shows the data signals used to generate these plots.

Table 6.4.1. Monte Carlo Study: Vertex Cuts

Cut	Cut Values
SDZ>	No Vtx,* NVV>0,** 0,2,4,6,8,10,12,14,16,18
DIP<	No Vtx, NVV>0, 200μ, 150, 100, 90, 80, 70, 60, 50, 40, 20
RAT<	No Vtx, NVV>0, 2., 1.5, 1., .9, .8, .7, .6, .5, .4, .2
ITP>	No Vtx, NVV>0, -20μ, 0, 10, 20, 40, 60, 80, 100, 150., 200.
COS<	No Vtx, NVV>0, .9, .8, .7, .6, .5
ABS(COS)<	.9, .8, .7, .6, .5

* No Vtx $\Rightarrow$ no vertex cuts are applied.

** Nvv> 0 $\Rightarrow$ at least one main vertex exists.

and the slope of the K_s momentum vector, $\frac{P_t}{P_z}(K_s)$. The K^* generated corrections presented in table 6.4.2 were used to correct the four charm modes and are applied in the final analysis (chapter 7). It should be noted that the reliability of the K^* corrections depends crucially on the relative production of the K^{*+} and the K^{*0}.

Table 6.4.2. Neutral Particle Efficiency Corrections

Decay Mode	Correction
$\Lambda\pi\pi\pi/\mathrm{pK}\pi$	$1.4 \pm .4$
$\Lambda\pi/\mathrm{pK}\pi$	$1.3 \pm .3$
$p\overline{K_0}/\mathrm{pK}\pi$	$1.2 \pm .3$
$\Lambda_c^+ \to p\overline{K_0}\pi\pi$	$1.3 \pm .3$

CHAPTER 7

RESULTS

In this chapter, the final set of cuts for each of the charm decay modes, $\Lambda\pi\pi\pi$, $\Lambda\pi$, $p\overline{K_0}$, and $p\overline{K_0}\pi\pi$, is outlined and the relative branching fractions for each of these modes relative to the $pK\pi$ mode is derived. These results are then compared to the theory where such predictions exist. A discussion of the possible decay mechanisms of the Λ_c^+ follows.

7.1 The Normalizing Mode: $\Lambda_c^+ \rightarrow pK\pi$

The $\Lambda_c^+ \rightarrow pK\pi$ decay mode has been discussed elsewhere.[44] We use this mode as the denominator in the calculation of the relative branching ratios reported in this thesis as it is the most significant Λ_c^+ signal seen in our experiment. The full complement of cuts were used to extract this signal. We apply a DIP cut of 80μ, an SDZ cut of 6., a RAT cut of 1.5, as well as Cerenkov cuts of 70% on the pion probability, 80% on the proton probability, and 50% on the kaon probability. The pion momentum must be greater than 3 GeV/c^2 as well. The signal is shown in figure 7.1.1. The Cerenkov cuts were chosen not simply to enhance the significance of the signal but to match the Cerenkov cut applied to the $p\overline{K^0}$ mode. The systematic error introduced by the proton efficiency correction will therefore not be included in this (or the $p\overline{K^0}\pi\pi$) decay mode.

The raw signal obtained in the $pK\pi$ decay mode is 134 ± 17 which implies an efficiency corrected signal of 6674 ± 885, given the $2.0 \pm .1\%$ efficiency of these cuts. The width of this fit is constrained to be 9 MeV/c^2 ,

which is the width of the Monte Carlo signal, and the mass is measured to be $2.286 \pm .002$ GeV/c^2 . Applying the Cerenkov corrections discussed in the last chapter (Kaon Correction $= 1.02 \pm .02$: Proton Correction $= 1.11 \pm .11$) to this mode we get the 'corrected' efficiency corrected signal,

$$A(pK\pi) = \frac{6674 \pm 885}{1.13 \pm .13} = 5900 \pm 780 \pm 800$$

where the systematic error introduced by the fit (4%) is included in the calculation.

It is important to note here that the Cerenkov cuts applied to the pKπ mode constrain the charm momentum to be > 40GeV/c^2 . In like manner, the charm signal in decay modes containing neutrals is negligible above 120 GeV/c^2 because of the difficulties involved in reconstructing high momentum neutrals. All the Λ_c^+ signals reported in this thesis therefore have their momenta constrained between [40-120GeV/c^2] so that the charm signals are compared in similiar charm momentum regions.

7.2 The $\Lambda_c^+ \rightarrow \Lambda\pi^+\pi^-\pi^+$ Signal

The analysis on the $\Lambda\pi\pi\pi$ mode was performed as follows. The vertex cuts used to extract the signal were the DIP cut, the RAT cut, the SDZ cut, and the χ^2_{sec}/DoF cut. These were applied to the charm vertex, as formed by the three pions, at the values shown in table 7.2.1. The momenta of the three pions was also constrained to be greater than 2 GeV/c^2 . The values of these cuts were chosen by maximizing the quantity $SIG = \frac{S_{MC}}{\sqrt{B_{DATA}}}$ which measures the significance of the $\Lambda\pi\pi\pi$ Monte Carlo signal, S_{MC}, with respect to the background, B_{DATA}, found in the data with the same cuts. Figure 7.2.1 illustrates how the value of the SDZ cut for the $\Lambda\pi\pi\pi$ mode was

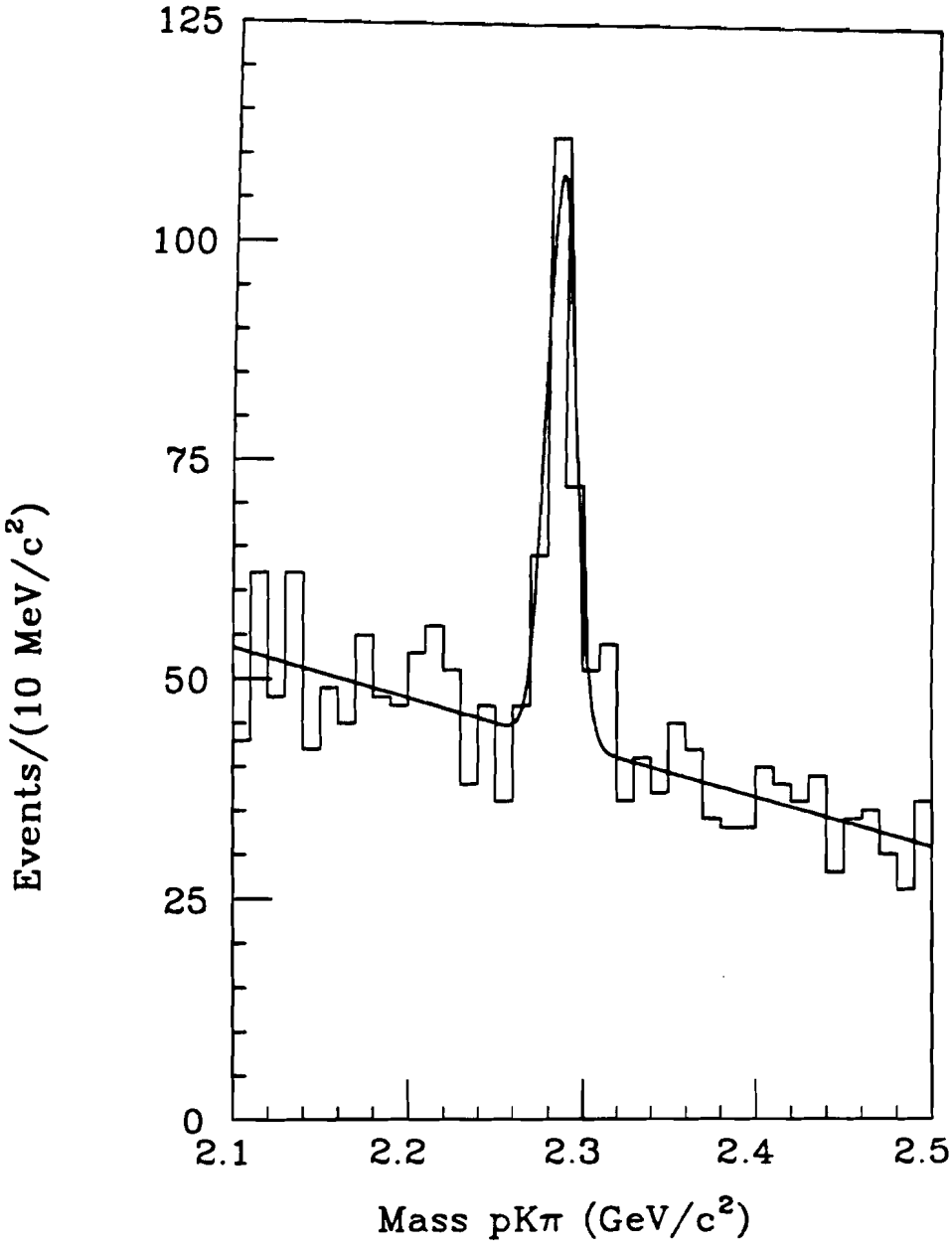

FIGURE 7.1.1. The $\Lambda_c^+ \rightarrow pK^-\pi^+$ invariant mass plot for 40 $<\bar{P}_{\Lambda_c^+}<$ 120GeV/c^2 . The width is constrained in the fit.

chosen. This technique was used to select the cuts used in all four Λ_c^+ decay modes.

Table 7.2.1 Final Cuts: $\Lambda\pi\pi\pi$

Cuts	ϵ
$P_{\pi 1...} > 2GeV/c^2$	.078
χ^2_{sec}/DoF< 3.5	.057
DIP < 80μ	.041
SDZ > 7	.013
RAT < 1	.01

With the cuts discussed above, we obtain the $\Lambda\pi\pi\pi$ data signal shown in figure 7.2.2. The plot is fit to a gaussian with a linear background. The width of the data signal is constrained to 12 MeV as indicated by the Monte Carlo generated data, and the mass is measured to be 2283± 5MeV in full agreement with the definitive value obtained in the pKπ mode.[44] The raw data signal is 44 ± 14 events and the efficiency is 1.00 ± .06%, which gives an efficiency corrected signal of 6800 ± 2200 Λ_c^+s. The branching fraction for $\Lambda^0 \rightarrow p\pi$ (.641) is included in this calculation. Applying the neutral efficiency correction (1.4 ± .4; see table 6.4.2) to this mode, we obtain the final efficiency corrected signal of 4860 ± 1570 ± 1430, where the systematic error introduced by the fit (7%) is included in the calculation. Normalizing to the pKπ signal, we obtain for the relative branching fraction;

$$RBF\left(\frac{\Lambda\pi\pi\pi}{pK\pi}\right) = .82 \pm .29 \pm .27. \qquad (7.2.2)$$

Comparison of this result with the results from other experiments will be left until after the relative branching fractions of all 4 modes have been presented.

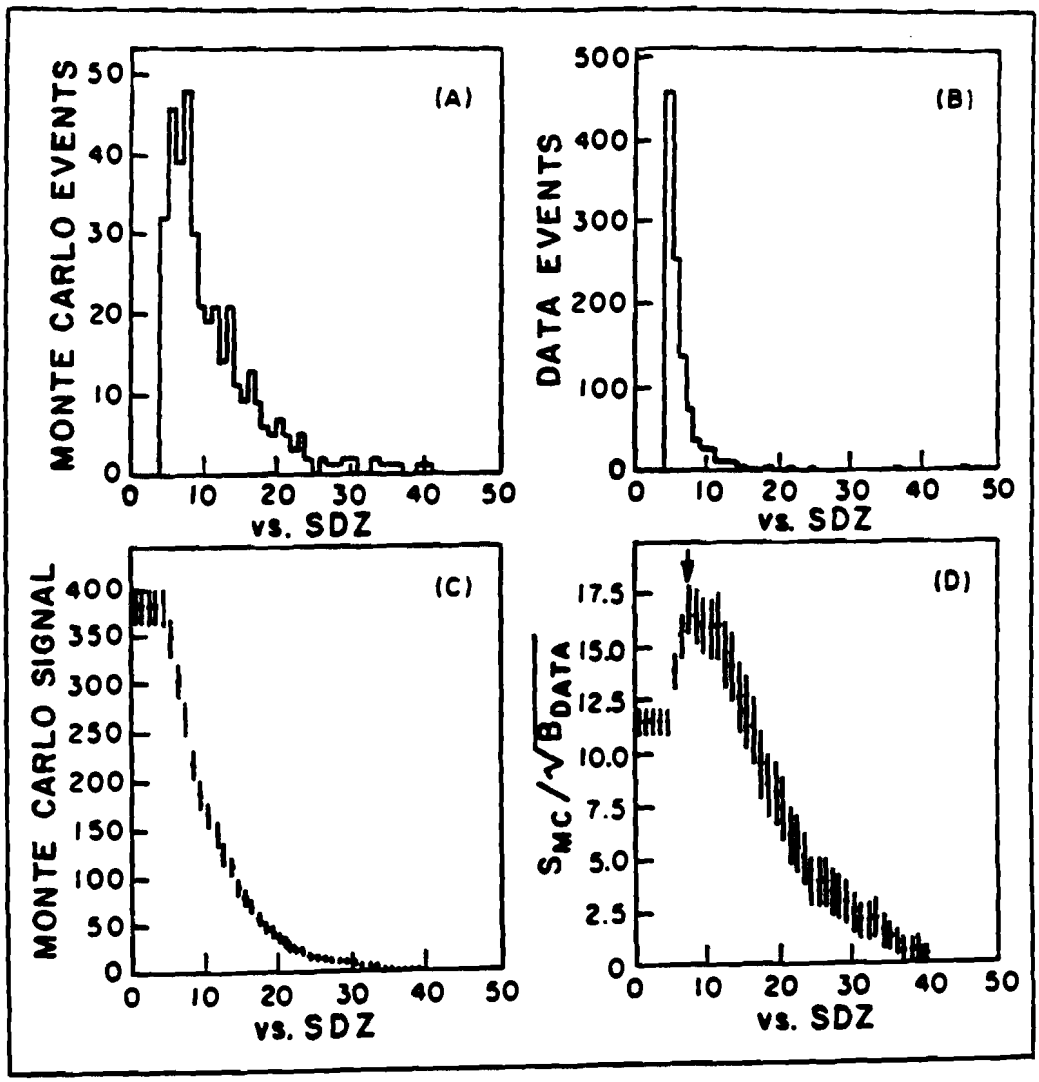

FIGURE 7.2.1. The plots used in selecting the SDZ cut for the $\Lambda\pi\pi\pi$ mode. (A) and (B) show the SDZ distribution of Monte Carlo signal and data background events respectively. Note the effect of the substrip cuts on these plots. Plot (C) shows the attenuation of the Monte Carlo signal with the SDZ cut. The significance of this signal with respect to the data background is shown in (D) where significance $= S/\sqrt{B}$. A cut at SDZ > 7 was used.

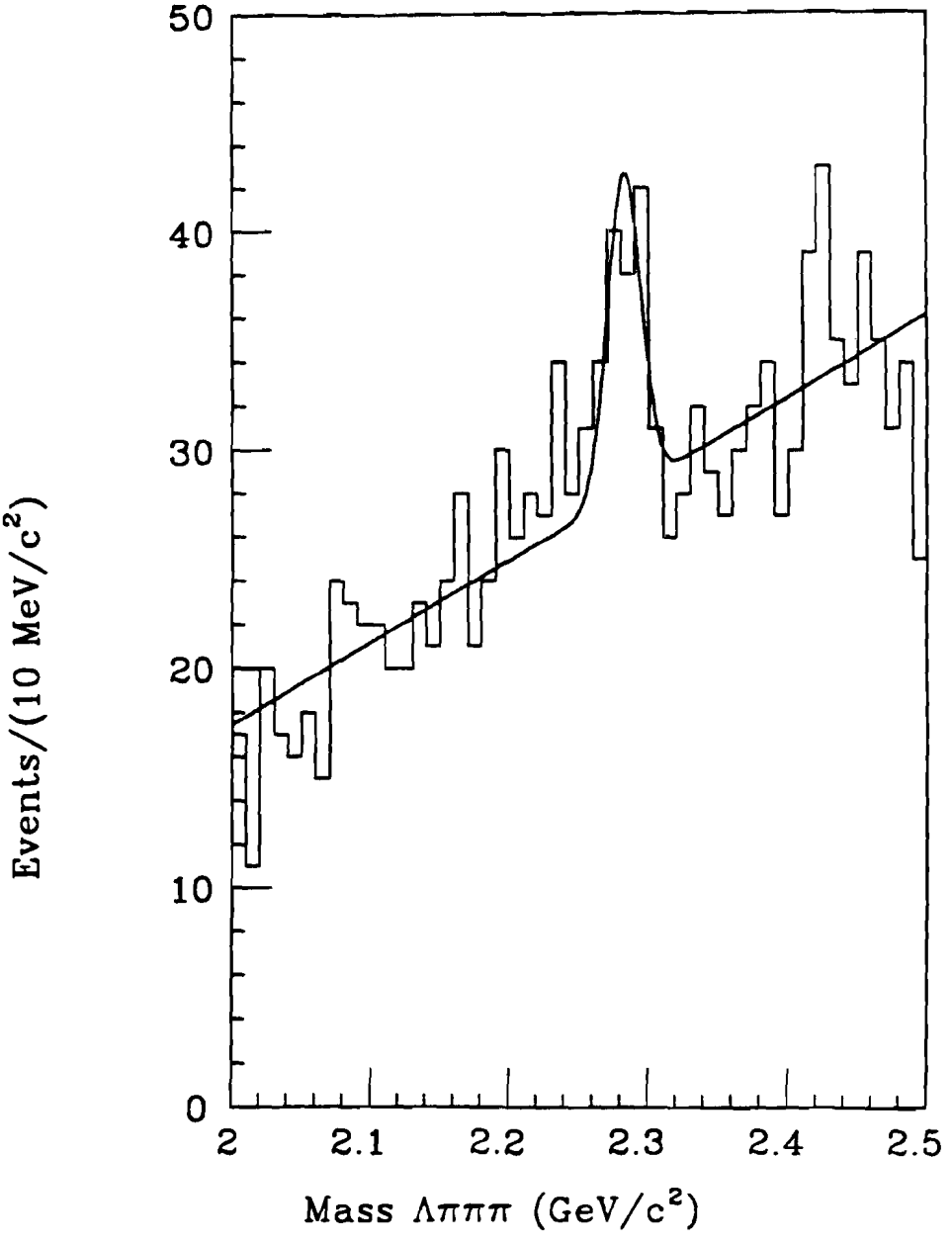

FIGURE 7.2.2. The $\Lambda_c^+ \rightarrow \Lambda\pi^+\pi^-\pi^+$ invariant mass plot for 40 $<P_{\Lambda_c^+}<$ 120GeV/c^2 . The width is constrained in the fit.

7.3 The $\Lambda_c^+ \rightarrow \Lambda\pi^+$ Signal

The analysis of the $\Lambda\pi$ mode differs greatly from the analysis of the $\Lambda\pi\pi\pi$ mode, as was discussed earlier. The vertex cuts used for this mode are the modified SDZ and RAT cuts, the DCA cut, and the $\cos_{cm}(\theta)$ cut discussed in section 6.3; their values are given in table 7.3.1. These cuts were chosen by maximizing the significance of the $\Lambda\pi$ Monte Carlo charm signal with respect to a background derived from the data, as for the $\Lambda\pi\pi\pi$ mode. The plots used to select the SDZ cut value for this mode are shown in figure 7.3.1. Comparing this plot qualitatively to figure 7.2.1 illustrates the improvement one could expect if a standard secondary vertex could be defined for the $\Lambda\pi$ mode.

Table 7.3.1 Final Cuts: $\Lambda\pi$

Cuts	ϵ
$\lvert\cos_{cm}(\theta)_\pi\rvert < .6$	.095
ITP $> 30\mu$	.048
DCA $< 80\mu$	.043
SDZ > 2	.037
RAT $< .75$	.034

The $\Lambda\pi$ data signal obtained by applying the cuts outlined in table 7.3.1 is shown in figure 7.3.2. The plot is fit to a gaussian plus a linear background function. The width and mass are both constrained; the width to 13 MeV, the value indicated by the Monte Carlo, and the mass to 2.286 GeV/c^2 as indicated by the strong pKπ signal. The raw data signal obtained is 28 $\pm$ 13 events and the efficiency is 3.4 $\pm$ .2%, implying an efficiency corrected Λ_c^+ signal of 1280 $\pm$ 600. The branching fraction for $\Lambda^0 \rightarrow p\pi$ is included in this calculation. Applying the neutral efficiency correction (1.3$\pm$

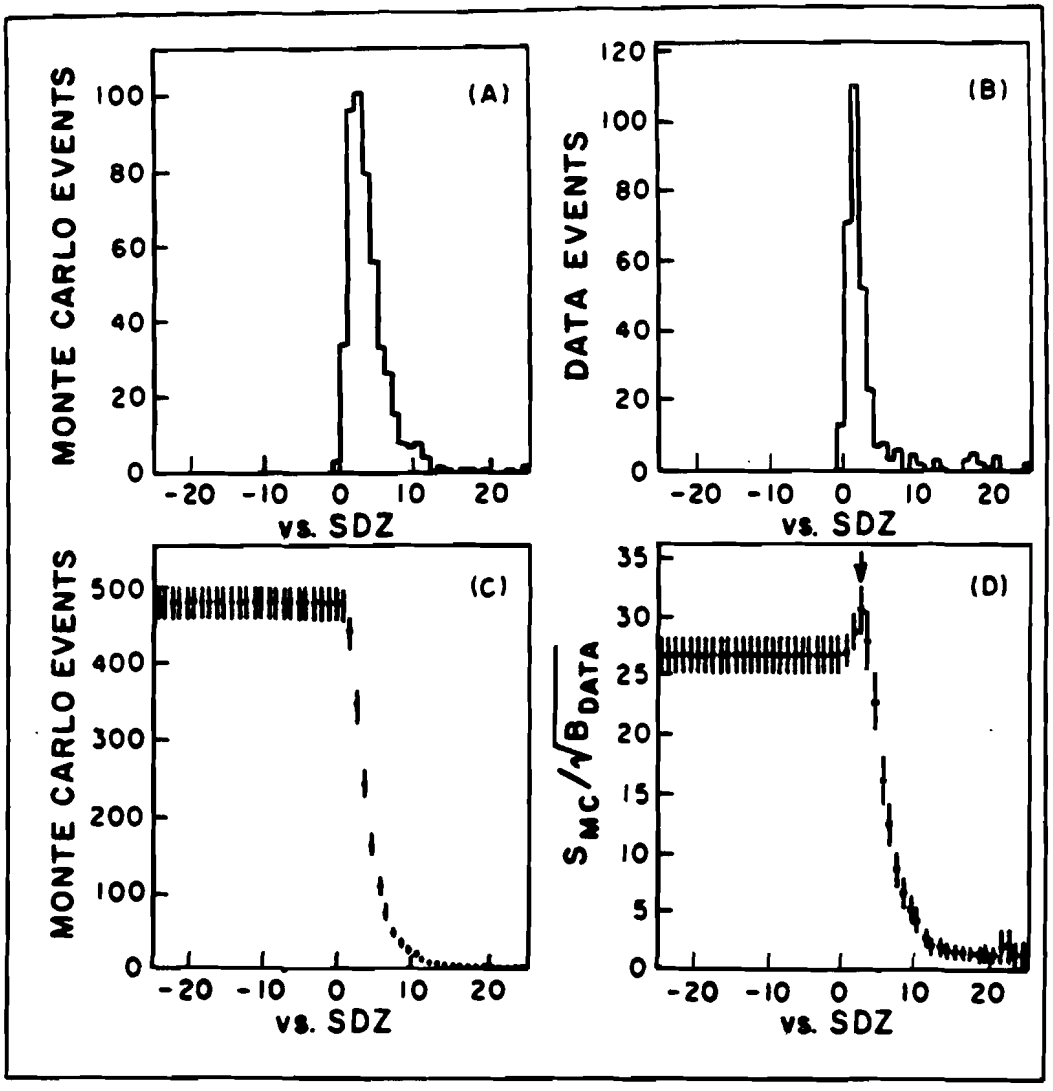

FIGURE 7.3.1. The plots used in selecting the SDZ cut for the $\Lambda\pi$ mode. (A) and (B) show the SDZ distribution of Monte Carlo signal and data background events respectively. Plot (C) shows the attenuation of the Monte Carlo signal with the SDZ cut. The significance of this signal with respect to the data background is shown in (D) where significance = $S/\sqrt{B}$. A cut at SDZ > 2 is indicated here.

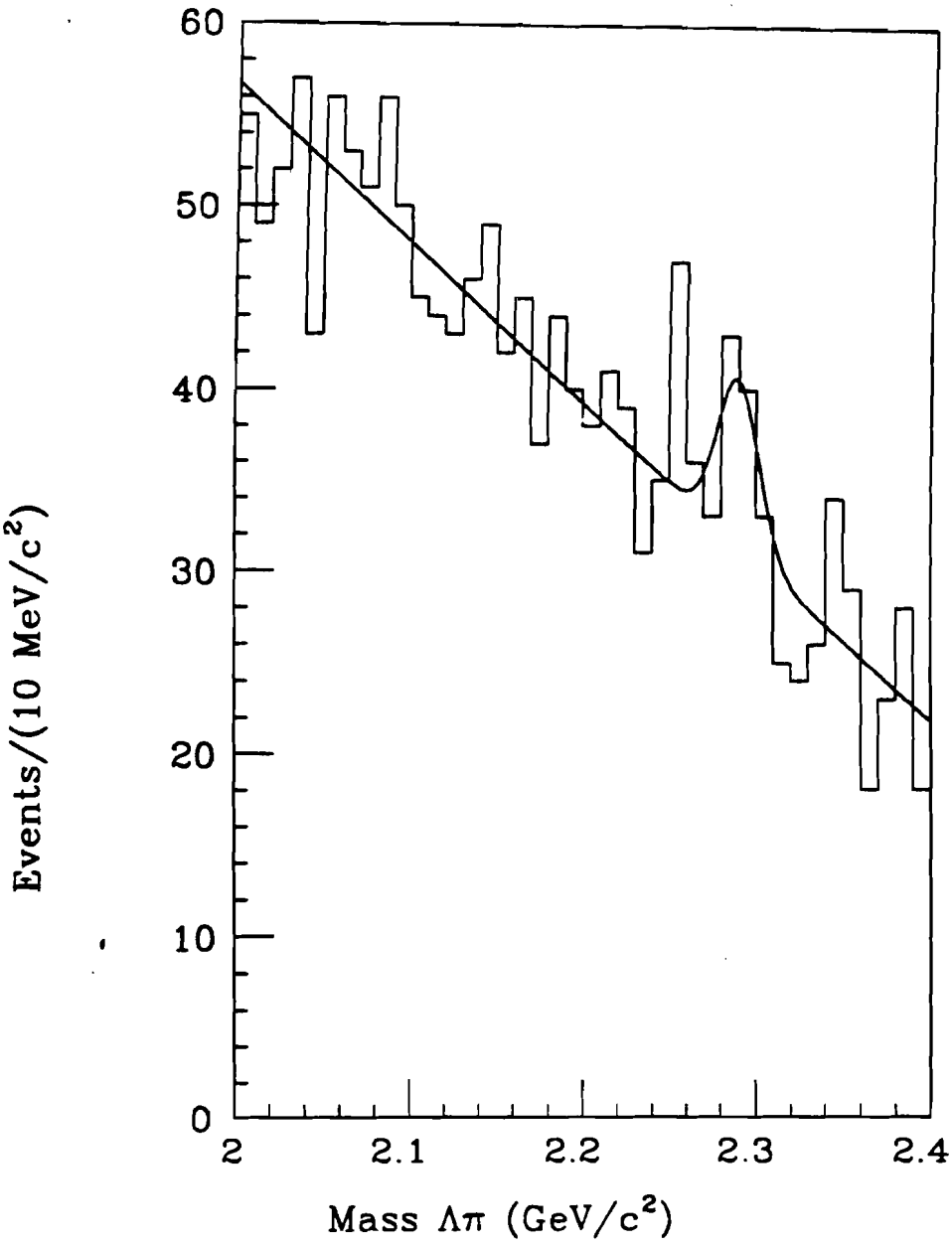

FIGURE 7.3.2. The $\Lambda_c^+ \rightarrow \Lambda\pi^+$ invariant mass plot for 40 $<P_{\Lambda_c^+}<$ 120GeV/c^2 . The width and mass are constrained in the fit.

.3) to this mode, we get the final efficiency corrected signal of $990 \pm 460 \pm 250$, where the systematic error from the fit (10%) is included in the calculation. Again, normalizing with the pKπ mode, we obtain the relative branching fraction for the $\Lambda\pi$ mode;

$$RBF\left(\frac{\Lambda\pi}{pK\pi}\right) = .17 \pm .08 \pm .05. \tag{7.3.2}$$

7.4 The $\Lambda_c^+ \rightarrow p\overline{K_0}$ Signal

The analysis on the $p\overline{K_0}$ decay mode was similiar to that used for the $\Lambda\pi$ mode. The modified 2-body vertex cuts were applied with the values given in table 7.4.1. A cut on $\cos_{cm}(\theta)$ was also applied as was the cut on the Cerenkov probability of the proton. The most important of these cuts were the Cerenkov cut and the ITP cut for reasons detailed in section 6.3.

Table 7.4.1 Final Cuts: $p\overline{K_0}$

Cuts	ϵ
$\lvert\cos_{cm}(\theta)_\pi\rvert < .8$	.105
$CV_{pr} > 80\%$	.085
DCA $< 80\mu$	.070
SDZ > 0	.047
RAT < 1	.032
ITP $> 30\mu$	.030

The $p\overline{K_0}$ data signal that we obtain with the cuts in table 7.5.1 is shown in figure 7.4.1. Again, the plot is fit to a gaussian plus a linear background and the width of the fit is set to 13 MeV as indicated by the

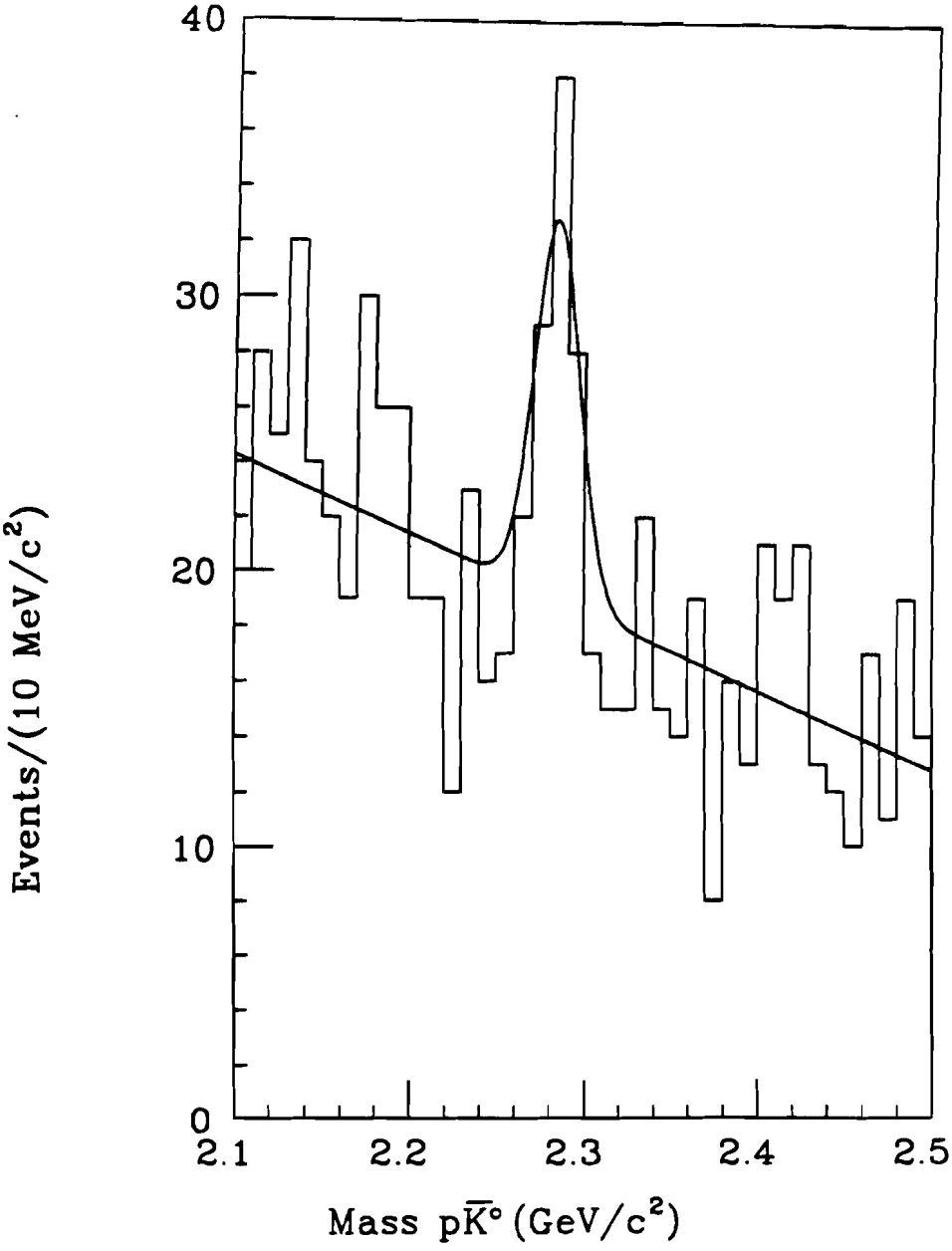

FIGURE 7.4.1. The $\Lambda_c^+ \rightarrow p\overline{K_0}$ invariant mass plot for 40 $<P_{\Lambda_c^+}<$ 120GeV/c^2 . The width is constrained in the fit.

Monte Carlo. The mass is measured to be 2283 ± 3 MeV, which is consistent with the pKπ mode. The raw data signal we obtain is 45 ± 12 events and the efficiency for this decay mode is 3.0 ± .2%, giving an efficiency corrected Λ_c^+ signal of 4350 ± 1190. The branching fractions of $\overline{K^0} \rightarrow K_s$ (.5) and $K_s \rightarrow \pi^+\pi^-$ (.686) are included in this calculation. Applying the neutral efficiency (1.2 ± .3) and the proton Cerenkov (1.11 ± .11) corrections, we get the final efficiency corrected signal of 3270 ± 890 ± 900, where the systematic error for the fit (5%) is included in the calculation. Note that the contribution to the systematic error from the proton Cerenkov correction is cancelled when this mode is normalized to the pKπ mode. The relative branching fraction obtained is then;

$$RBF\left(\frac{p\overline{K_0}}{pK\pi}\right) = .55 \pm .17 \pm .14. \qquad (7.4.2)$$

7.5 The $\Lambda_c^+ \rightarrow p\overline{K_0}\pi^+\pi^-$ Signal

The analysis of the p$\overline{K_0}\pi\pi$ mode proceeded in the same way as the analysis of the $\Lambda\pi\pi\pi$ mode since we were able to define a standard secondary vertex with the p$\pi\pi$ SESTR tracks. The cuts and their values are given in table 7.5.1. Comparing these cuts with the cuts used in the $\Lambda\pi\pi\pi$ analysis (see table 7.2.1), we can see the similiarity between the behavior of signal and background in these two modes. The main difference in their analyses is the Cerenkov cut on the proton probability, $CV_{p\pi\pi} > .25$ which, as noted earlier (see section 6.3), excludes all but definitely identified proton candidates.

Table 7.5.1 Final Cuts: $p\overline{K_0}\pi\pi$

Cuts	ϵ
$CV_{pr} \times CV_{\pi 1} \times CV_{\pi 2} > 25\%$	.050
$P_{\pi 1...} > 2GeV/c^2$	.043
$\chi^2_{sec}/dof < 3.5$	.028
$DIP < 80\mu$	.020
$SDZ > 7$	.006
$RAT < 1$	.004

The $p\overline{K_0}\pi\pi$ data signal is shown in figure 7.5.1. The width of the fit is set to 10 MeV as indicated by the Monte Carlo and the mass is set to the $pK\pi$ value of 2.286 GeV/c^2 . The plot is fit to a gaussian plus a linear background. The raw data signal is 9 $\pm$ 6 events and the efficiency for this mode is .4 $\pm$ .04%, implying an efficiency corrected Λ_c^+ signal of 6700 $\pm$ 4500. The branching fractions of $\overline{K^0} \rightarrow K_s$ and $K_s \rightarrow \pi^+\pi^-$ are included in this calculation. Applying the neutral efficiency (1.3 $\pm$ .3) and proton Cerenkov (1.11 $\pm$ .11) corrections, we get the final efficiency corrected signal of 4600 $\pm$ 3300, where the systematic and statistical errors have been combined. Normalizing this result to the $pK\pi$ mode, we obtain the limit;

$$RBF\left(\frac{p\overline{K_0}\pi\pi}{pK\pi}\right) < 1.7@90\%(CL). \qquad (7.5.2)$$

As with the $p\overline{K^0}$ mode, the proton Cerenkov correction does not contribute to the systematic error used in this measurement.

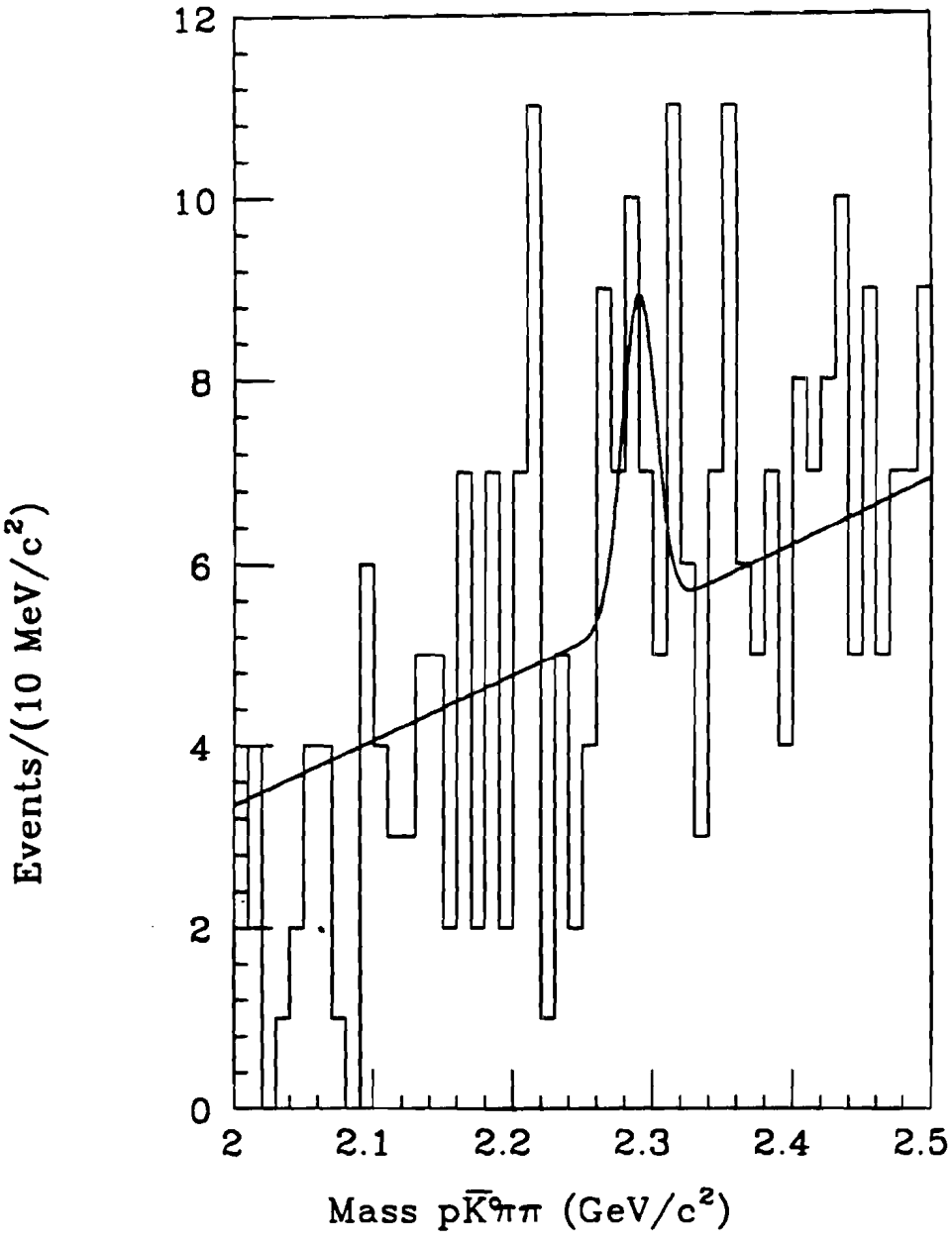

FIGURE 7.5.1. The $\Lambda_c^+ \rightarrow p\overline{K_0}\pi^+\pi^-$ invariant mass plot for 40 $<P_{\Lambda_c^+}<$ 120GeV/c^2 . The width and mass are constrained in the fit.

CHAPTER 8

RESULT COMPARISONS AND CONCLUSIONS

The relative branching fractions derived in the previous chapter are insensitive to the details of our experiment. We can therefore compare these values to similiar measurements made by other experiments. I will restrict my comparison with experiment to the results from CLEO and ARGUS, with some results from MARKII where applicable. A discussion of the theoretical results follows this.

Table 8.1.1 contains the results reported in this thesis along with previously existing results from the e^+e^- experiments, CLEO,[45] ARGUS,[46] and MARKII.[47] It is clear that our results agree with each of the other results, providing corroboration for these earlier measurements. It should be noted that these are the first significant measurements of Λ_c^+ relative branching fractions from a fixed target experiment.

The discussion of theoretical predictions for these rates will be restricted to the two body modes because these are the only decays that have been calculated. These predictions have been presented most conveniently in the form ($\frac{\tau(\Lambda\pi)}{\tau(p\overline{K^0})} \equiv$) RBF($\Lambda\pi/p\overline{K^0}$) by Ebert and Kallies.[13] The experimental value we obtain for this parameter is $.3 \pm .2$, which naturally agrees with the values obtained by CLEO(.33) and ARGUS($< .27$). Table 8.1.2 contains a comparison of our experimental result with available theoretical predictions. It is apparent that the SU(4), current algebra, and quark model

calculations agree with our result while the MIT Heavy Bag Model calculation disagrees.

The symmetry and quark model calculations were done by Kor̈ner, Kramer, and Willrodt.[11] In the SU(4) calculation, we consider the SU(2) I(=Isospin), U, and V spin subgroups, where;

$$I_+ d = \quad u; U_+ s = \quad d; V_+ s = \quad u$$
$$I_+ \overline{u} = -\overline{d}; U_+ \overline{d} = -\overline{s}; V_+ \overline{u} = -\overline{s}.$$

It is apparent that the effective hamiltonian (given in equation 1.2.1 and 1.2.2) transforms as an I or U spin vector, implying that the baryon decays obey the selection rules, $\Delta I = \Delta U = 1$. The two separate parts of this hamiltonian transform differently under V spin; the O^- part in equation 1.2.2 transforms as a V spin scalar ($\Delta V = 0$) while the O^+ part transforms as a V spin vector ($\Delta V = 1$). Kor̈ner *et. al.* applied the $\Delta I = \Delta U = 1$ and $\Delta V = 0$ properties of the hamiltonian to I, U, and V spin meson and baryon multiplets to obtain sum rules relating different $\Delta C = 1$ decays to each other. The $\Delta C = 1$ decays were then related in the same manner to known $\Delta C = 0$ decays and scaled by the ratio of enhancement factors ($\frac{f^{\Delta C=1}}{f^{\Delta C=0}} = 0.54$[48]) to obtain the estimate for the decay rate entered in column 2, table 8.1.2.

The decay amplitude used in the quark model calculation was derived from the effective hamiltonian (again, see equation 1.2.1) and is essentially the same as that obtained using current algebra.[15] In this calculation, the contribution to the rate from the W-exchange and W-emission diagrams is generated by inserting quark model wavefunctions[14] explicitly into this amplitude, where the wavefunction overlap, the ratio of enhancement factors, etc. are estimated from the known behavior of $\Delta C = 0$ decays. The contribution to the rate from the spectator diagrams is then derived in terms

of the measured current transition form factors of established baryons. These two amplitudes are added to get the relative branching fraction estimate entered in column 3, table 8.1.2.

Only the first term in the effective hamiltonian (equation 1.2.1) is used in the current algebra calculation.[15] Soft meson technique plus current algebra are used to reduce the three hadron matrix element to calculable baryon to baryon transition elements. The $\Delta C = 1$ baryon transitions elements in these expressions are then related to $\Delta C = 0$ transition elements using symmetry considerations. Adding in the spectator contribution as before, we obtain the value for the relative branching fraction entered in column 4, table 8.1.2.

The same soft meson plus current algebra method is used in the MIT Heavy Bag Model calculation to derive the baryon decay amplitude. The charm quark wavefunction is taken to be gaussian with $\sigma^2 \sim 1/M_c^2$ and the recoil of the charm quark with respect to the light quarks is neglected. The charm quark is thus centered in the bag. The masses and frequencies assigned to the light quarks in this calculation are the standard values[49] and, adding in the spectator contribution, we obtain the value for the relative branching fraction entered in column 5, table 8.1.2. This method is inconsistent with our experimental result because it underestimates the $\Lambda_c^+ \to p\overline{K^0}$ decay rate.

The future prospects for experimental measurements of these, and other, Λ_c^+ relative branching fractions are bright. CLEO and ARGUS have both taken more data since they submitted the results presented in this thesis, so significant improvement in their measurements of these ratios can be expected soon. Photon experiments (with hopes of taking 10^9 events)

Table 8.1.1: Charmed Baryon Relative Branching Fractions

Experiment	$\frac{B(\Lambda\pi\pi\pi)}{B(pK\pi)}$	$\frac{B(\Lambda\pi)}{B(pK\pi)}$	$\frac{B(p\overline{K^0})}{B(pK\pi)}$	$\frac{B(p\overline{K^0}\pi\pi)}{B(pK\pi)}$
E691	$.82 \pm .29 \pm .27$	$.17 \pm .08 \pm .05$	$.55 \pm .17 \pm .14$	< 1.7@90%CL
ARGUS	$.63 \pm .15 \pm .04$	$< .17$@90%CL	$.64 \pm .13 \pm .03$	$< .94$@90%CL
CLEO	$.80 \pm .19 \pm .22$	$.22 \pm .07 \pm .09$	$.66 \pm .20 \pm .19$	$.67 \pm .28 \pm .29$
Mark II		$< .25$@90%CL	$.72 \pm .32$	

Table 8.1.2: $\frac{\tau(\Lambda_c^0\pi^+)}{\tau(pK^0)}$ Experiment vs. Theory

E691	SU(4)	Quark Model	Current Algebra	Bag Model
$.3 \pm .2$	.4	.09	.47	1.9

and very high statistic fixed target hadron experiments also figure in the future of baryon physics. The most promising experiments of all, however, will most probably be the Z^0 factories gearing up at CERN and SLAC. The determination of all pertinent measurements involving the charmed baryons may well be at hand. The theoretical prospects are not this bright but, as the experimental results increase, so will the theorist's interest.

REFERENCES

1. Gell-Mann, M., Phys. Rev. Lett. **8**, 214 (1964).
2. Particle Data Group; Phys. Lett., **170B** 1 1986.
3. Greenberg, O.W., Phys. Rev. Lett. **13**, 598 (1964).
4. Gross, D.J., Wilczek, F., Phys.Rev.Lett. **30**, 1343 (1973); Politzer, H.; Phys. Rev. Lett. **30**, 1346 (1973).
5. Trilling, G; *The Properties of Charmed Particles*; Physics Reports **75** no.2 (1981).
6. Glashow, S.L., Ilioupoulos, J., Maiani, L; Phys Rev D **2** 1285 (1970).
7. Halsen and Martin; *Quarks and Leptons*, (John Wiley and Sons) 1984.
8. Gross, D.J., Wilczek, F., Phys. Rev. D**8**, 3633 (1973); Phys. Rev D**9**, 980 (1974), Politzer, H.D. Phys. Rep. 14**C**, 129 (1974).
9. Quigg, C., Kwong, W., Rosner, J.; *Heavy Quark Systems*, Fermilab-Pub-87/15-T.
10. Santoro, A., Souza, M., Escobar, C.; *Notes about Lambda/c*, E691 Internal Memo.
11. Korner, J.G., Kramer, G., Willrodt, J.; Zeit. fur Phys. **C** Particles and Fields 2, 117 (1979).
12. Ellis, J., Gaillard, M.K., Nanopoulos, D.V.; Nucl. Phys.; **B100** 313, (1975).
13. Ebert, D., Kallies, W.; Zeit. fur Phys. **C**, Particles and Fields 29, 643 (1985).
14. Delbargo, R., Salam, A., Strathdee, J.; Proc. Roy. Soc. A**278**, 146 (1965).
15. Hussain, F.,Scadron, M.D.; Il Nuovo Cimento **79A**, 248 (1984)
16. Jones, L., Wyld, H.; Phys Rev **D17** 759 (1978).
17. Holmes, S., Lee, W., Wiss, J.; Ann. Rev. Nucl. Part. Sci. **35**, 397 (1985).
18. Seyward, H; PhD Thesis; University of Toronto (1987).

19. Gaillard, M.D., Lee, B.W., Rosner, J.; Rev. of Mod. Phys., Vol 47, No. 2, (1975).

20. Bhadra, S; PhD Thesis; University of Colorado, Boulder (1984).

21. Tsai, Y; Rev. Mod. Phys.; **46**, 815 (1974).

22. Raab, J; PhD Thesis; University of California, Santa Barbara (1987).

23. The intrinsic resolution of this detector is $\sigma_{int}^2 = \frac{\int_{d/2}^{d/2} x^2 dx}{\int_{d/2}^{d/2} dx} = d^2/12$.

24. Browder, T; PhD Thesis; University of California, Santa Barbara (1988).

25. Damerell, C; *Vertex Detectors* In Ferbel, T (editor); *Techniques and Concepts of High Energy Physics IV*, Chapter 8; Plenum Press (1987).

26. Menary, S; Ms Thesis; University of Toronto (1986).

27. Jackson, J; *Classical Electromagnetism*, (John Wiley and Sons) 1975.

28. RCA Corporation, Lancaster, Penn., USA.

29. Bartlett, D.F. *et al*; Nucl. Ins. and Meth. **A260** 55 (1987).

30. Eagle Convex Glass Co., 419 Tuna St., P.O. Box 1340, Clarksburg, West Virginia, 26301, USA.

31. Acton Research Corp, 525 Main St., Acton, Mass., 01720, USA.

32. Carlson, P.J.; Nucl. Instr. and Meth., **158** 403 (1979).

33. LeCroy Corp., 700 S. Main St., Spring Valley, N.Y., 10977, USA.

34. Bartlett, D.F.; Duncan, A.L.; Elliot, J.R.; Rev. Sc. Inst. **52** 265 (1981).

35. Amersil Inc.; 650 Jones Road, Sayreville N.J., 08872, USA.

36. Summers, D; PhD Thesis; University of California, Santa Barbara (1984).

37. Mathews, J., Walker,R.L.; *Mathematical Methods of Physics*, (Benjamin, Menlo Park, California) 1970.

38. The apriori likelihoods for electrons, muons, pions, kaons, and protons used are .02, .01, .81, .12, .04 respectively.

39. The Λ and K_s strips differed because they were done by two different people. The slight differences in the cuts did not affect the charm signals.

40. Goldstein, H.; *Classical Mechanics*; (Addison-Wesley) 1950.

41. Sjostrand, T.; LU TP 85-10.

42. Cremaldi, L.M.; E691 Internal Group Memo, May 1988.

43. Sokoloff, M.D.; E691 Internal Group Memo, Jan 1988.

44. Anjos, J.C., *et al*; Phys. Rev. Lett.; **60** 1379 (1988)

45. Alam, M. *et al.*,, 1987 *International Symposium on Lepton and Photon Interactions at High Energies*, Hamburg.

46. Albrecht, H. *et al.*, 1987 *International Symposium on Lepton and Photon Interactions at High Energies*, Hamburg.

47. Abrams, G.S. *et al.*, Phys. Rev. Lett. **44** 10 (1980); Vella, E., PhD Thesis; University of California, Berkeley (1981).

48. Ellis, J., Gaillard, M.K., Nanopoulos, D.V.; Nucl. Phys. **B100**, 313, (1975).

49. Donoghue, J.F., Golovich, E.; Phys. Rev D **14** 1386 (1976).

50. Bean, A.; E691 Internal Memo; Oct. 88.

51. The uncorrected relative branching fraction for the $\overline{K^0}\ \pi\pi\pi$ mode is taken from a calculation of A. Bean. The $\overline{K^0}\pi\pi$ measurement is generated by the author.

52. Bean, A.; Study of the Decays D$\rightarrow$K$\pi\pi\pi$ and D$\rightarrow$K$\pi\pi\pi\pi$; Paper in Progress; 1988.

53. The initial K* study was more involved. The efficiency corrections were calculated with respect to *three* parameters; $\frac{p_t}{p_z}(K_s)$, beam energy, and kaon momentum.

54. Private Communication with Mike Witherell.

55. DeWolfe, E.A., *Proceedings of the* 15^{th} *Rencontre de Moriond*, *Vol.*1, Les Arcs, Savore, France March 9-21 201 (1980).

56. Paler *et al*, Nucl. Phys. **B96** 1 (1975).

57. Abachi, S. *et al*; Phys. Lett. 158**B** 519 (1985).

58. Abachi, S. *et al*; Phys. Lett. 199**B** 151 (1987).

APPENDIX

A

Neutral Particle Efficiencies

A1 Introduction

A problem with neutral particle efficiencies became apparent during the analysis of high statistics charmed meson decay modes containing $\overline{K^0}$s $\rightarrow K_s \rightarrow \pi^+\pi^-$.[50] Table A1.1 shows the uncorrected E691 measurements for the relative branching fractions of the charmed meson modes $\overline{K^0}\pi$, $\overline{K^0}\pi\pi$, and $\overline{K^0}\pi\pi\pi$ and the charmed baryon modes $\Lambda^0\pi^+\pi^+\pi^-$ and $p\overline{K^0}$.[51] These are compared with measurements from other experiments. In every case except the $D^+ \rightarrow \overline{K^0}\pi$ mode, the E691 measurement is high compared with the other measurements, implying that a systematic problem may exist.

From table A1.1, we see that the E691 and Mark III measurements of the $\frac{\overline{K^0}\pi\pi}{K\pi}$ relative branching fraction differ by a factor of 1.3 ± 0.3. This correction was applied to the measurement of the $D^+ \rightarrow \overline{K^0}\pi\pi\pi$ relative branching fraction to obtain the reported value of $.69 \pm .06 \pm .22$.[52] Applying this correction factor to the other modes (as must be done if it is used for the large $\overline{K^0}\pi\pi\pi$ mode), we obtain the values listed in table A1.1, column 4. From this table, one can see that there is an apparent disagreement between the 'corrected' relative branching fraction and the Mark III value in the

Table A1.1: Behaviour of Relative Branching Fractions

Mode	Other Expts.	Uncorr. E691	Corr.=1.3 ± .3
$\overline{K^0}\pi/\mathrm{K}\pi\pi$	$.35 \pm .04_{MIII}$ [47]	$.34 \pm .04$	$.26 \pm .03 \pm .06$
$\overline{K^0}\pi\pi/\mathrm{K}\pi$	$1.52 \pm .28_{MIII}$ [47]	$2.05 \pm .24$	
$\overline{K^0}\pi\pi\pi/\mathrm{K}\pi\pi$	$.79 \pm .13_{MIII}$ [47]	$.92 \pm .09$	$.71 \pm .07 \pm .16$
$\mathrm{p}\overline{K^0}/\mathrm{pK}\pi$	$.64 \pm .13_{ARGUS}$ [46]	$.66 \pm .20$*	$.51 \pm .15 \pm .12$
$\Lambda\pi\pi\pi/\mathrm{pK}\pi$	$.63 \pm .15_{ARGUS}$ [46]	$1.16 \pm .40$*	$.89 \pm .31 \pm .27$

* these measurements include cerenkov corrections(see section 6.4). The correction for the Λ^0 mode is assumed to be the same as for the K_s^0 modes.

$D^+ \rightarrow \overline{K^0}\pi$ mode. This disagreement in fact is worse than that which first motivated this study, indicating that the nature of the neutral efficiency problem is not well understood.

This study has two parts. First, the $D^* \rightarrow \pi D^0 \rightarrow \pi\overline{K^0}\pi\pi$ charm decay mode is examined in detail in an attempt to understand the behaviour of the $\overline{K^0}$. Then, the $K^{*+} \rightarrow \overline{K^0}\pi^+$ and $K^{*0} \rightarrow K^-\pi^+$ decays (and their charge conjugates) are investigated. Assuming that K^{*+} and K^{*0} production is the same, absolute efficiencies can be generated for the $\overline{K^0}$.

A2 A Closer Look at $D^{*+} \rightarrow \pi^+ D^0 \rightarrow \pi^+\overline{K^0}\pi^+\pi^-$

The behaviour of the $\overline{K^0}\pi\pi$ charm signal with beam energy is shown in figure A2.1(A). We assume, at this point, that the Monte Carlo is inefficient by the factor of 1.3 derived for table A1.1. The Monte Carlo histogram in this figure is therefore weighted by 1/1.3 to reveal the beam dependence of the inefficiency. The same procedure is followed for figures A2.1(B-D). Only high beam energy events ($> 150 GeV/c^2$) are used in these last three plots because the K_s efficiency problem is more marked for these energies, as can be seen in figure A2.1(A). It should be noted that the behaviour illustrated in these plots is evident in the $\overline{K^0}\pi\pi\pi$ decay as well.

From this figure, one can see that the behaviour of the Monte Carlo with respect to the data appears to depend on $\frac{P_t}{P_z}(K_s)$, (the slope of the neutral kaon with respect to the beam axis (fig A2.1(B))). The NTRK and kaon momentum distributions are also shown, in figures A1(C)and (D). To quantify the apparent efficiency dependence, the behaviour of the $\overline{K^0}\pi\pi$

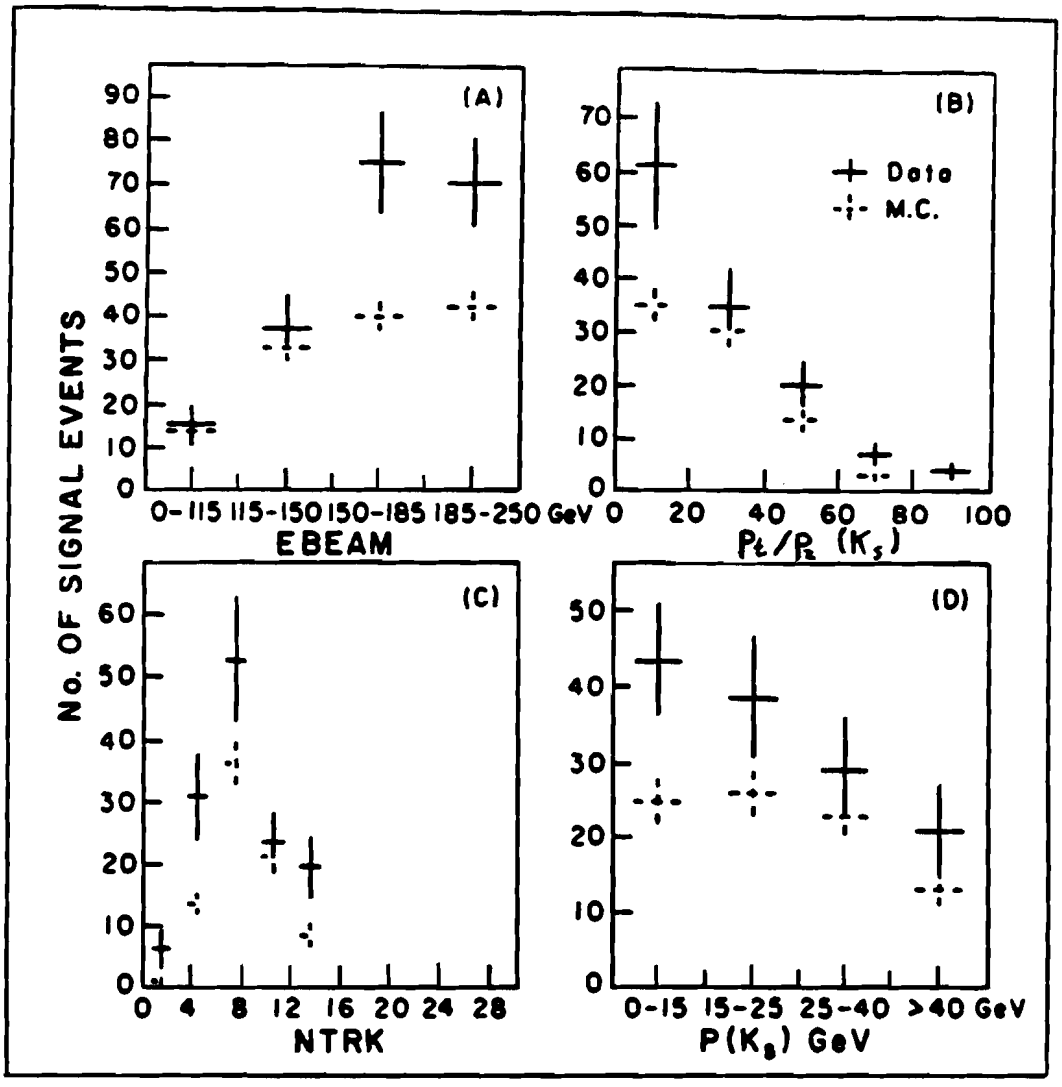

FIGURE A2.1. For the charm mode $D^{*+} \rightarrow \pi^+ D^0 \rightarrow \pi^+ \overline{K^0} \pi^+ \pi^-$. The behaviour of the data and Monte Carlo charm events with respect to beam energy is shown in (A). The Monte Carlo plot is weighted by 1/(Mark III correction factor) to give a qualitative idea of the beam dependence of the Monte Carlo inefficiency. Figures (B-D) are restricted to high beam energy events > 150 GeV/c^2 and illustrate the dependence of this inefficiency on (B) $\frac{P_t}{P_z}(K_s)$, (C) the number of tracks(excluding spurious and charm decay tracks), (D) the momentum of the K_s.

Table A2.1: Correction Factors using $\overline{K^0}\pi\pi$ Mode

	$E_{beam} < 150$	$E_{beam} > 150$	All Energies
All P_t/P_z	$1.1 \pm .3$	$1.5 \pm .3$	$1.3 \pm .3$
$P_t/P_z < .02$	$1.3 \pm .5$	$1.8 \pm .6$	$1.7 \pm .5$
$P_t/P_z > .02$	$1.0 \pm .3$	$1.3 \pm .4$	$1.2 \pm .3$

Table A2.2: N/ϵ Corrections Using $\overline{K^0}\pi\pi$

Mode	$f_{\overline{K^0}\pi\pi}$	$RBF_{\overline{K^0}\pi\pi}$
$\overline{K^0}\pi/K\pi\pi$	$1.3 \pm .3$	$.26 \pm .03 \pm .06$
$\overline{K^0}\pi\pi/K\pi$	$1.3 \pm .3$	
$\overline{K^0}\pi\pi\pi/K\pi\pi$	$1.4 \pm .4$	$.66 \pm .06 \pm .19$
$p\overline{K^0}/pK\pi$	$1.3 \pm .3$	$.51 \pm .15 \pm .12$
$\Lambda\pi\pi\pi/pK\pi$	$1.4 \pm .3$	$.83 \pm .29 \pm .18$

charm signal with respect to Mark III is presented in table A2.1 as a function of the beam energy and $\frac{P_t}{P_z}(K_s)$, where the entries in the table take the form;

$$f(E_{beam}, \frac{P_t}{P_z}(K_s)) = \frac{RBF(\frac{\overline{K^0}\pi\pi}{K\pi})_{E691}}{RBF(\frac{\overline{K^0}\pi\pi}{K\pi})_{MIII}}. \qquad (A2.1)$$

In table A2.2, the $\frac{P_t}{P_z}(K_s)$ dependent correction factors from table A2.1 ($1.7 \pm .5$ for $\frac{P_t}{P_z} < .02$: $1.2 \pm .3$ for $\frac{P_t}{P_z} > .02$) are applied to each of the five charm modes, giving the overall corrections expressed in column 2, table A2.2. These corrections are then applied to the uncorrected E691 branching fractions (column 3, table A1.1) to give the corrected measurements in column 3, table A2.2. The variation in these overall correction factors illustrates the mode to mode variation of the $\frac{P_t}{P_z}(K_s)$ distribution.

A3 The K* Study

It is interesting to consider the behaviour of the two decays $K^{*0} \rightarrow K^-\pi$ and $K^{*+} \rightarrow \overline{K^0}\pi^+$ as a further check of this problem. The motivation for this portion of the study follows from a desire to understand the systematic errors on these charm decay modes and, at the same time, to generate corrections that are independent of the Mark III experiment. Such corrections could even be applied to the $\overline{K^0}\pi\pi$ mode, which is sacrificed in the previous method.

From isospin arguments,[36] we know that the decay rates for $K^{*0} \rightarrow K^-\pi^+$ and $K^{*+} \rightarrow \overline{K^0}\pi^+$ are the same, since they are 'strong' decays. We assume the production of the charged and uncharged K*s is the same. At

Table A3.1: Correction Factors using K* Decays

	$E_{beam} < 150$	$E_{beam} > 150$	All Energies
All P_t/P_z	$1.1 \pm .1$	$1.5 \pm .1$	$1.3 \pm .1$
$P_t/P_z < .02$	$1.3 \pm .1$	$2. \pm .2$	$1.6 \pm .1$
$P_t/P_z > .02$	$1.1 \pm .1$	$1.2 \pm .1$	$1.2 \pm .1$

Table A3.2: Corrections Using K* vs P_t/P_z

Mode	$f \frac{P_t}{P_z}(K_s)$	RBF_{K^*}
$\overline{K^0}\pi/K\pi\pi$	$1.2 \pm .3$	$.28 \pm .03 \pm .07$
$\overline{K^0}\pi\pi/K\pi$	$1.3 \pm .3$	$1.58 \pm .18 \pm .36$
$\overline{K^0}\pi\pi\pi/K\pi\pi$	$1.3 \pm .3$*	$.71 \pm .06 \pm .16$
$p\overline{K^0}/pK\pi$	$1.2 \pm .3$	$.55 \pm .17 \pm .14$
$\Lambda\pi\pi\pi/pK\pi$	$1.4 \pm .4$	$.82 \pm .29 \pm .24$

* estimate using only non-resonant Monte Carlo

this point then the number of acceptance corrected K^{*+}s can be deduced using the $K^{*0} \rightarrow K^- \pi^+$ signal, and the Monte Carlo K^0_s efficiencies can be tested . The correction factor obtained from this comparison is,

$$f(E_{beam}, \frac{P_t}{P_z}(K_s)) = \frac{\frac{N}{\epsilon}(K^{*+})}{\frac{N}{\epsilon}(K^{*0})} \qquad (A3.1)$$

where again the K^* signals are split with respect to beam energy and kaon transverse momentum.The behaviour of the K^{*+} and K^{*0} signals with respect to these parameters (and the NTRK and K_s momentum distributions) is shown in figure A3.1. In this figure, the Monte Carlo plots are weighted with respect to the data by the factor in equation A3.1 and, as before, figures A3.1(B-D) include high beam energy events only (> 150 GeV/c^2).

The agreement between the $\overline{K^0}\pi\pi$ correction factors in table A2.1 and the K^* corrections factors in table A3.1 is good. This immediately implies that any charm decay correction derived with the K^*s will agree well with that derived using the $\overline{K^0}\pi\pi$ mode. Further, the correction for the $\overline{K^0}\pi\pi$ mode itself, which we can't get using the other correction method, will be nearly independent of $\frac{P_t}{P_s}(K_s)$ and of beam energy (and, in fact, kaon momentum)[53] implying that the K_s from the charged K^* decays mimics the K_s from the $\overline{K^0}\pi\pi$ decay.

The relative branching fractions of all the meson and baryon charm decay modes were calculated using the $\frac{P_t}{P_s}(K_s)$ dependent K^* correction factors ($1.6 \pm .1$ for $\frac{P_t}{P_s} < .02$: $1.2 \pm .1$ for $\frac{P_t}{P_s} > .02$) and are listed in table

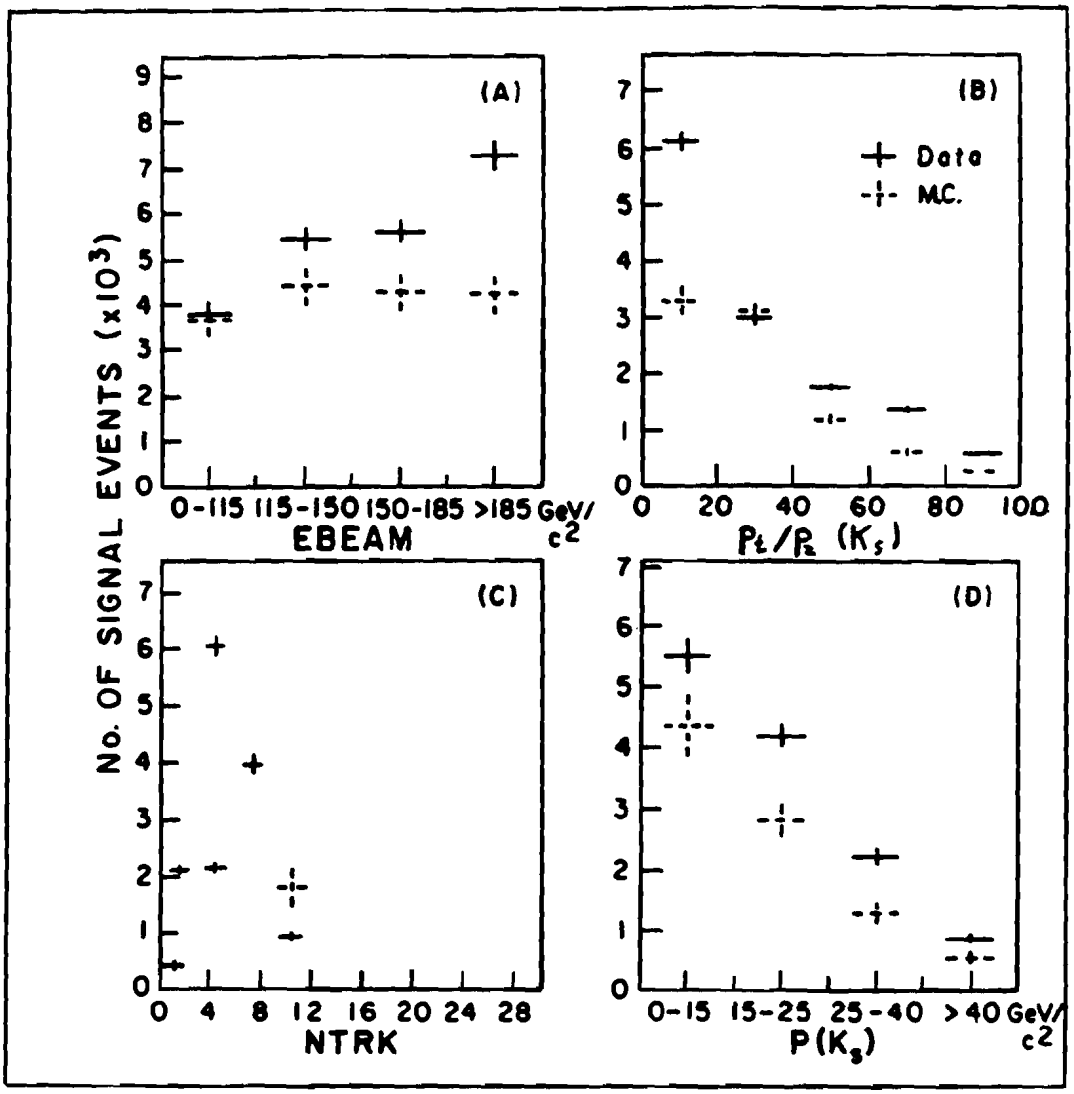

FIGURE A3.1. For the decay mode $K^{*+} \rightarrow \overline{K^0}\pi^+$. The behaviour of the data and Monte Carlo K^* events with respect to beam energy is shown in (A). The Monte Carlo plot is weighted by the factor in equation A3.1 to give a idea of the beam dependence of the Monte Carlo inefficiency. Figures (B-D) are restricted to high beam energy events > 150 GeV/c^2 and illustrate the dependence of this inefficiency on (B) $\frac{P_t}{P_z}(K_s)$, (C) the number of tracks (excluding spurious and K^* decay tracks), (D) the momentum of the K_s.

A3.2. As was inferred above, there is good agreement between the corrected relative branching fractions in column 3 of tables A2.2 and A3.2.

A4 Conclusions

The straightforward neutral efficiency correction of 1.3 ± 0.3 generated from the $\overline{K^0}\pi\pi$ mode has terrific simplicity. On the downside, it implicitly incorporates a measurement from another experiment (Mark III) into our results and, as it must be applied to all the neutral decay modes, pretends to correct decay modes that have quite different analyses and topologies. In this study, I investigated neutral particle (K_s) behaviour with respect to beam energy, K_s transverse and total momentum, and the total number of tracks in the event. The marked dependence of the neutral efficiency correction on beam energy, and on the slope of the kaon with respect to the beam, $\frac{P_t}{P_z}(K_s)$, can be seen in figures A2.1 and A3.1.

Tables A2.1 and A3.1 quantify this dependence. A close comparison of these tables testifies to the uniformity of the two methods of correction. It is also apparent that the beam energy dependence of the inefficiency is closely related to the $\frac{P_t}{P_z}(K_s)$ dependence, which is more than likely the fundamental dependence of the inefficiency. The $\frac{P_t}{P_z}(K_s)$ correction factors alone were chosen to generate the efficiency corrections for the charm decay modes.

After calculating the corrections for these modes (given in column 2 of table A3.2), we need to obtain an estimate of the systematic error introduced using this correction method. The errors on the K^* corrections in table A3.1 are statistical errors from the K^* fits and substantially underestimate

the systematic error we must assign to the full correction. The errors actually assigned are on the order of 20% and reflect the fact that the charm decays generate a substantial number of K_ss with high $\frac{P_t}{P_z}(K_s)$ ($> .02$) and high momentum (> 25 GeV/c^2) while the K^* decays do not.[53] The corrections applied to the portion of the charm signal with these characteristics therefore have large errors and generate a large contribution to the systematic error.

Comparing the distributions in figures A2.1 and A3.1, we can see that the K^{*+} decay mimics the $\overline{K^0}\pi\pi$ decay quite well in K_s momentum and $\frac{P_t}{P_z}(K_s)$, and not so well with NTRK and beam energy. Efficiencies vary slowly with respect to the number of tracks in the event, so the discrepancies between the NTRK data plots should not contribute to the systematic error greatly ($< 10\%$). (The fact that the Monte Carlo NTRK distribution for the K^{*+} doesn't match its data distribution won't affect the K^* corrections since the K^{*0} exhibits similiar behaviour). The error introduced by the discrepancy in the beam energy distributions can be estimated from figures A2.1(a) and A3.1(a) and is also of small effect ($< 10\%$).

Finally, the assumption that the production of the K^{*+} and the K^{*0} is the same introduces a contribution to the systematic error of $\sim 10\%$. Studies done on the K^*s in experiment E516, the predecessor of experiment E691, indicated that the relative production of K^{*0} to K^{*+} was the same to within $\sim 10\%$.[54] Results from kaon/proton interaction experiments[55,56] and e^+e^- experiments[57,58] give similiar limits. Combining these three contributions to the systematic error with the 20% errors on the corrections themselves, we obtain the systematic errors expressed in table A3.2. The systematic errors

reported in this appendix are due solely to the neutral efficiency corrections, while the final errors are reported in chapter 7.